



UPPSALA  
UNIVERSITET

*Digital Comprehensive Summaries of Uppsala Dissertations  
from the Faculty of Science and Technology 2133*

# New Roads for an Ancient Enzyme

*Whole-Cell Studies and New Cofactors for [FeFe]  
Hydrogenases*

MARCO LORENZI



ACTA  
UNIVERSITATIS  
UPSALIENSIS  
UPPSALA  
2022

ISSN 1651-6214  
ISBN 978-91-513-1462-4  
URN urn:nbn:se:uu:diva-470799

Dissertation presented at Uppsala University to be publicly examined in Å10K1190, Ångströmlaboratoriet, Lägerhyddsvägen 1, Uppsala, Monday, 23 May 2022 at 13:00 for the degree of Doctor of Philosophy. The examination will be conducted in English. Faculty examiner: Associate Professor Hannah Shafaat (Department of Chemistry and Biochemistry, Ohio State University).

### Abstract

Lorenzi, M. 2022. New Roads for an Ancient Enzyme. Whole-Cell Studies and New Cofactors for [FeFe] Hydrogenases. *Digital Comprehensive Summaries of Uppsala Dissertations from the Faculty of Science and Technology* 2133. 98 pp. Uppsala: Acta Universitatis Upsaliensis. ISBN 978-91-513-1462-4.

[FeFe] hydrogenases rare Nature's best H<sub>2</sub>-processing catalysts, and one of the best candidates to satisfy societal need for cheap and efficient catalyst for H<sub>2</sub>-evolution. These enzymes owe their remarkable catalytic activities to their organometallic active site, called "H-cluster". The H-cluster can be described as a canonical [4Fe4S] cluster linked via a bridging cysteine residue to a [2Fe] subsite, which is in turn coordinated by three CO, two CN<sup>-</sup> and one bidentate azadithiolate ligand. This unique cofactor allows these enzymes to function with virtually no overpotential requirements and TOFs up to 20 000 s<sup>-1</sup>. We have now reached a good understanding of the catalytic cycle by which these enzymes operate, yet many questions remain open especially regarding the physiological relevance of some the proposed intermediates.

In this thesis, we have used FTIR and EPR spectroscopies on whole-cell samples of [FeFe] hydrogenases to study the influence of the intracellular environment on the catalytic cycle of these enzymes. Moreover, we have investigated how the bacterial cytoplasm influences the stability of the H-cluster and favours the formation of sulfide-inhibited states, and we have studied the role of the proton-transfer chain and of steric factor related to the active site pocket in promoting this inhibition. Today, whole-cell systems attract a lot of interest due to the possibility to couple living cells with artificial photosensitizer to create whole-cell photocatalytic systems endowed with self-healing capabilities and broadband light absorption properties. We have built a system consisting of an *E. coli*-encapsulated [FeFe] hydrogenase coupled to the organic photosensitizer eosin Y, and we have verified the occurrence of light-induced electron transfer from eosin Y to the enzyme with consequent H<sub>2</sub> production. We have also applied a simple design-of-experiments approach to look into how the different system parameters interact with each other, and we have demonstrated that such approaches represent a viable strategy to guide the optimization of this type of photocatalytic systems. Finally, we have moved our attention to semi-artificial hydrogenases. We have used artificial maturation to generate asymmetric monocyanoide versions of the H-cluster using two different model hydrogenases, *CrHydA1* and *DdHydAB*. Through the application of FTIR, EPR and Protein-Film Electrochemistry we characterized these variants, studied the effect of this ligand exchange on the overall catalytic performance, and shed light on the effect of second-coordination sphere interaction on parameters such as catalytic rate, overpotential, affinity for H<sub>2</sub> and inhibitor sensitivity.

**Keywords:** [FeFe] hydrogenases, hydrogen, catalysis, photocatalysis, spectroscopy, whole-cell, semi-artificial enzymes

Marco Lorenzi, Department of Chemistry - Ångström, Molecular Biomimetics, Box 523, Uppsala University, SE-75120 Uppsala, Sweden.

© Marco Lorenzi 2022

ISSN 1651-6214

ISBN 978-91-513-1462-4

URN urn:nbn:se:uu:diva-470799 (<http://urn.kb.se/resolve?urn=urn:nbn:se:uu:diva-470799>)



*"The nation that will insist on drawing  
a broad line of demarcation between  
the fighting man and the thinking man  
is liable to find its fighting done by fools  
and its thinking done by cowards"*

*Sir William Francis Butler*



# List of Papers

This thesis is based on the following papers, which are referred to in the text by their Roman numerals.

- I. Mészáros, L.S., Ceccaldi, P., Lorenzi, M., Redman, H.J., Pfitzer, E., Heberle, J., Senger, M., Stripp, S.T., Berggren, G. (2020) Spectroscopic investigations under whole-cell conditions provide new insight into the metal hydride chemistry of [FeFe]-hydrogenase. *Chemical Science*, 11(18): 4608-4617.  
**Author's contributions:** Contributed to the activity assays. Performed EPR-samples preparation and participated to EPR measurements. Had a supporting role on manuscript writing and figures preparation.
- II. Lorenzi, M., Ceccaldi, P., Rodríguez-Maciá, P., Redman, H.J., Zamader, A., Birrell, J.A., Mészáros, L.S., Berggren, G. (2022) Stability of the H<sub>2</sub> cluster under whole-cell conditions - formation of an H<sub>trans</sub>- like state and its reactivity towards oxygen. *Journal of Biological Inorganic Chemistry*, 27, 345–355  
**Author's contributions:** Contributed to the planning of the project and to the interpretation of the results. Contributed to CrHydA1 sample preparation and data collection. Wrote the manuscript, and designed and prepared figures with support from other authors.
- III. Lorenzi, M., Senger, M., Gamache, M.T., Redman, H.J., Berggren, G. H<sub>2</sub> production as a model reaction for exploring E. coli based semi-artificial photosynthetic systems. *Manuscript in preparation*.  
**Author's contributions:** Developed the experimental design. Performed EPR experiments, photocatalytic assays and ANOVA analyses. Wrote the manuscript, and designed and prepared figures with support from other authors.

- IV. **Lorenzi, M.**, Gellet, J., Zamader, A., Senger, M., Duan, Z., Rodríguez-Maciá, P., Berggren, G. Investigating the role of the strong field ligands in semi-synthetic hydrogenases: Spectroscopic and functional characterization of the asymmetric monocyano active site. *Submitted*.

**Author's contributions:** On CrHydA1's side, lead the planning of the project, purified, reconstituted and matured both the wild-type and the mutants, performed all FTIR and electrochemical experiments. Measured H<sub>2</sub>-evolution activity, and recorded and analysed EPR spectra on both *CrHydA1* and *DdHydAB* samples. Wrote the manuscript, and designed and prepared figures with support from other authors.

First and co-first authors are underlined in the author list.

Reprints were made with permission from the respective publishers.

## Other publications not included in this thesis

During the PhD, contribution were made to the following publications, not included in the thesis.

- I. Land, H., Ceccaldi, P., Mészáros, L.S., **Lorenzi, M.**, Redman, H.J., Senger, M., Stripp, S.T., Berggren, G. (2019) Discovery of novel [FeFe]-hydrogenases for biocatalytic H<sub>2</sub>-production. *Chemical Science*, 10, 9941-9948.
- II. Senger, M., Kernmayr, T., **Lorenzi, M.**, Redman, H.J., Berggren, G. Hydride state accumulation in native [FeFe]-hydrogenase with the physiological reductant H<sub>2</sub> supports its catalytic relevance. *Submitted*
- III. Senger, M., **Lorenzi, M.**, Redman, H.J., Berggren, G. (2022) The missing intermediate in the catalytic cycle of [FeFe]-hydrogenases: Diiron site reduced state featuring a bridging CO ligand observed at room temperature. *ChemRxiv*
- IV. Pavliuk, M.V., **Lorenzi, M.**, Morado, D.R., Gedda, L., Wrede, S., Mejias, S.H., Liu, A., Senger, M., Glover, S., Edwards, K., Berggren, G., Tian, H., Polymer Dots as Photoactive Membrane Vesicles for [FeFe]-hydrogenase Self-assembly and Solar-driven Hydrogen Evolution. *Submitted*.





# Contents

Chapter 1 - Introduction.....	13
1.1. Today's "hydrogen world" .....	15
1.1.1. Hydrogen applications .....	17
1.1.2. Hydrogen production methods.....	18
1.2. [FeFe] hydrogenases .....	23
1.2.1. Diversity in the world of hydrogenases .....	25
1.2.2. The proposed catalytic cycle .....	27
1.2.3. Inhibition .....	29
1.2.4. Outlook .....	29
1.3. Back to the cell.....	32
1.3.1. Whole cell spectroscopy .....	34
1.3.2. Whole-cell biocatalysis.....	36
1.3.3 Summary.....	37
1.4. Foreword .....	38
Chapter 2 - Paper I: Spectroscopic investigations under whole-cell conditions provide new insight into the metal hydride chemistry of [FeFe]-hydrogenase .....	39
2.1. Introduction and motivation. ....	39
2.2. Generation of a functional CrHydA1 enzyme under whole-cell condition.....	39
2.3. Integrity check.....	42
2.4. Probing the catalytic cycle with whole-cell ATR-FTIR spectroscopy.....	44
2.5. Confirming the occurrence of two distinct hydride states with EPR. ....	47
2.6. Conclusions. ....	48
Chapter 3 - Paper II: Stability of the H-cluster under whole-cell conditions – Formation of an H <sub>trans</sub> -like state and its reactivity towards oxygen .....	51
3.1. Introduction and motivation .....	51
3.2. Stability of [FeFe] hydrogenases under whole-cell conditions .....	52
3.3. Oxygen tolerance.....	54
3.4. Role of the Proton Transfer Chain in the formation of the H <sub>trans</sub> -like state .....	55
3.5. Conclusions .....	57

Chapter 4 - Paper III: H <sub>2</sub> production via an <i>E. coli</i> based semi-artificial photosynthetic system.....	59
4.1. Introduction and motivation .....	59
4.2. System design.....	60
4.3. Spectroscopic characterization .....	60
4.4. DoE and ANOVA .....	62
4.4.1. Oxygen tolerance .....	66
4.5. Conclusions .....	67
Chapter 5 - Paper IV: Investigating the role of the strong field ligands in semi-synthetic hydrogenases: Spectroscopic and functional characterization of the asymmetric mono-cyanide active site. ....	69
5.1. Introduction and motivation .....	69
5.2. Cofactor insertion and spectroscopic characterization .....	71
5.2.1. FTIR.....	71
5.2.2. EPR.....	73
5.3. Determining the isomer form .....	74
5.4. Reactivity towards inhibitors.....	75
5.5. Catalytic properties .....	76
5.6. Conclusions .....	77
Chapter 6 – Summary and Outlook.....	79
Popular Science Summary .....	81
Populärvetenskaplig Sammanfatning.....	83
Riassunto divulgativo.....	85
Aknowledgments .....	87
References.....	90

# Abbreviations

[2Fe] <sub>H</sub>	Di-iron subsite of the H-cluster
[2Fe2S]	Two-iron-two-sulfur cluster
[4Fe4S]	Four-iron-four-sulfur cluster
[4Fe4S] <sub>H</sub>	Four-iron-four-sulfur cluster of the H-cluster
AFM	Atomic Force Microscopy
ANOVA	Analysis Of Variance
ATR-FTIR	Attenuated Total Reflection Fourier-Transformed InfraRed
CCUS	Carbon Capture, Usage and Storage
CV	Cyclic Voltammogram
cwEPR	Continuous-Wave Electron Paramagnetic Resonance
DEER	Double Electron-Electron Resonance
Fe <sub>d</sub>	Distal iron of the H-cluster
Fe <sub>p</sub>	Proximal iron of the H-cluster
ENDOR	Electron Nuclear Double Resonance
EPR	Electron Paramagnetic Resonance
FRET	Förster Resonance Energy Transfer
FTIR	Fourier-Transformed InfraRed
GFP	Green Fluorescent Protein
GHG	GreenHouse Gas
HHV	High Heating Value
LHV	Low Heating Value
NaDT	Sodium Dithionite
NHE	Normal Hydrogen Electrode
NMR	Nuclear Magnetic Resonance
PAGE	PolyAcrilamide Gel Electroforesis
PBS	Phospate-Buffered Saline
PCET	Proton-Coupled Electron Transfer
PFE	Protein-Film Electrochemistry
SDS	Sodium Dodecyl Sulfate
ROS	Reactive Oxygen Species
SHE	Standard Hydrogen Electrode
SMR	Steam Methane Reforming
sSNOM	Scattering Scanning Nearfield Optical Microscopy
TEOA	Tri-Ethanol Ammine
WGSr	Water-Gas Shift Reaction



# Chapter 1 - Introduction

We often speak of “the hydrogen world”: the futuristic depiction of a society relying on sustainable hydrogen gas for most of its energy needs. Here biological  $H_2$  production, enabled by metalloenzymes, has the potential to play an important role in assuring a sustainable supply. Hydrogen is often referred to as the most promising energy vectors for helping us to achieve an epoch-making energy shift towards renewables, and for sure it has all the hallmarks to be it. Indeed, hydrogen gas has the highest heating value between combustible fuels with a value of 120-142 MJ/kg, depending on conditions, and its combustion is absolutely “clean” as the only byproduct consists of water vapour. This fact, for instance, would make hydrogen-powered vehicles the only alternative to battery-powered electric cars for zero-emission personal transportation.

**Table 1.1** Higher (HHV)\* and lower heating values (LHV)\* for selected fuels. \* HHV is calculated including the latent heat of vaporization of the water produced during combustion, LHV considers that energy lost.

Fuel	HHV (MJ/kg)	LHV (MJ/kg)
Hydrogen ( $H_2$ )	141.80	119.96
Methane	55.50	50.00
Butane	49.50	45.75
Kerosene	46.20	43.00
Diesel	44.80	43.4
Coal (Anthracite)	32.50	/

Unfortunately, between two states of the world there is always a transition, which is seldom smooth and cheap. Fossil fuels have been a staple for human societies for centuries - since the industrial revolution – which means that a global infrastructure for extraction, transportation and efficient usage of these power sources is already in place. This cannot be said for hydrogen.

Despite having a high gravimetric energy density, hydrogen gas only weighs 0.0899 g/l, making its volumetric energy density actually quite low and posing a relevant problem when it comes to transport and storage, due to technical and practical limitations.

For instance, adapting the infrastructures used for natural gas for  $H_2$  transportation is a challenging endeavour. Existing pipelines cannot withstand pure

hydrogen as it would embrittle the steel, leading to possible structural failures or leaks of an explosive gas, and liquifying it comes at the cost of roughly 30% of the energy stored. As a widespread distribution, analogous to the one we have developed e.g. for automotive fuels, will be pivotal to implement hydrogen usage for daily energy needs, many technological solutions are currently being developed for the aforementioned issues.<sup>1</sup>

Today, a lot of attention is put on imagining how the future “hydrogen world” will look like and to delineate the massive efforts and economic investments that are going to make it possible; less attention, though, is put on discussing the role that hydrogen has in today’s society and how much we are already reliant on this small molecule.

In this chapter I will try to give a glimpse of the “hydrogen world” we already live in and discuss how researching new ways of producing this gas can have an immediate impact on today’s society.

# 1.1. Today’s “hydrogen world”

In 2020 world consumption of hydrogen gas has exceeded 80 Mt/year, with three industrial sectors driving demand: ammonia and methanol production, oil refining and steel manufacturing (Fig. 1.1).<sup>2</sup>

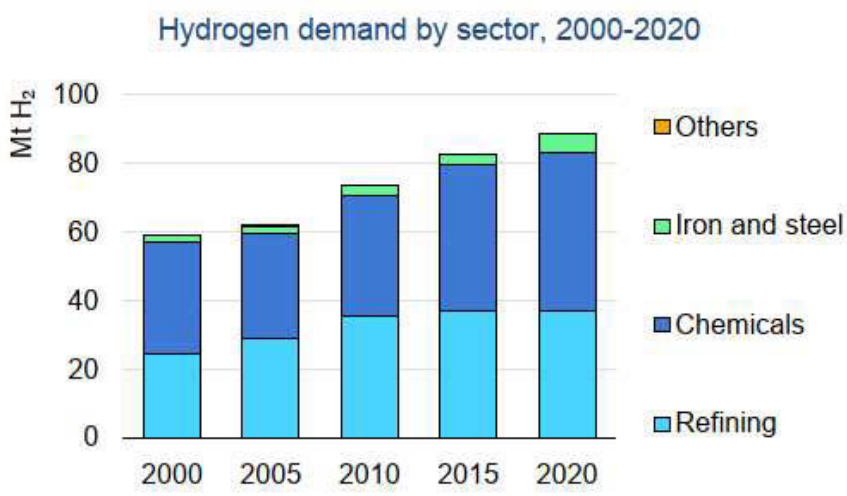


**Fig. 1.1** Hydrogen demand by sector during the period 2000-2020. “Others” indicates a minor fraction of demand coming from other industrial application, transportation or electricity generation. Source: IEA (2021) Global Hydrogen Review. All rights reserved.

Projections for a Net Zero Emission scenario estimate a global consumption higher than 530 Mt/year. In 2020, practically all of the hydrogen supply was derived from fossil fuels, with 79% being generated in dedicated industrial facilities and 21% being obtained as a by-product of naphtha reformation into gasoline (Fig. 1.2). Electrolyser plants currently only account for 0.03% of the global H<sub>2</sub> production.<sup>2</sup>



## Sources of hydrogen production, 2020

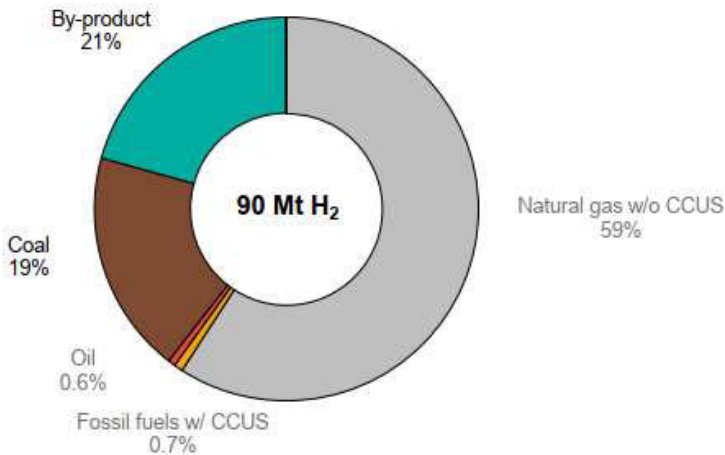


**Fig. 1.2** Global sources of hydrogen in 2020. CCUS stands for “Carbon Capture, Usage and Storage” and indicates the ensemble of technologies used to make use of CO<sub>2</sub> emissions from industrial processes. Source: IEA (2021) Global Hydrogen Review. All rights reserved.

Clearly, the current mix of hydrogen sources is far from being “green”; we will see in section 1.1.1 that many of the methods we rely upon today involve generating CO<sub>2</sub> as a by-product. In many cases, H<sub>2</sub> production can be effectively decarbonized by applying carbon capture technologies (CCUS) but this approach is still limited due to the impact it has on the final product’s cost.<sup>3</sup>

Even when CCUS are applied, it should not be forgotten that methane is an extremely potent GHG, 25 time more potent than the infamous CO<sub>2</sub>,<sup>4</sup> and that extractive activities are estimated to be responsible for one third of all CH<sub>4</sub> emissions into the atmosphere.<sup>5</sup>

Given the times we are living through as I am writing this section, I cannot refrain from a final consideration. As I will try to briefly show in section 1.1.1, the processes that require hydrogen are pivotal to our society; on them depend some of our key infrastructures, much of the comfort we live in and most of our food. Yet, for its production we lean heavily on resources for which the availability can be leveraged against the life and the freedom of entire nations by merciless dictators. This has to change as soon as possible.

### 1.1.1. Hydrogen applications

#### ***Ammonia production***

Ammonia production through the Haber-Bosch reaction is maybe the single most crucial chemical reaction for human prosperity, and this process alone is responsible for more or less half of the whole  $N_2$  fixation on Earth.

In the Haber-Bosch reaction, a 1:3 mixture of pure  $N_2$  and  $H_2$  is made to react at high pressure (15–25 Mpa) and high temperatures (400–450 °C) in the presence of an iron-based catalyst (commonly magnetite) in order to achieve hydrogenation of the triple bond in the nitrogen molecule ( $N_2$ ) to yield ammonia ( $NH_3$ ) (1).



The reaction proceeds via a dissociative adsorption of  $N_2$  and  $H_2$  on the catalyst surface; the nitride generated is then hydrogenated three times sequentially to form  $NH_3$ .<sup>6</sup>

The vast majority of the ammonia produced through the Haber-Bosch method is used to mass-produce fertilizers, while the rest is used as a solvent, a base or a nitrogen source in bacterial cultures. Notably, ammonia can also be used as a fuel, and is being studied as a possible solution for hydrogen storage.<sup>7, 8</sup>

#### ***Oil refining<sup>9</sup>***

Hydrogen is an indispensable reagent in the oil refining industry and it is involved in several steps of petroleum processing, aimed at making the refining process easier and at improving quality and quantity of the products obtained.

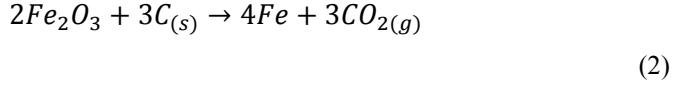
The main uses of  $H_2$  are:

- *Hydrodesulfuration*, where hydrogen is used to reduce sulfur contaminants to  $H_2S$  in order to increase the quality of the crude oil and facilitate refining.
- *Hydroisomerisation*, where long chain alkanes are catalytically transformed into branched molecules to improve fuel properties such as RON and fluidity at low temperatures.<sup>10</sup>
- *Hydrocracking*, a versatile process where C-C bonds in long-chain hydrocarbons are broken to produce lighter compounds that are then saturated by hydrogen.

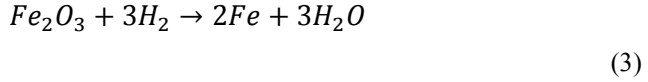
#### ***Iron ore reduction<sup>11</sup>***

Reduction of iron ore (which is composed by iron oxides such as hematite,  $Fe_2O_3$ ) is usually achieved by melting the ore into a blast furnace with coal. As the ore melts, oxygen oxidizes the carbon to  $CO_2$  and escapes the furnace (2).

The result is the so-called *pig iron*, a high-carbon intermediate in steelmaking processes.



As this procedure heavily contributes to the carbon footprint of steelmaking, the industry is developing systems to replace reduction based on carbon with reduction based on hydrogen (3)

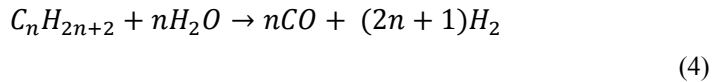


Pilot plants are being established that drive iron ore reduction in shaft furnaces using a H<sub>2</sub>/CO gas mixture, with the goal of going completely carbon-free in the next years (e.g. the HYBRIT project in northern Sweden).

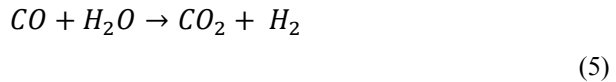
### 1.1.2. Hydrogen production methods

#### ***Steam reforming (Grey/Blue Hydrogen)***

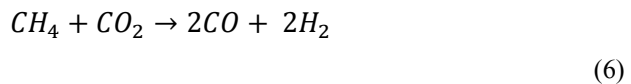
Steam reforming is the name of an industrial process where hydrocarbons (often methane, with which the process takes the name of Steam Methane Reforming, SMR) are made to react with excess steam in the presence of a nickel catalyst to produce a mixture of carbon monoxide and hydrogen gases known as syngas, according to the equation shown below (4).<sup>12, 13</sup>



Additional hydrogen is generated through the water-gas shift reaction (WGSR) (5)



A secondary reaction resulting in hydrogen production, known as CO<sub>2</sub> reforming or dry reforming (6), may also be catalyzed under process conditions.

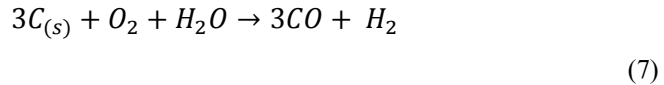


While (5) is slightly exothermic, (4) is highly endothermic and running the process requires constant heating in order to maintain the high temperatures (800–900 °C) and pressures (20-30 bar) needed. Overall, steam reforming emits 8 kg of CO for each kg of H<sub>2</sub> produced and has a relatively high energy efficiency of around 75%, that gets lowered to 60% when CCSUs are applied.<sup>14</sup> Despite its high environmental footprint, steam reforming still constitutes more than 60% of the global hydrogen production

### ***Coal gasification (Black/Brown Hydrogen)***

Coal gasification is a process that has its roots in the 18<sup>th</sup> and 19<sup>th</sup> centuries, when coal would be used to produce “town gas”, which was then distributed in pipes, and used to illuminate the streets and for other daily applications.<sup>15</sup>

The process consists of t high temperature (800 °C) oxidation of coal in the presence of controlled amounts of oxygen and water vapour to produce syngas (7).<sup>16</sup>



As in the case of steam reforming, additional hydrogen is produced through the WGSR (5).

### ***Methane pyrolysis (Turquoise Hydrogen)***

Methane pyrolysis, also known as methane decarbonization, represents one of the first and most promising routes for CO<sub>2</sub>-free hydrogen generation from a fossil fuel.<sup>17</sup>

The reaction consists in the thermal dissociation of methane, following reaction (8), and is run in the absence of oxygen to prevent CO/CO<sub>2</sub> formation.



The reaction is thought to proceed through the breaking of a C-H bond and the formation of two radical species as the first step, and to then proceed through a complex mechanism, shown in Fig. 1.3.

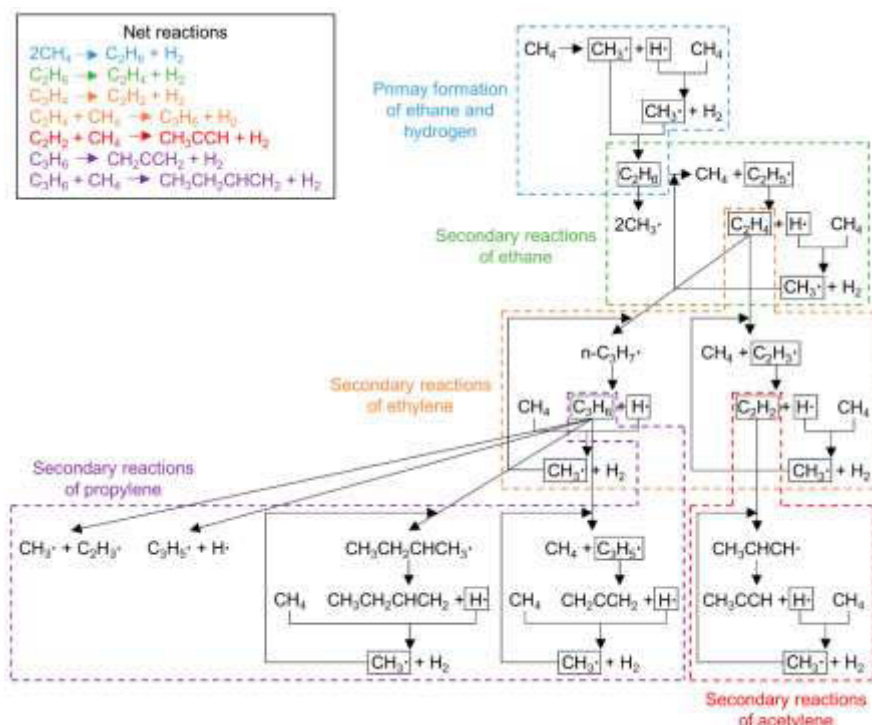


**Fig. 1.3** Proposed scheme for methane pyrolysis. Figure reprinted with permission from ref.<sup>18</sup>

The first step has a high activation energy and dictates the kinetic of the overall reaction. An acceptable rate for this reaction, if left uncatalyzed, can be achieved at 1200 °C. Catalysis using transition metals such as iron, nickel or cobalt is being developed but it is hindered by problems of catalyst deactivation due to poisoning, sintering and carbon deposition that make industrial-scale application currently not a viable option.<sup>17-19</sup>

### ***Water electrolysis (Green Hydrogen)<sup>20</sup>***

When competing for “the greenest hydrogen production method”, nothing beats water electrolysis, especially when ran using zero-emission energy (e.g. photovoltaic and wind power). Currently, it represents the cheapest way to produce pure hydrogen (that is not mixed with other gases, like CO or CO<sub>2</sub>, known to poison the catalysts used in fuel cells)<sup>21, 22</sup> but only account for ~0.03% of global production.<sup>2</sup>

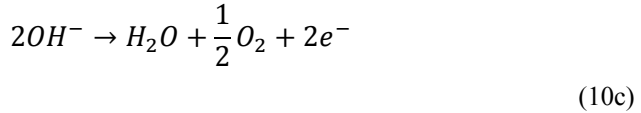
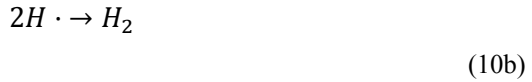
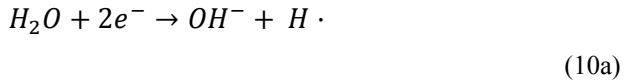
Water electrolysis fundamentally consists in running direct current through water in order to split its molecules into hydrogen and oxygen, respectively at the cathode and at the anode (9).



The two electrodes are immersed into an electrolyte solution and separated by a membrane that ensures charge transfer while preventing the recombination of produced  $O_2$  and  $H_2$  into  $H_2O$ , which would happen spontaneously.

As a mature and commercially available technology, alkaline electrolyzers are currently employed on the megawatt scale. They function by using a concentrated alkaline solution as electrolyte and non-noble metal catalysts for the electrodes. When sufficient voltage is applied, water molecules at the cathode take up one electron and are dissociated into  $OH^-$  and  $H\cdot$  (10a), with two of the latter recombining into an  $H_2$  molecule (10b).

The  $OH^-$  ions then travel to the anode where they are oxidized into water and oxygen (10c).<sup>23</sup>



### ***Why the need for a different catalyst?***

Despite being an already widely adopted technology, alkaline water electrolysis suffers from a few major drawbacks, mainly related to corrosion, and relatively low current density ( $400 \text{ mA/cm}^2$ ) and energy efficiency (70-80%). A valid alternative is represented by Proton Exchange Membrane (PEM) electrolyzer, which function by transporting the protons generated at the anode following water oxidation via a conductive membrane towards the cathode where they are subsequently reduced to  $H_2$ .<sup>23</sup> This technology is capable of reaching higher current densities (up to  $2 \text{ A/cm}^2$ ) and higher energy efficiencies (up to 90%) when compared to alkaline electrolysis.

Then what is holding this technology back? Mainly its cost.

While working, PEM electrolyzers generate a locally acidic environment that induces rapid corrosion of the electrodes materials. This limits the choice of catalysts to expensive noble metals such as platinum and palladium and drives up the manufacturing cost, which is then driven even higher by the need for expensive membrane materials.

This has driven research towards the development of cheap and efficient catalysts able to reliably function under the required acidic conditions.<sup>24</sup>

Another possible solution to problems related to corrosion is to develop water electrolysis systems that function at neutral or almost-neutral pH. These systems, though, suffer from limited current densities arising from the low conductivity of water. Moreover, as of today, catalysts able to efficiently drive both hydrogen evolution and water oxidation in this pH range are once again mostly based on precious metals: platinum and ruthenium/iridium, respectively. For hydrogen evolution, some materials based on metals like cobalt and nickel have been developed and shown to have moderate activities at neutral pH, but still low in comparison to platinum catalysts.

Luckily for us, as it is often the case, Nature is offering us a possible alternative solution to this issue, at least in relation to hydrogen evolution. All we have to do is to gain insight into and take inspiration from the wonderful machines that are [FeFe] hydrogenases.

## 1.2. [FeFe] hydrogenases

[FeFe] hydrogenases are Nature's best hydrogen-evolving and hydrogen-oxidizing catalysts, capable of reaching turnover frequencies as high as 20,000 s<sup>-1</sup>.<sup>25-27</sup> Their high proficiency and low overpotential requirement have made them some of the most interesting candidates for industrial hydrogen production. These extraordinary enzymes appear in a variety of forms and have different roles in the organisms that carry them, but they all have something in common: their active site, the H-cluster. When discussing [FeFe] hydrogenases one unavoidably focuses on this unique organometallic cofactor; its structure comprises a canonical [4Fe4S] cluster ([4Fe4S]<sub>H</sub>) linked via a cysteine residue to a di-iron subsite ([2Fe]<sub>H</sub>). What makes this cofactor special is the uncommon set of ligands that coordinate [2Fe]<sub>H</sub>: 3 CO, 2 CN<sup>-</sup> and a bridging azadithiolate (adt, <sup>-</sup>SCH<sub>2</sub>NHCH<sub>2</sub>S<sup>-</sup>) ligands.<sup>28, 29</sup> This peculiar first coordination sphere is responsible for stabilizing the iron ions in the low spin and oxidation states (Fe<sup>I</sup>/Fe<sup>II</sup>) they take during catalysis. Moreover, the amine bridgehead is conveniently placed to deliver protons to the open coordination site during hydrogen evolution or to form, together with the distal iron, the frustrated Lewis pair responsible for hydrogen splitting.

While the cysteine residue linking the [4Fe4S]<sub>H</sub> and the [2Fe]<sub>H</sub> clusters is the only protein-derived coordination ligand, the diatomic ligands' rotated geometry is stabilized by weak interactions with some fairly conserved amino-acidic residues (Fig. 1.4B).<sup>30-32</sup>

Other common structural features in [FeFe] hydrogenases are the presence of dedicated pathways for substrates delivery: a proton transfer chain composed of amino acidic residues and water molecules<sup>33-37</sup>, an electron transfer chain consisting of one or more [4Fe4S] or [2Fe2S] clusters<sup>38-42</sup>, beginning/ending with the [4Fe4S]<sub>H</sub> cluster, and one or more putative gas channels for H<sub>2</sub> diffusion (Fig. 1.4A).<sup>43-45</sup>



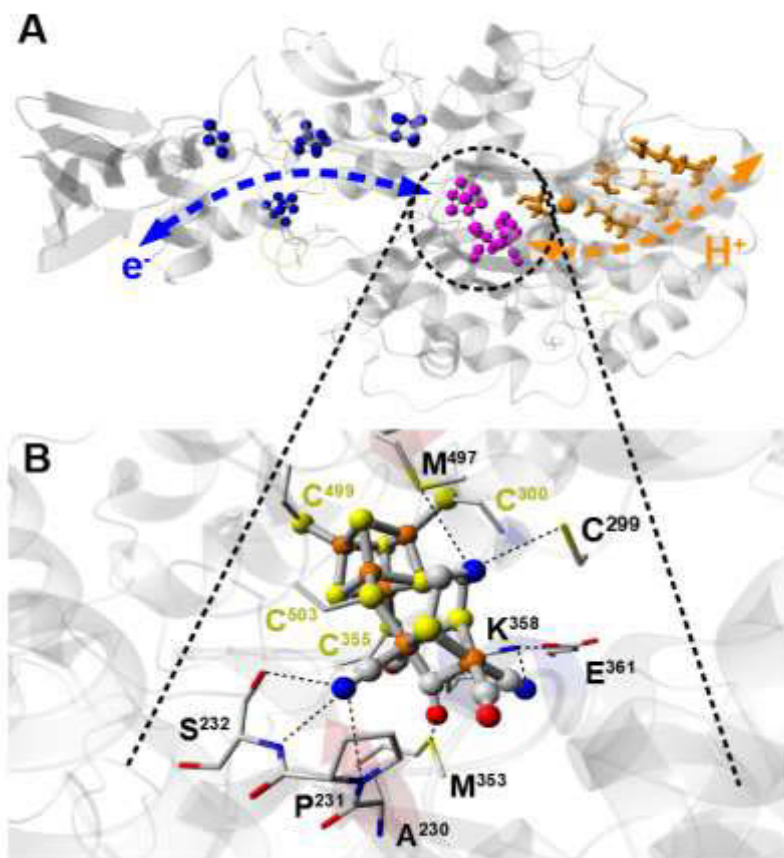


**Fig. 1.4 (A)** Illustrative representation of the substrate channels of a [FeFe] hydrogenase. The electron transfer chain is colored in blue, the amino acidic residues and water molecules belonging to the proton transfer pathway are colored in orange, and the H-cluster is colored in purple. **(B)** Graphical representation of the H-cluster, including key amino acids. Weak interactions between the H-cluster ligands and the surround residues are represented by dashed lines. Elements coloring is based on the following scheme: Fe = orange, S = yellow, C = grey, N = blue, O = red. Both panels and the residues numbering are based on the enzyme from *Clostridium pasteurianum* Cpl (1.63 Å resolution, PDB ascension code 4XDC)<sup>46</sup>. Adapted with permission from ref.<sup>47</sup>

The biosynthesis of the peculiar  $[2\text{Fe}]_{\text{H}}$  subsite relies on a well conserved machinery consisting of three enzymes (HydG, HydE and HydF) referred to as maturases. The proposed mechanism begins with the assembly of two  $\text{Fe}^{\text{II}}(\text{CO})_2(\text{CN})(\text{Cys})$  precursors, called synthons, by the radical-SAM enzyme HydG.<sup>48</sup> These mononuclear precursors are then assembled by HydE (another radical-SAM enzyme) and the bridging adt ligand is formed using a serine as a donor for the  $\text{NH}(\text{CH}_2)_2$  moiety, yielding a  $\text{Fe}_2(\text{adt})(\text{CO})_4(\text{CN})_2^{2-}$  precursor

on the scaffold HydF.<sup>49-51</sup> Finally, HydF delivers the precursor to an un-matured hydrogenase, only carrying the [4Fe4S]<sub>H</sub> cluster (called *apo*-hydrogenase).<sup>52, 53</sup>

The discovery that this complex machinery could be circumvented, and that [FeFe] hydrogenases could be matured by loading a synthetic mimic of the final precursor on HydF or directly onto an *apo*-hydrogenase, in a process named artificial maturation, has allowed for easier heterologous expression and purification of these enzymes.<sup>28, 54</sup> Moreover, it has opened the door for the generation of variants of the H-cluster based on the insertion of different di- and monoatomic iron ligands with interesting spectroscopic and functional properties.<sup>55</sup>

In the following sections, I will talk about [FeFe] hydrogenases distribution across biological domains, describe the mechanism by which they operate and discuss the obstacles that limit our ability to utilize them on a large scale.

### 1.2.1. Diversity in the world of hydrogenases

[FeFe] hydrogenases represent one of the three separate families of hydrogenases that have been identified so far, the others being [NiFe] hydrogenases and Fe-only hydrogenases.<sup>56</sup> While Fe-only hydrogenases are mostly involved in hydride transfer reactions, [NiFe] hydrogenases catalyze hydrogen evolution and oxidation reactions and, despite being known for being less fast, they receive a lot of attention for being more oxygen tolerant than their [FeFe] counterparts. As the title of this thesis implies, in this section I will focus on the evolutionary diversity of [FeFe] hydrogenases, but the interested reader can find information on the [NiFe] hydrogenases' classification and diversity across life's domains in references<sup>57</sup> and<sup>58</sup>.

[FeFe] hydrogenases can be found in many organisms across the bacteria and eukarya domains, especially in obligate anaerobes. These enzymes have been classified based on their domain structure and are conventionally divided into 4 phylogenetically distinct groups, each divided into several subclasses.<sup>39, 59</sup>

- **Group A** is the most well known class and includes the most proficient H<sub>2</sub>-evolving enzymes, including the model hydrogenases from the green alga *Chlamydomonas reinhardtii* (CrHydA1), the sulfate-reducing bacteria *Desulfovibrio desulfuricans* (DdHydAB) and the bacillus *Clostridium pasteurianum* (CpI). Enzymes belonging to this class often use ferredoxins as redox partners and function as H<sub>2</sub>-producers during anaerobic fermentation of reserve carbohydrates or small organic acids. In some organisms, like in many species of the genus *Desulfovibrio*, group A hydrogenases function as H<sub>2</sub> oxidizers during heterotrophic and mixotrophic growth.<sup>60</sup> A few of the members of this group, though, are known as bifurcating enzymes and work with both ferredoxins or NAD(P)H as their redox partner. These enzymes work by exploiting the exergonic reduction of protons using

electrons provided by ferredoxins to drive the endergonic reduction of protons using electrons coming from the oxidation of NAD(P)H. This mechanism represents an efficient energy conservation strategy and allows for the production of H<sub>2</sub> while salvaging energy to generate an extra ATP molecule.

- **Group B** is the least known of the classes, as no representatives from it has been characterized yet. Despite being phylogenetically distinct from group A enzymes, group B enzymes display fairly conserved amino acidic motifs around the H-cluster.
- **Group C** is considered the “sensory hydrogenases” group, as many of its members have been assigned a sensory role based on the presence of a PAS domain, which is a common sensor domain that can be found across basically all life forms.<sup>61</sup> Their genomic localizations, upstream to other hydrogenases, supports their regulatory role, as do the catalytic properties (high affinity for H<sub>2</sub> and low catalytic rates) reported for the group C member *TmHydS*.<sup>62</sup>
- **Group D** is another mysterious group as its members lack a PAS domain but display similar genomic localizations and domain structures as those in the group C subclass. To date only a single member has been isolated, from the bacterium *Thermoanaerobacter mathranii* (*TamHydS*)<sup>30</sup>.

Other than defining class membership, the domain structure of [FeFe] hydrogenases can have a considerable effect on its catalytical properties. Many enzymes possess domains that bind additional [4Fe4S] clusters, respectively called F-domains and F-clusters. These clusters act as an entry point for electrons coming from ferredoxins and have been shown to exert long-range influences over many catalytical properties: these include tuning the catalytic bias by acting on the active site’s thermodynamical potential<sup>40, 41</sup> and influencing protonation events of the H-cluster<sup>42</sup>.

The astonishing structural diversity of [FeFe] hydrogenases challenges our beliefs about being able to understand the way these enzymes function. Structures that seem extremely well conserved in group A model hydrogenases, such as second-coordination sphere amino acids and the proton transfer pathway cease to be “conserved” when groups B-D are taken into consideration. The role of the conserved amino acids in the active site pocket is thought to go beyond a simple structural role and they are involved in directly modulating electronic and catalytic properties of the H-cluster.<sup>63-65</sup> The observation that common conserved motifs, such as the APA motif next to the proximal iron<sup>31</sup> and the methionine interacting with the  $\mu$ CO ligand, appear not to be as well conserved outside of group A poses questions on the role that these second-coordination sphere interactions have in assisting the catalytic cycle.

Moreover, for group C hydrogenases an alternative proton transfer pathway was proposed, as two key amino acids belonging to the canonical one are not found to be conserved.<sup>62</sup> A similar argument was made for group D hydrogenases.<sup>30</sup>

Overall, [FeFe] hydrogenases' diversity seems to represent an almost entirely untapped resource that we can still explore in search for a deeper understanding of the inner workings of these extraordinary catalysts and for novel enzymes with new and exciting properties to investigate.

### 1.2.2. The proposed catalytic cycle

The combination of several spectroscopic, with EPR and FTIR doing the lion's share, and electrochemical techniques has allowed the scientific community to gain a considerable understanding of the [FeFe] hydrogenases' catalytic cycle. I will now briefly illustrate the main intermediates included in the currently accepted model, shown in Fig.1.5.

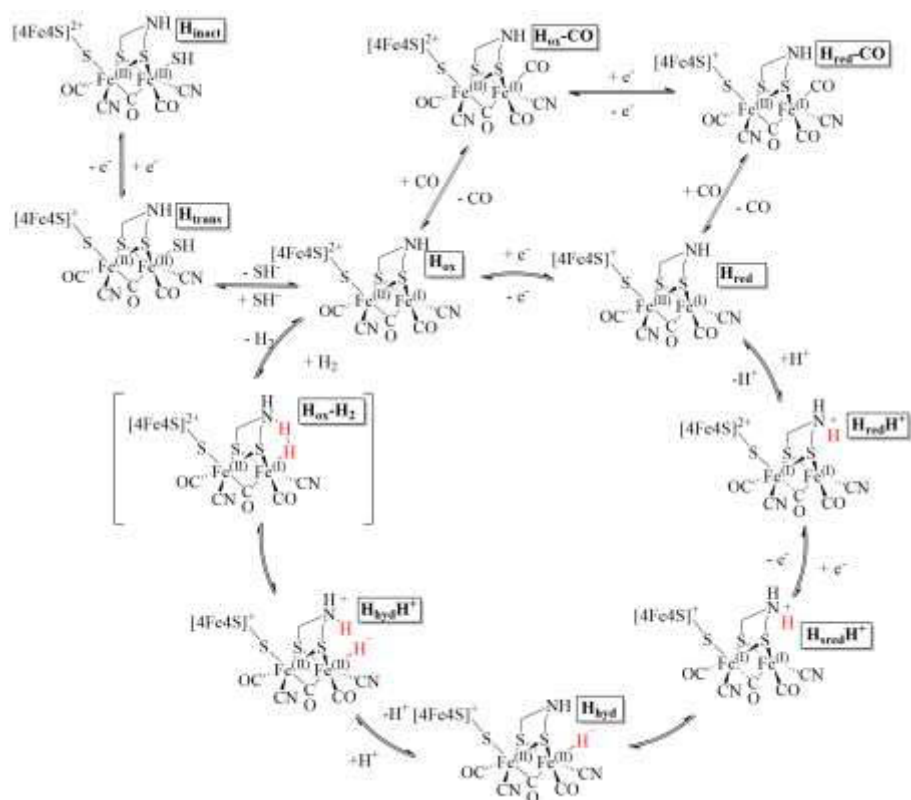
The most oxidized catalytically relevant intermediate of the cycle is called  $H_{ox}$  and it is generally considered to be the physiological "resting state" for these enzymes. Concerning the electronic structure,  $H_{ox}$  is assigned an oxidized  $[4Fe4S]_H$  cluster and a mixed valence  $[2Fe]_H$  subsite, with the proximal ( $Fe_p$ ) and distal ( $Fe_d$ ) irons, respectively, in an  $Fe^{II}$  and  $Fe^I$  oxidation state. This assignment is consistent with EPR data, that show a narrow rhombic signal compatible with a paramagnetic center located on  $[2Fe]_H$ , and with recent computational and  $^{13}C/^{15}N$  Mims ENDOR studies.<sup>66</sup>

The first reduced state,  $H_{red}$ , is reached following a one-electron reduction of  $H_{ox}$ . This intermediate can be observed at high pH and is best described as a reduced  $[4Fe4S]_H$  coupled to  $[2Fe]_H$  still in a mixed valence  $Fe^I$ - $Fe^{II}$  state.<sup>67</sup> This electronic structure is supported by the limited red-shift ( $5-10\text{ cm}^{-1}$ ) observed in the FTIR spectrum as compared to  $H_{ox}$ , which is indeed compatible with the extra electron being located relatively far from the CO and  $CN^-$  ligands. No EPR signature is reported for this intermediate, as the two paramagnetic centers are strongly coupled and yield an EPR-silent species.

When  $H_{red}$  is protonated on the bridgehead amine, the  $H_{red}H^+$  intermediate is formed.<sup>67</sup> It is noteworthy that this state can also form directly from  $H_{ox}$  at low pH following a proton-coupled electron transfer (PCET) event.  $H_{red}H^+$  remains EPR-silent, but FTIR shows that the protonation event triggers an electronic rearrangement, with one electron moving from the  $[4Fe4S]_H$  to the  $[2Fe]_H$  subsite. This is visible as a strong red-shift of the CO and  $CN^-$  bands, indeed consistent with a  $Fe^I$ - $Fe^I$  oxidation state of the di-iron moiety.

A second one-electron reduction yields the  $H_{sred}H^+$  state, with a reduced  $[4Fe4S]_H$  next to a di-iron subsite still in an  $Fe^I$ - $Fe^I$  state.<sup>29</sup> Interestingly, the reported FTIR signature for  $H_{red}H^+$  and  $H_{sred}H^+$  state lack a bridging CO ( $\mu CO$ ) band and has an extra terminal CO (t-CO) band, a fact that has been attributed

At this point, the two electrons and the proton that have accumulated on the H-cluster to form the  $\text{H}_{\text{sred}}\text{H}^+$  state combine and form a terminally-bound hydride ligand, generating the  $\text{H}_{\text{hyd}}$  state, which formally sports a reduced  $[\text{4Fe4S}]_{\text{H}}$  cluster and  $\text{Fe}^{\text{II}}\text{-Fe}^{\text{II}}$  di-iron subsite. The presence of a terminally bound hydride ligand has been confirmed by various spectroscopies, including FTIR, NVRS,  $^1\text{H}$ -NMR and Mössbauer.<sup>72-75</sup>



The final step is another protonation event on the bridgehead amine to yield the  $\text{H}_{\text{hyd}}\text{H}^+$  state.<sup>76</sup> The additional proton reacts then with the hydride ligand to form  $\text{H}_2$  and regenerate the  $\text{H}_{\text{ox}}$  state, which is then able to restart the cycle.

### 1.2.3. Inhibition

Outside of the catalytic cycle, several inhibited states have been identified, traceable to three main inhibitors:  $\text{HS}^-$ , CO and  $\text{O}_2$  (Fig. 1.5)

The sulfide-bound state  $\text{H}_{\text{inact}}$  was first identified following the aerobic purification of the [FeFe] hydrogenase of *Desulfovibrio vulgaris* (DvH).<sup>77, 78</sup> This state displays an oxidized  $[\text{4Fe4S}]_{\text{H}}$  cluster with an  $\text{Fe}^{\text{II}}\text{-Fe}^{\text{II}} [\text{2Fe}]_{\text{H}}$  subsite and it could be reactivated with a one-electron reduction to  $\text{H}_{\text{ox}}$ , going through an intermediate state called  $\text{H}_{\text{trans}}$ , isoelectronic to  $\text{H}_{\text{ox}}$ .

Initially the identity of the inhibitory ligand for these states was not clear, and it was only recently that its identity has been ascertained and assigned to sulfide.<sup>79, 80</sup> These states have sparked interest in the community as reversible sulfur inhibition appears to be a viable strategy to provide oxygen protection to [FeFe] hydrogenases.<sup>81-83</sup>

Carbon monoxide is a well-known inhibitor for mixed-valence H-cluster states, as it binds to  $\text{H}_{\text{ox}}$  and  $\text{H}_{\text{red}}$  to generate  $\text{H}_{\text{ox}}\text{-CO}$  and  $\text{H}_{\text{red}}\text{-CO}$ .<sup>84</sup> Interestingly, H-cluster susceptibility to CO-binding varies across different classes of [FeFe] hydrogenases, with for instance classes C and D's putative sensory hydrogenases showing a relatively low affinity for this inhibitor.<sup>30, 62</sup> As such, it is possible that the active-site pocket has a strong influence on CO-binding.

Molecular oxygen is maybe the most infamous inhibitor of [FeFe] hydrogenases. These enzymes are indeed famous for their oxygen sensitivity, and exposure to sub-atmospherical amounts of  $\text{O}_2$  usually results in H-cluster degradation and complete loss of function on a time scale of minutes.<sup>43, 85</sup> Interestingly, one can sometimes find exceptions to the rule and, as we mentioned above, sulfur binding seems to be a viable strategy for oxygen-damage prevention. The most interesting example is represented by the [FeFe] hydrogenase from *Clostridium beijerinckii*, that is able to use a cysteine residue nearby the open coordination site of the H-cluster as a “safety cap” to protect itself from oxygen damage.<sup>83</sup>

### 1.2.4. Outlook

For being enzymes that catalyze a relatively simple reaction, the [FeFe] hydrogenases mechanism has proven to be quite difficult to unveil. Despite the model presented in Section 1.2.2. being generally accepted, and time-resolved spectroscopy having supported the relevance of many of its intermediate states<sup>86</sup> there are still a few open questions and problems related to it.

A first consideration is that, while the aforementioned model of the catalytic cycle is considered to be applicable to all hydrogenases, it was developed exclusively based on experiments performed on model enzymes belonging to group A. As more and more hydrogenases from other groups are being char-

acterized, displaying peculiar characteristics in terms of structural and catalytic properties, it becomes legitimate to wonder about how much “general” this model can be considered.

Regarding the details of the catalytic cycle, the chemical interpretation of the  $H_{\text{red}}H^+$  and  $H_{\text{sred}}H^+$  states is still a topic of discussion. Following the initial observation of a lack of a bridging CO ligand and the appearance of an additional terminal CO band (as we mentioned in section 1.2.2.), these two states have been assigned to an H-cluster configuration carrying an  $Fe^I$ - $Fe^I$  di-iron subsite bound to a bridging-hydride ligand, and with a CO ligand moved to an apical position on the distal iron. This assignment has been supported by X-Ray spectroscopy data and DFT calculations.<sup>87-89</sup> Bridging-hydride intermediates are supposed to be thermodynamically more stable than their terminal-hydride counterparts, but the transitions to these states (and, consequently, out of these states) are unfavourable due to high kinetic barriers; thus, bridging-hydride species are implied to be catalytically inactive, or at least poorly active. Consequently, the protein enforces and stabilizes an inverted square-pyramid ligand conformation on the distal iron, with a bridging CO and an open coordination site in the apical position.<sup>90</sup>

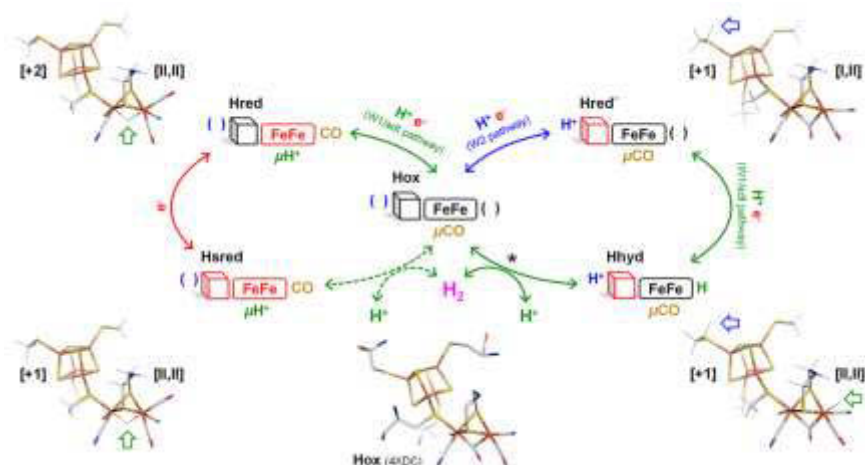


**Fig. 1.6** Alternative catalytic model, as proposed by Haumann and Stripp in ref.<sup>91</sup> The right branch represents the more proficient catalytic cycle, proceeding through bridging-CO intermediates thanks to a water-mediated PCET on one of the  $[\text{4Fe4S}]_{\text{H}}$ -coordinating cysteines (W2 pathway). The left branch represents the slow-turnover secondary cycle, proceeding through bridging-hydride intermediates following a protonation event on the  $[\text{2Fe}]_{\text{H}}$  subsite (W1/adt pathway). Reprinted with permission from ref.<sup>91</sup>

In this alternative model, therefore, both  $\text{H}_{\text{red}}\text{H}^+$  and  $\text{H}_{\text{sred}}\text{H}^+$  (here named  $\text{H}_{\text{red}}$  and  $\text{H}_{\text{sred}}$ ) have been placed onto a slow-turnover secondary catalytic branch (Fig. 1.6).<sup>91</sup> To prevent the active site from entering these states during catalysis, this model proposes the occurrence of a PCET event upon  $\text{H}_{\text{ox}}$  reduction, involving the protonation of one of the  $[\text{4Fe4S}]_{\text{H}}$ -coordinating cysteines. This protonation event would then prevent the electron from moving to the  $[\text{2Fe}]_{\text{H}}$  subsite prematurely and from triggering the rearrangement into the  $\text{H}_{\text{red}}$  state following a protonation on the  $[\text{2Fe}]_{\text{H}}$  subsite.

The models proposed hereupon and in section 1.2.2 seem to contradict each other, but as pointed out recently by Lampret and coworkers, our understanding of the catalytic cycle as a single monolytic circular pathway might be incorrect.<sup>92</sup> External conditions can influence which steps the enzyme takes while turning over in either direction by making more or less likely the occurrence of a concerted PCET.

Keeping in mind this consideration, one can wonder how well all the conclusions drawn about the  $[\text{FeFe}]$  hydrogenases' mechanism studying the enzyme *in vitro* can be transported over into its mechanism *in vivo*.

Finally, and exciting perspective in  $[\text{FeFe}]$  hydrogenase research is the study of enzyme variants obtained *via* artificial maturation using non-native cofactor, trying to develop semi-artificial hydrogenases with better properties (e.g. lower sensitivity towards inhibitors) than their natural counterparts.



### 1.3. Back to the cell

Compared to the dilute, well-defined and well-mixed environment that enzymes find themselves in when investigated *in vitro*, the cell interior can be – in a not-too-scientifical way – defined as “a mess”.

The first reason behind the earlier statement is that the cytoplasm of *E. coli* is crowded, as it contains more than 4000 different types of protein, with a total concentration of 3-400 mg/ml and occupying 20-30% of the cell volume on average.<sup>93-95</sup>

The effect of this cellular crowding has been named the “volume exclusion effect”. In a simple model where identical macromolecules are represented by spheres, the minimum distance between the centers of two macromolecules is determined by their radii. Effectively, around each macromolecule there is a volume from which the centers of other macromolecules are excluded, or in other words there is a space that other macromolecules cannot occupy (Fig 1.7).

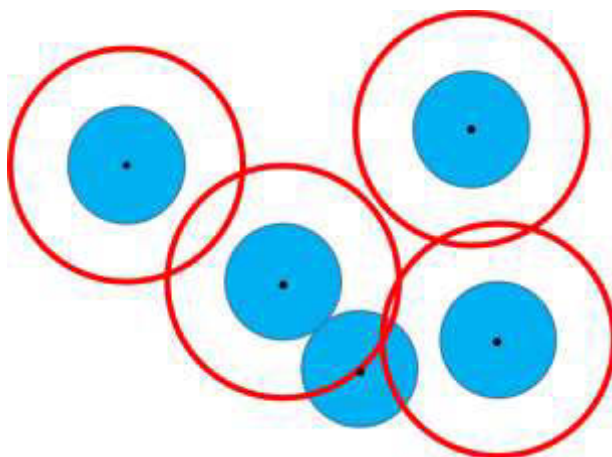


**Fig. 1.7** Representation of the volume exclusion effect. Light blue circles represent macromolecules, red circles delimit the excluded volume.

The more macromolecules are present in a certain region of space, the less volume is available to them: this has the effect of reducing the number of ways these molecules can be arranged, therefore increasing the free energy of the solution by lowering the entropy of the system.<sup>96</sup> Volume exclusion results in an increase of the effective concentration of the species which in turn is reflected in an increase of their thermodynamic activity. All of these phenomena will for instance influence the rate of processes that depend on oligomerization or, in general, of any process that results in the increase or decrease of the excluded volume. Folding in particular can both be influenced by this entropic effect and by the enthalpic contribution of weak interactions occurring between the folding peptide and the crowding agents.<sup>96</sup>

Another important effect of crowding is an up to 10-fold reduction of diffusion rates, both for small and big molecules. As diffusion rates relate directly to the probability of encounter between molecules, crowding can influence the kinetics of many reactions, in particular of diffusion-limited ones.<sup>95,97</sup>

With the exception of a few research fields (with the most known being the study of protein-DNA interactions), historically not many works have supported the physiological relevance of their results with studies on the effect of crowding. We will see in section 1.3.1. how in recent years the development of whole-cell spectroscopic techniques has started filling in these gaps.

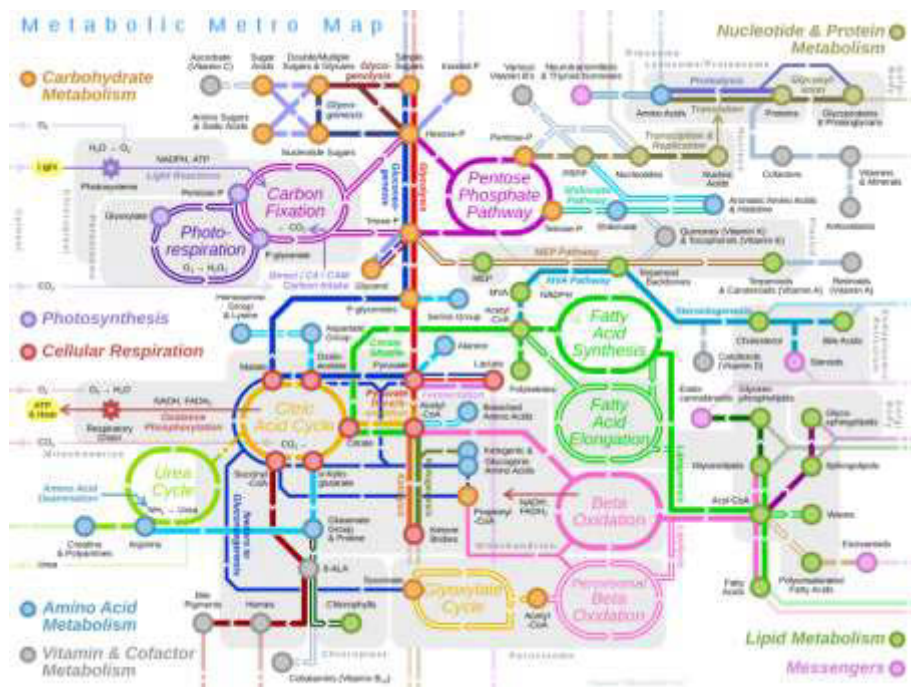


**Fig. 1.8** The “Metabolic Metro Map”. This figure gives a glimpse of the complex network of reaction that take place inside a living cell. Reproduced under Creative Commons licence from Wikipedia. Credits to Bert Chan.

The study of crowding effects is arguably also a relevant issue in [FeFe] hydrogenase research, where for instance  $H_{red}$  state formation is thought to depend on intermolecular electron-transfer between hydrogenase molecules and is hindered when the enzyme is diluted into a BSA protein solution;<sup>98</sup> an observation that raises questions over the relevance of this state in the *in vivo* catalytic mechanism.

The second reason that makes the intracellular environment “a mess” is that a living cell consists in a massively complex network of finely regulated chemical reactions (Fig. 1.8). As the intracellular environment is intricate and poorly-defined, interpretation of spectroscopic results obtained under whole-

cell conditions can be difficult. Moreover, as we will see in sections 1.3.2. and 1.3.3, the presence of a complex metabolism can be considered to some extent a double-edged sword when it comes to using whole-cell catalysts. On one hand, a living cell can fit many useful biochemical pathways that allow for multi-step catalysis, enzyme and cofactor regeneration, and protection from harsh environmental conditions and from external inhibitors thanks to the cell membrane and to the homeostatic processes. On the other hand, an enzyme surrounded by a cell envelope is intrinsically less accessible and its surroundings are harder to manipulate for the experimentalist; also, an enzyme's efficiency can be hampered by other reaction pathways competing with it for substrates/cofactors or generating inhibitors.

### 1.3.1. Whole cell spectroscopy

The importance of being able to study proteins in their native environment has been recognized at least since the early 90s, when GFP could be expressed fused with proteins and used as a label for fluorescence microscopy to follow its cellular localization and its interaction with other fluorescent targets,<sup>99</sup> eventually developing techniques exploiting phenomena such as FRET.<sup>100</sup>

The drive to learn more about the biological function of proteins has led to the development of whole-cell applications for also more powerful spectroscopic techniques, namely NMR and EPR.

In so-called “in-cell NMR”, overexpression and isotopical labeling of the target protein is often enough to achieve an acceptable signal-to-background ratio, and it is achieved either by media enrichment or through the use of amino acid-specific probes.<sup>101-104</sup> When this approach is not feasible (e.g. for eucaryotic cells) the target protein can be labeled and purified heterologously, and then introduced into the cell via different methods, including microinjection<sup>105</sup> or the use of pore-inducing toxins.<sup>106</sup>

In-cell NMR has proven to be a valuable tool for structural biology, allowing for the study of phenomena that are much more significant when investigated inside a cell. One of the most common topics is protein folding, where NMR can be used by exploiting the fact that in the cytoplasm globular proteins tumble much more slowly than their disordered/unfolded counterparts, allowing for distinction based on signal broadening. In-cell NMR has also seen application in studying post-translational modifications and degradation dynamics *in vivo*, and in investigating how drug import, localization and target-specificity are influenced by the intracellular environment.<sup>101</sup>

As it is often the case for NMR, also its in-cell version's main limitation is the molecular size of molecules and complexes that can be studied with it.

In-cell EPR is instead based on selective labeling of targets using spin-labels and measuring their relative distances (a technique known as DEER) as a tool to study conformational dynamics of proteins or nucleic acids (Fig. 1.9).<sup>107</sup>

Compared to in-cell NMR, EPR is more sensitive (at higher bands, a few microliters of 50  $\mu\text{M}$  sample are enough) and has no size limitations. Moreover, as EPR specifically detects only paramagnetic species, the impact of background signals is often negligible.

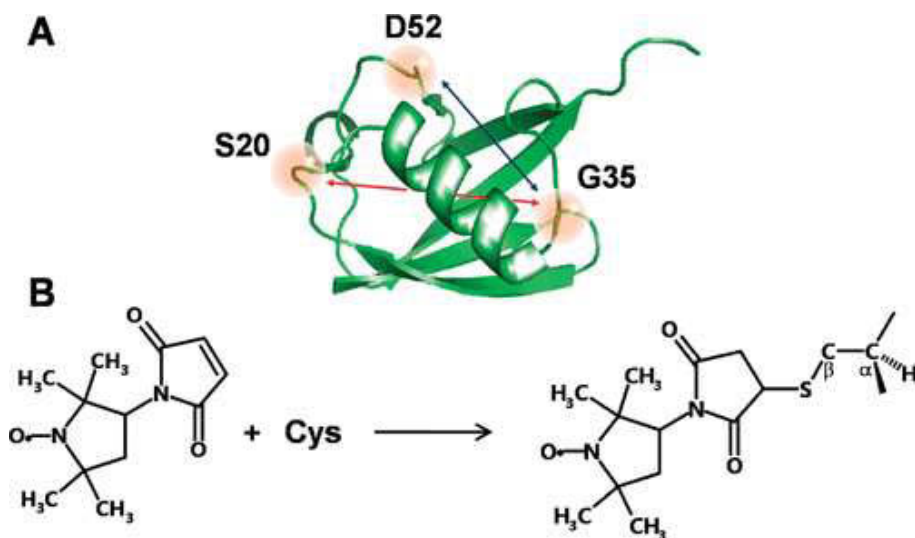


**Fig. 1.9** Spin labeling of a target protein for in-cell EPR. (A) selected amino acids are mutated into cysteines and (B) made to react in vitro with 3-maleimido-PROXYL for spin labeling. Distances between the chosen sites can be monitored with a DEER experiment. Printed with permission from ref.<sup>108</sup>

For in-cell EPR, proteins are generally labeled in vitro and introduced into cells with methods analogous to the ones used for in-cell NMR.

A new, milder and more elegant, approach is based on direct expression of labeled proteins by introducing into the host's genetic code the tRNA for a noncanonical spin-labeled aminoacid, with only a minimal impact on cell viability.<sup>109</sup> The most widely used spin labels are based on the nitroxide radical, due to their localized paramagnetic center and responsiveness to surrounding conditions, but they suffer from limited sensitivity at lower bands and instability in the cellular environment.<sup>110</sup> Therefore, lanthanide-based ( $\text{Gd}^{\text{III}}$ ) labels, being more stable intracellularly, are being developed for in-cell EPR applications.<sup>111</sup>

For “naturally” paramagnetic molecules, such as bioradicals and enzymes with transition-metals cofactors, a form of in-cell EPR can be performed without the need for labeling. An example for this approach has been recently reported for [FeFe] hydrogenases, where spectroscopically relevant amounts of mature *Chlamydomonas reinhardtii* HydA1 have been generated by artificial maturation inside the cytoplasm of *E. coli* and detected with X-band cwEPR.<sup>112</sup>

### 1.3.2. Whole-cell biocatalysis

Exploiting life's ability to synthesize complex molecules starting from basic building blocks, and to do that with astounding regio- and stereoselectivity, has been a tantalizing prospect for chemists and chemical industries. As mentioned before, living cells represent in some ways the ideal instrument to pursue this goal, with their ability to perform cascade reactions, shield catalysts from adverse environmental conditions and regenerate both catalysts and co-factors. Moreover, Nature has optimized biological catalyst to function in mild conditions, which is an attractive feature for the development of green chemistry processes. Today, whole-cell biocatalysis is being used for producing various chemicals and nutraceuticals, and research is focused on improving the efficiency of the exploited natural pathways and on introducing new ones with synthetic biology.<sup>113-116</sup>

There are two approaches to whole-cell biocatalysis that push the boundaries of "natural" processes towards the concept of semi-artificial catalysis.

The first approach consists in introducing into a living cell an artificial enzyme, with the goal of achieving new-to-nature types of catalysis.<sup>117-119</sup> A good example of this approach is represented by the work of Jeschek and colleagues, who developed an artificial metalloenzyme based on a streptavidine scaffold and a biotinilated ruthenium-based synthetic catalyst and used it to perform olefin metathesis in the periplasm of *E. coli* cells.<sup>120</sup> Another example can be found in the work of Drienovská and coworkers, who used genetic code expansion to introduce bipyridyl alanine residues into the transcription factor LmrR. Upon copper binding, the resulting enzyme was able to catalyze Friedel-Crafts alkylation in-cell.<sup>121</sup> As a final example, falling into the hydrogen production field, Naughton et al. have reported the successful in-cell assembly of an artificial enzyme consisting in a Ni-substituted rubredoxin. Co-factor insertion is obtained taking advantage of a native machinery, and the enzyme behaves as a structural and functional analogue of a [NiFe] hydrogenase.<sup>122</sup>

A second approach aims at matching the properties of biocatalysts with the efficiency of artificial light-harvesting systems, generating semi-artificial photocatalytic systems.<sup>123, 124</sup> This strategy has been explored extensively in the fields of solar fuels production and carbon fixation, using both inorganic and organic photosensitizers. For instance, the Wood-Ljungdahl pathway in *Moorella thermoacetica* has been exploited to fix CO<sub>2</sub> into acetate, using gold nanoparticles as photoexciters.<sup>125</sup> In the archeobacterium *Methanosarcina barkeri*, exposure to cadmium ions triggers a defense response and causes the precipitation of Cd/S nanoparticles. These can act as photosensitizers and have been used to directly convert CO<sub>2</sub> into CH<sub>4</sub>.<sup>126</sup> As a final example, the organic dye eosin Y has been used to drive P450-catalyzed reactions into *E. coli* cells,<sup>127</sup> and used in conjunction with the proteobacterium *Shewanella oneidensis* to produce many small molecules including H<sub>2</sub>.<sup>128</sup>

### 1.3.3 Summary

As we have seen in the previous section, whole-cell approaches represent a very promising direction for both fundamental and applied research.

The main drawback is represented by the complexity of the intracellular media. When it comes to biocatalysis, homeostatic processes actively push back against attempts to steer the metabolism towards productions of desired molecules. Also introducing artificial complexes into a cell can prove to be a challenging task, as the cell membrane could prove to be a hardly penetrable barrier for specific groups of molecules. Moreover, any artificial complex introduced into a cell, be it a spin-label, an artificial cofactor or an artificial photosensitizer, will be subject to degradation and inhibition from metabolites.<sup>110, 129</sup>

More generally, living cells can be complex objects to analyze as they perform many reactions simultaneously and exist in a constant exchange relationship with the surrounding environment. This means that they influence and are influenced by many variables of the system they find themselves in, which can make process optimization more arduous.

## 1.4. Foreword

In the following chapters I will describe the work performed during my time as a PhD student, and I will show how this work contributed to several of the challenges and open questions regarding [FeFe] hydrogenases mentioned in this introduction.

In Chapters 2 and 3, I will show our efforts in the context of whole-cell spectroscopic studies of [FeFe] hydrogenases, and how we used this approach to gain insight onto the catalytic cycle and on the stability of the H-cluster under intracellular conditions.

In Chapter 4, I will present a possible approach for solving the intricate puzzle of whole-cell photocatalytic systems and to get leads for optimization of these set-ups.

In Chapter 5, I will present the characterization of a monoCN variant of the H-cluster, performed on two different hydrogenase scaffolds. This will provide the opportunity to discuss about the role of the scaffold in tuning the structural and catalytical properties of the H-cluster.

I hope that, for the reader, this thesis about [FeFe] hydrogenases will be a pleasant walk along the new roads that stretch out in front of these ancient enzymes.

## Chapter 2 - Paper I:

# Spectroscopic investigations under whole-cell conditions provide new insight into the metal hydride chemistry of [FeFe]-hydrogenase

### 2.1. Introduction and motivation.

As we discussed in Sections 1.2.2. and 1.3., the relevance of some of the proposed catalytic intermediates in the [FeFe] hydrogenases' cycle that have been identified over the years is still sometimes challenged. The non-physiological conditions in which many of these intermediates have been isolated and studied have instilled the doubt that some of these states might be artifacts or non relevant dead-end species.

The discovery that it was possible to obtain a mature [FeFe] hydrogenase inside bacterial cells, in amounts sufficient for many spectroscopic techniques, opened up a new way to shed light on this challenging question.<sup>112, 130, 131</sup>

Therefore, in this study, we artificially matured the algal [FeFe] hydrogenase from *Chlamydomonas reinhardtii* (CrHydA1) inside *E. coli* cells and we used EPR and ATR-FTIR spectroscopy to monitor the catalytic cycle under whole-cell conditions, trying to identify which intermediates can be observed and accumulated under mild physiological conditions.

### 2.2. Generation of a functional CrHydA1 enzyme under whole-cell condition.

The first step was of course the generation of CrHydA1 in *E. coli*. For this purpose, we used a BL21(DE3) strain transformed with a pETDUET plasmid carrying the sequence for CrHydA and grown on M9 minimal media supplemented with an iron source. As the genes for the maturation machinery were not expressed in parallel, the result was an enzyme carrying the [4Fe4S]<sub>H</sub> cluster, that in *E. coli* is incorporated by the non-specific Isc machinery<sup>132</sup>, but lacking the [2Fe]<sub>H</sub> subsite (herein named *apo*-HydA1).

At this stage, an EPR sample consisting of a suspension of these *E. coli* cells only displays an ill-defined broad signal around  $g = 2$ , attributable to *apo*-HydA1 and to other iron-containing proteins present in the strain (Fig. 2.1A).



Following expression, the cells were harvested, resuspended in fresh M9 media and incubated in anaerobically sealed vials with various amounts of a synthetic mimic of  $[2\text{Fe}]_{\text{H}}$  ( $2\text{Fe}(\text{adt})(\text{CO})_4(\text{CN})_2^{2-}$ ,  $[2\text{Fe}]^{\text{adt}}$ ). The formation of  $[2\text{Fe}]^{\text{adt}}\text{-CrHydA1}$  could be monitored via EPR spectroscopy as the H-cluster signal was found to be increasing with the amount of mimic provided (Fig. 2.1A and 2.1B). The signal appeared composed of one rhombic ( $g_{\text{zyx}} = 2.100$ ; 2.040; 1.996) and one axial ( $g_{\parallel\perp} = 2.054$ ; 2.007) component, with the latter being more predominant as higher amounts of  $[2\text{Fe}]^{\text{adt}}$  were used for the maturation. Based on the spectral signatures reported for isolated *CrHydA1*, the two components were assigned, respectively, to the  $\text{H}_{\text{ox}}$  (reported signature:  $g_{\text{zyx}} = 2.102$ , 2.040, 1.998)<sup>133</sup> and  $\text{H}_{\text{ox}}\text{-CO}$  (reported signature:  $g_{\parallel\perp} = 2.052$ , 2.007)<sup>133</sup> states. Interestingly, the signals recorded under-whole cell conditions are in good agreement with their “isolated” counterparts; we reported differences in  $g$ -values on the third decimal, a variance that can be attributed to the effect of the intracellular environment on the overall structure of the enzyme.

The predominance of the  $\text{H}_{\text{ox}}\text{-CO}$  in connection to higher amounts of  $[2\text{Fe}]^{\text{adt}}$  being used for maturation can be attributed to the release of CO molecules following cofactor insertion or to degradation of excess mimic.

The confirmation that what we were generating was a functional  $[\text{FeFe}]$  hydrogenase came from the measurement of hydrogen being produced by the cell suspensions following incubation with  $[2\text{Fe}]^{\text{adt}}$  and accumulating in the vials’ headspace. The amount of hydrogen produced increased with the amount of non-CO-inhibited H-cluster signal measured in EPR (Fig. 2.1B and 2.1C), which confirmed that the enzyme matured in whole-cell conditions was capable of performing catalysis.

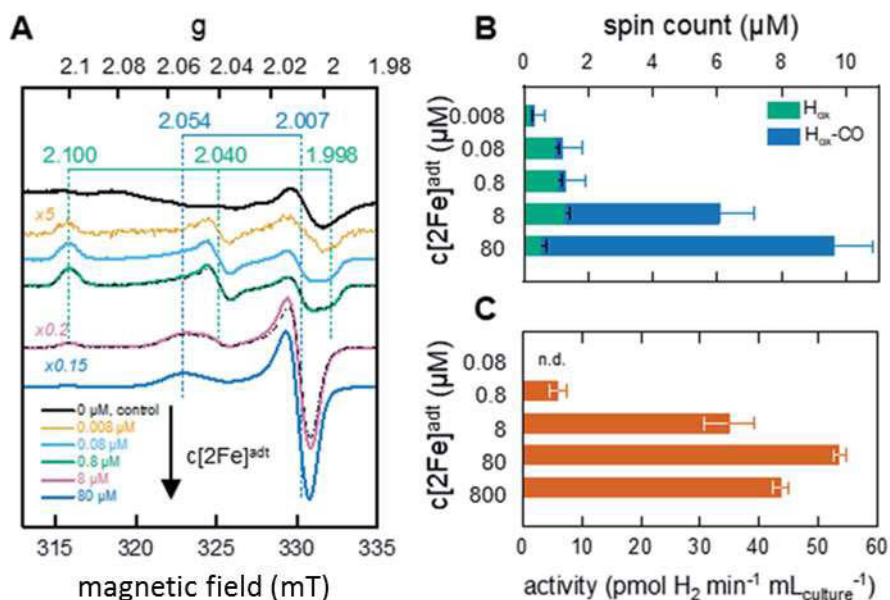


**Fig. 2.1** Whole-cell H-cluster assembly followed via EPR spectroscopy and  $\text{H}_2$  gas production. **(A)** EPR spectra of *E. coli* cells' suspensions incubated with different amounts of  $[2\text{Fe}]^{\text{adt}}$ . H-cluster signal increases upon as the concentration of the synthetic cofactor increases and appears as a mixture of  $\text{H}_{\text{ox}}$  and  $\text{H}_{\text{ox}}\text{-CO}$  states. The g-values reported for  $\text{H}_{\text{ox}}$  (green dashed lines) and  $\text{H}_{\text{ox}}\text{-CO}$  (blue dashed lines) are extrapolated from the simulations of the 0.8 and 8  $\mu\text{M}$  samples (black dash-dotted lines). The *apo-CrHydA1* (black spectrum) was subtracted from all other spectra to remove signals coming from the cell background. EPR experimental conditions:  $T = 20 \text{ K}$ ,  $P = 1 \text{ mW}$ , Frequency = 9.28 GHz. **(B)** Spin count for the  $\text{H}_{\text{ox}}$  (green bars) and  $\text{H}_{\text{ox}}\text{-CO}$  (blue bars) signals in each sample, derived from simulations. Error bars account for both relative error from simulations and for additional absolute error coming from the background subtraction. **(C)**  $\text{H}_2$  evolving activity measured from anaerobic *E. coli* suspensions over the first hour after addition of the cofactor. Values are given as pmol of hydrogen per minute per milliliter of culture used to prepare the sample. Reprinted with permission from ref.<sup>134</sup>

## 2.3. Integrity check.

The follow-up question came up naturally: are we really observing the H-cluster from inside the cells? Or in other words: are the cells intact? We employed a wide array of methods to answer this question. At first, we simply separated cells and supernatant via centrifugation and checked the protein content of both fractions with SDS-PAGE, verifying the absence of the 49kDa band corresponding to *CrHydA1* in the supernatant. We also measured *in vitro* H<sub>2</sub>-evolution activity in both fractions; the absence of activity in the supernatant was a solid confirmation that all of our matured enzyme still resided inside of *E.coli*.

The perhaps more spectacular confirmation of this came from the images obtained by combining Atomic Force Microscopy (AFM) and scattering Scanning Nearfield Optical Microscopy (sSNOM) (Fig.2.2A).

These microscopy techniques were performed on a film obtained by drying the cell suspension on a template-stripped gold. From the AFM images it was clearly visible that the majority of the cells were morphologically intact, with no signs of damage to the membrane. Furthermore, sSNOM was used to monitor the optical properties of the film in the infrared region and the Nano-FTIR near-field phase spectra showed a concentration of the typical protein absorption bands (Amide I, 1600-1700 cm<sup>-1</sup>, and Amide II, ~1550 cm<sup>-1</sup>) in correspondence to the cell profile (Fig 2.2B).

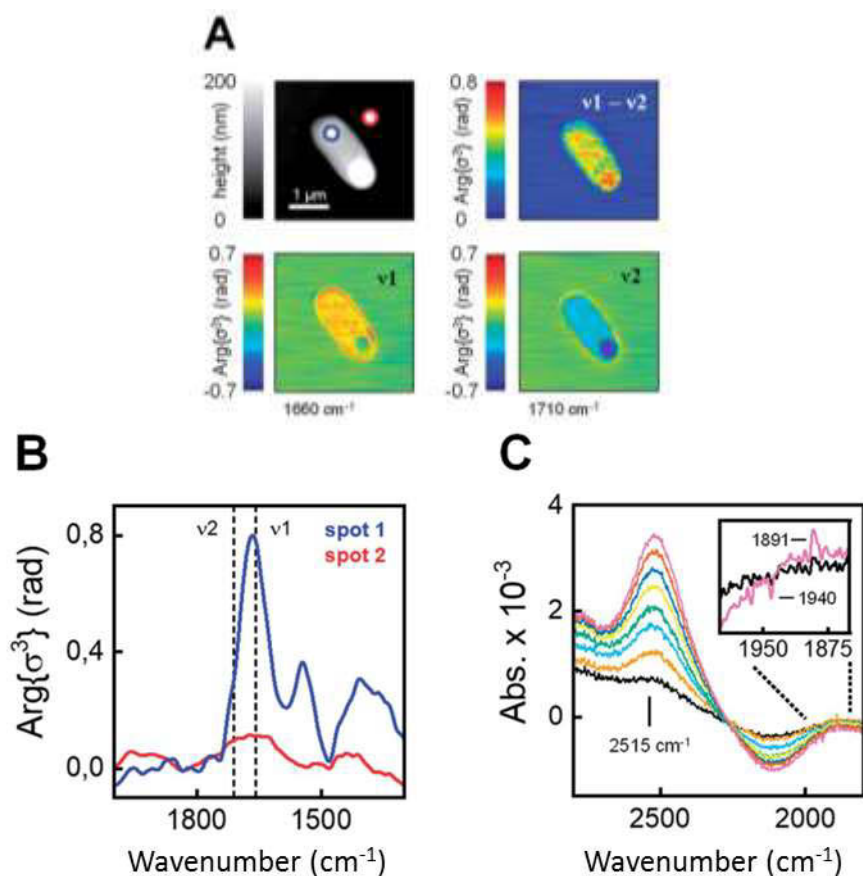


**Fig. 2.2** Single cell microscopy and spectroscopy. **(A) Upper left:** AFM topography of an [2Fe]<sup>adt</sup>-HydA1-containing *E. coli* cell. **Lower left:** sSNOM image mapped at the amide I absorption frequency ( $\nu_1 = 1660 \text{ cm}^{-1}$ ). **Lower right:** sSNOM image mapped at the frequency corresponding to the topography artifact ( $\nu_2 = 1710 \text{ cm}^{-1}$ ). **Upper right:** sSNOM image obtained by difference ( $\nu_1 - \nu_2$ ), clearly showing that the protein is fully localized inside the cell. **(B)** Nano-FTIR near-field phase spectrum in the  $2000\text{--}1300 \text{ cm}^{-1}$  range. Spectra were recorded on a spot inside the cell (spot 1, blue) and on one next to the cell (spot 2, red), as shown in the AFM topography picture (panel A, upper left). **(C)** ATR FTIR difference spectra showing the increase of the HDO band ( $2515 \text{ cm}^{-1}$ ) upon exposure to D<sub>2</sub> (exposure time 0–90 s going from black to purple). **Inset:** difference spectra showing the simultaneous enrichment of H<sub>red</sub>H<sup>+</sup> (reporter band  $1891 \text{ cm}^{-1}$ ) over H<sub>ox</sub> (reporter band  $1940 \text{ cm}^{-1}$ ). Reprinted with permission from ref.<sup>134</sup>

## 2.4. Probing the catalytic cycle with whole-cell ATR-FTIR spectroscopy.

After confirming the intracellular residency of CrHydA1 and the formation of a functional H-cluster, we could start investigating how the catalytic cycle would appear under these conditions.

ATR-FTIR was chosen as principal spectroscopic technique as EPR, despite being more sensitive, would be blind to any diamagnetic intermediate and would only return a partial picture of the catalytic cycle.

A semi-dry film was formed by depositing the  $[2\text{Fe}]^{\text{adt}}$ -CrHydA1-containing

*E.coli* cell suspension on an ATR silicon crystal, drying under a flow of inert gas ( $\text{N}_2$  or Ar) and re-hydrating it with an aerosol obtained by bubbling the same gas in water or buffer. When the inert gas was switched to 100 mbar of deuterium gas ( $\text{D}_2$ ), the FTIR spectrum of the film showed the appearance of an HDO band (Fig. 2.2C). This observation signifies that deuterium ions were being released in the film water as a consequence of the  $\text{D}_2$ -cleavage activity of CrHydA1, confirming that the enzyme retains its ability to perform heterolytic cleavage even in these semi-dry film conditions.

The  $2050\text{--}1750\text{ cm}^{-1}$  region contains the stretching bands of the metal-coordinating CO molecules belonging to the H-cluster. For  $[2\text{Fe}]^{\text{adt}}$ -CrHydA1-containing film this region was clearly resolved using ATR-FTIR and, under 100% inert gas, showed an enzyme predominantly residing in  $\text{H}_{\text{ox}}$ , with only minor traces of  $\text{H}_{\text{ox}}\text{-CO}$ . No trace of free  $[2\text{Fe}]^{\text{adt}}$  complex was detected.

Exposing the film to 1%  $\text{H}_2$  lead to the enrichment of the  $\text{H}_{\text{red}}\text{H}^+$  state on a timescale of seconds, and as the gas was switched back to 100%  $\text{N}_2$  we observed full reversion to  $\text{H}_{\text{ox}}$  (Fig. 2.3A, spectra a and b). Increasing the  $\text{H}_2$  concentration to 100% had no effect on the redox states composition of the spectrum, as compared to 1%  $\text{H}_2$ . This is striking as on films made with purified  $[2\text{Fe}]^{\text{adt}}$ -CrHydA,  $\text{H}_{\text{red}}$  and  $\text{H}_{\text{sred}}\text{H}^+$  bands are usually formed and accumulated under pure hydrogen atmosphere (Fig 2.3D). The possibility that this difference could depend on a limited accessibility of  $[2\text{Fe}]^{\text{adt}}$ -CrHydA1 to gas treatments, due to the cellular envelope, was excluded when full conversion to  $\text{H}_{\text{ox}}\text{-CO}$  was observed upon exposure to 1% CO (Fig. 2.3A, spectrum c). The accumulation of  $\text{H}_{\text{red}}$ , in particular, was also hindered by diluting the enzyme with Bovine Serum Albumin (BSA) (Fig. 2.3C), which suggests that its formation might depend on intermolecular collisions between enzyme molecules, which are impeded by the presence of BSA or by the cytoplasmic crowding.<sup>98</sup>

At lower pH (buffer pH4, 2mM NaDT) and under inert gas flow,  $\text{H}_{\text{ox}}$  converted quantitatively to  $\text{H}_{\text{ox}}\text{H}^+$ , a slightly blue-shifted  $\text{H}_{\text{ox}}$ -like state thought to be protonated on the  $[\text{4Fe4S}]_{\text{H}}$  cluster (Figure 2.3A, spectrum d).<sup>98</sup>

Using 1%  $\text{H}_2$  instead of the inert gas allowed for the accumulation of the terminal hydride-bound state  $\text{H}_{\text{hyd}}$  (Figure 2.3B).

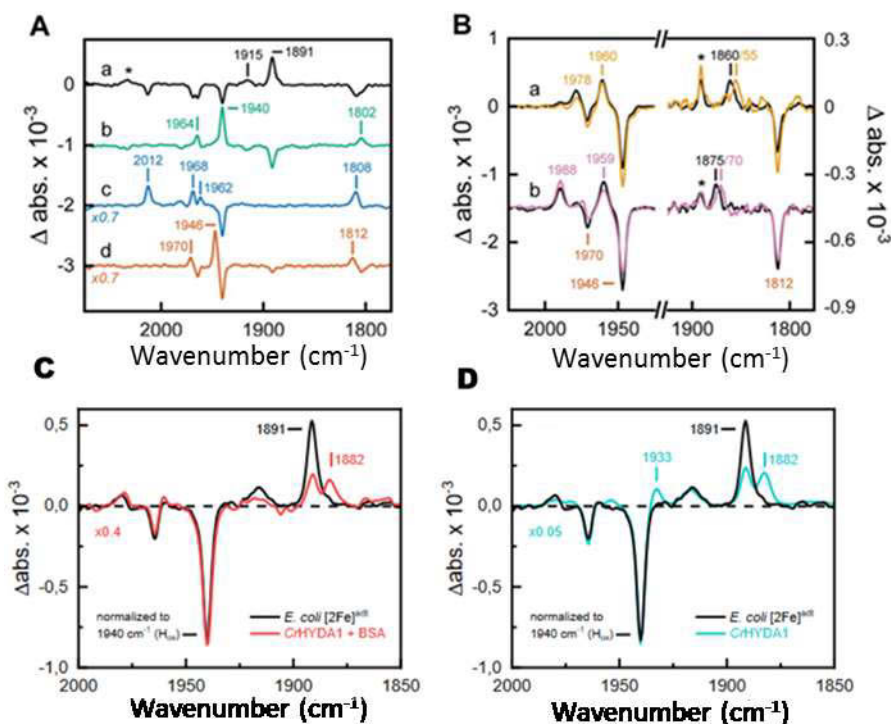


**Fig. 2.3 Panels A and B:** Difference ATR-FTIR spectra of [2Fe]<sup>adt</sup>-CrHydA1 containing *E. coli* cells. **(A):** Upon exposure to 1% H<sub>2</sub> (bubbled in buffer pH 8, 2 mM NaDT) a mixture of H<sub>ox</sub> and H<sub>ox</sub>-CO readily converted to H<sub>red</sub> (**spectrum a**). The asterisk (\*) marks a 2032 cm<sup>-1</sup> signal attributed to a CN<sup>-</sup> band of H<sub>red</sub>H<sup>+</sup>. In the absence of H<sub>2</sub> a complete reversion to H<sub>ox</sub> was observed (**spectrum b**). Exposure to 1% CO was enough to generate a full H<sub>ox</sub>-CO population (**spectrum c**). Non reducing acidic conditions (N<sub>2</sub> bubbled in buffer pH 4, 2 mM NaDT) trigger the conversion of H<sub>ox</sub> into H<sub>ox</sub>H<sup>+</sup> (**spectrum d**). **(B):** In the presence of 1% H<sub>2</sub> and acidic conditions (pH 4, 2 mM NaDT) the formation of H<sub>hyd</sub> from H<sub>ox</sub>H was observed (**spectrum a**, **black line**). Using D<sub>2</sub> gas instead of H<sub>2</sub> caused the typical redshift of the bridging-CO band from 1860 to 1855 cm<sup>-1</sup>, confirming the presence of a hydride ligand (**spectrum a**, **dark yellow line**). Increasing the NaDT concentration in the aerosol buffer to 100 mM resulted in the accumulation of a different hydride state: H<sub>hyd</sub>H<sup>+</sup> (**spectrum b**, **black line**). Again, the redshift of the bridging-CO band under D<sub>2</sub> (from 1875 to 1870 cm<sup>-1</sup>) was diriment for assigning this signal to a hydride species (**spectrum b**, **purple line**). The asterisk (\*) marks a band attributed to a small fraction of H<sub>red</sub>H<sup>+</sup>. **Panels C and D:** Reactivity differences between whole-cell samples and purified [2Fe]<sup>adt</sup>-CrHydA1 monitored by ATR-FTIR spectroscopy. **(C)** A mixture of purified [2Fe]<sup>adt</sup>-CrHydA1 and BSA (Bovine Serum Albumine) was exposed to 100% H<sub>2</sub>. This resulted in the formation of a mixture of H<sub>red</sub>H<sup>+</sup> (reporter band = 1891 cm<sup>-1</sup>) and H<sub>sred</sub>H<sup>+</sup> (reporter band = 1882 cm<sup>-1</sup>) (**red spectrum**). Conversely, the same conditions applied to the whole-cell sample (**black spectrum**) only caused the enrichment of H<sub>red</sub>H<sup>+</sup>. **(D)** When CrHydA1 was placed on the ATR crystal without BSA addition the presence of H<sub>red</sub> could be detected (blue spectrum, reported band 1933 cm<sup>-1</sup>), a state that does not seem to accumulate with *E. coli* cells containing [2Fe]<sup>adt</sup>-HydA1. Reprinted with permission from ref.<sup>134</sup>

Surprisingly, more reducing conditions, achieved by increasing NaDT concentration to 100mM resulted in the accumulation of a different hydride-like state displaying a blueshift of a magnitude suggestive of a protonation event involving the  $[2\text{Fe}]_{\text{H}}$  subsite.<sup>76</sup> Supporting the protonation hypothesis there is the observation that strong reducing conditions (1%  $\text{H}_2$ , 100mM NaDT) combined with an alkaline buffer (pH 8) lead to the accumulation of the “unprotonated”  $\text{H}_{\text{hyd}}$  state.

For both  $\text{H}_{\text{hyd}}$  and this new hydride-like state, swapping  $\text{H}_2$  gas for  $\text{D}_2$  caused the typical hydride-specific shift of the bridging-CO FTIR band, proving the presence of terminally bound hydride ligands (Figure 2.3B).

## 2.5. Confirming the occurrence of two distinct hydride states with EPR.

To confirm that we were dealing with two distinct redox states of the H-cluster, we turned to EPR as a complementary spectroscopic technique.

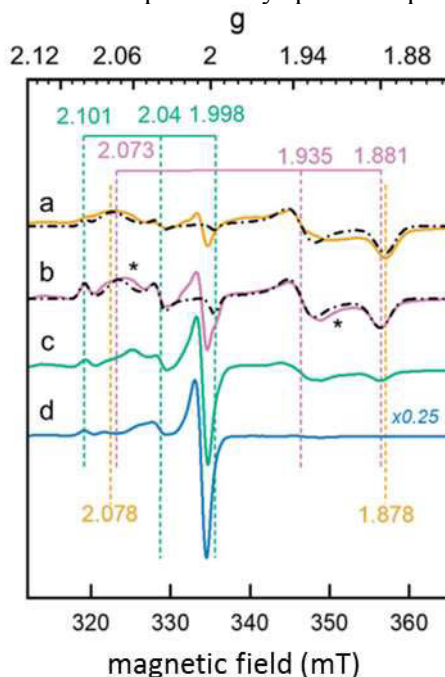


**Fig. 2.4** EPR spectra of whole-cell generated hydride states. **(a)** Sample of  $[2\text{Fe}]^{\text{adt}}\text{-CrHydA1}$  containing cells prepared in pH 7.5 buffer containing 10mM NaDT, flushed for 15 min with  $\text{H}_2$  and flash frozen, displaying the  $\text{H}_{\text{hyd}}$  state (dark yellow spectrum); **(b)**: Sample prepared as in (a) but in a pH 4 buffer, displaying a different signal attributed to  $\text{H}_{\text{hyd}}\text{H}^+$  (purple spectrum); **(c)** Sample prepared as in (b) but with no NaDT, giving rise to a less intense  $\text{H}_{\text{hyd}}\text{H}^+$  signal (green spectrum); **(d)** Sample prepared as in (b) but without  $\text{H}_2$  flushing, showing no  $\text{H}_{\text{hyd}}\text{H}^+$  signal (blue spectrum). Simulations are overlaid to spectra as black dashed-dotted lines.  $g$ -values are given for  $\text{H}_{\text{ox}}/\text{H}_{\text{ox}}\text{H}$  (green),  $\text{H}_{\text{hyd}}$  (dark yellow) and  $\text{H}_{\text{hyd}}\text{H}^+$  (purple) Asterisks (\*) indicate weak signals possibly arising from an  $\text{H}_{\text{trans}}$ -like state.<sup>76</sup> EPR experimental conditions:  $T = 20\text{ K}$ ,  $P = 1\text{ mW}$ , Frequency = 9.38 GHz. Reprinted with permission from ref.<sup>134</sup>

Samples were then prepared trying to mimic the conditions applied in FTIR experiments. Strong reducing conditions (10mM NaDT, 100%  $\text{H}_2$  flushing) in a slightly alkaline buffer (pH 7.5) cause the build up of a broad and fast relaxing rhombic signal ( $g_{\text{zyx}} = 2.078; 1.935; 1.881$ ) corresponding to the  $\text{H}_{\text{hyd}}$  signal reported for the purified enzyme (Figure 2.4, spectrum a).<sup>74</sup> When switching to an acidic buffer (pH 4) a slightly less anisotropic rhombic signal ( $g_{\text{zyx}} = 2.073; 1.935; 1.881$ ) is accumulated (Figure 2.4, spectrum b). NaDT does not seem to be necessary to generate this new state as it accumulates also



in its absence, although to a lesser extent (Figure 2.4, spectrum c), whereas in the absence of  $H_2$  we could not detect any trace of it. As this second signal shows the hallmarks of a  $[4Fe4S]_H$  paramagnetic species, being relatively broad and fast-relaxing, we were confident in assigning it to  $H_{hyd}H^+$ , confirming the occurrence of this state under whole-cell conditions.

## 2.6. Conclusions.

Artificial maturation proved, once again, to be a reliable method to obtain relevant amounts of mature  $[FeFe]$  hydrogenases in a form that is active and indistinguishable from the native enzyme.

Interestingly, a whole-cell matured  $[2Fe]^{adt}$ -CrHydA is able to turn over and produce hydrogen in the absence of external reducing agents and redox mediators, implying that it is somehow able to interface with *E. coli* proteome (e.g. with its ferredoxins). A further confirmation of its ability to turnover comes from the  $H_2$ -dependent accumulation of the  $H_{red}H^+$  state and from the auto-oxidation back to  $H_{ox}$  as the  $H_2$  pressure is removed, both observed in FTIR.

These two apparently trivial observations signify that the enzyme is going through the catalytic cycle and that the equilibrium of the different redox intermediates can be manipulated varying the outside conditions, both pivotal for a whole-cell catalytic cycle probing.

The subsequent experiments revealed a complex hydride chemistry as FTIR and EPR complemented each other and allowed us to identify two different hydride states. Lowering the pH of the cell suspension, under inert gas flow, led to the accumulation of the protonated  $H_{ox}H$  state, which quantitatively converted into the terminally-bound hydride state  $H_{hyd}$  in the presence of 1%  $H_2$  and low amounts of the chemical reductant NaDT. Increasing the amount of NaDT caused the appearance of a protonated hydride-state,  $H_{hyd}H^+$ . Its protonated state was confirmed by the observation that the same conditions in an alkaline buffer only led to the accumulation of  $H_{hyd}$ , whereas its hydride-state nature was confirmed via H/D substitution and by observing an EPR signature suggestive of an electronic structure similar to  $H_{hyd}$ .

A recent study has problematized the use of NaDT as a reductant in mechanistic studies of  $[FeFe]$  hydrogenases, putting the spotlight on the interaction between the H-cluster and the product of NaDT oxidation,  $SO_2$ .<sup>135</sup> The fact that we are able to detect the  $H_{hyd}H^+$  state with EPR even in the absence of NaDT seems to exclude that what we are observing could be an artifact originating from this non-physiological reductant.

Interestingly, two intermediates commonly observed in purified enzymes,  $H_{red}$  and  $H_{sred}H^+$ , were not detected under any of the conditions applied in this study. ATR-FTIR experiments performed on purified  $[2Fe]^{adt}$ -CrHydA, on its own or mixed with BSA, suggest that in the case of  $H_{red}$  this difference could

be due to the effect of cell crowding. In the case of  $H_{sred}H^+$  no specific explanation can be given, but it is possible that the lower intracellular pH as compared to the pH of the buffer used for the BSA-dilution experiment ( intracellular =  $7.5 \pm 0.3$ , buffer = 8) could play a role.

It is important to point out that the spectroscopic detection of specific intermediates in a functional enzyme and under whole-cell conditions is supporting their physiological relevance; therefore the results of our investigation hint at a catalytic cycle that can be schematized like in Fig.2.5.

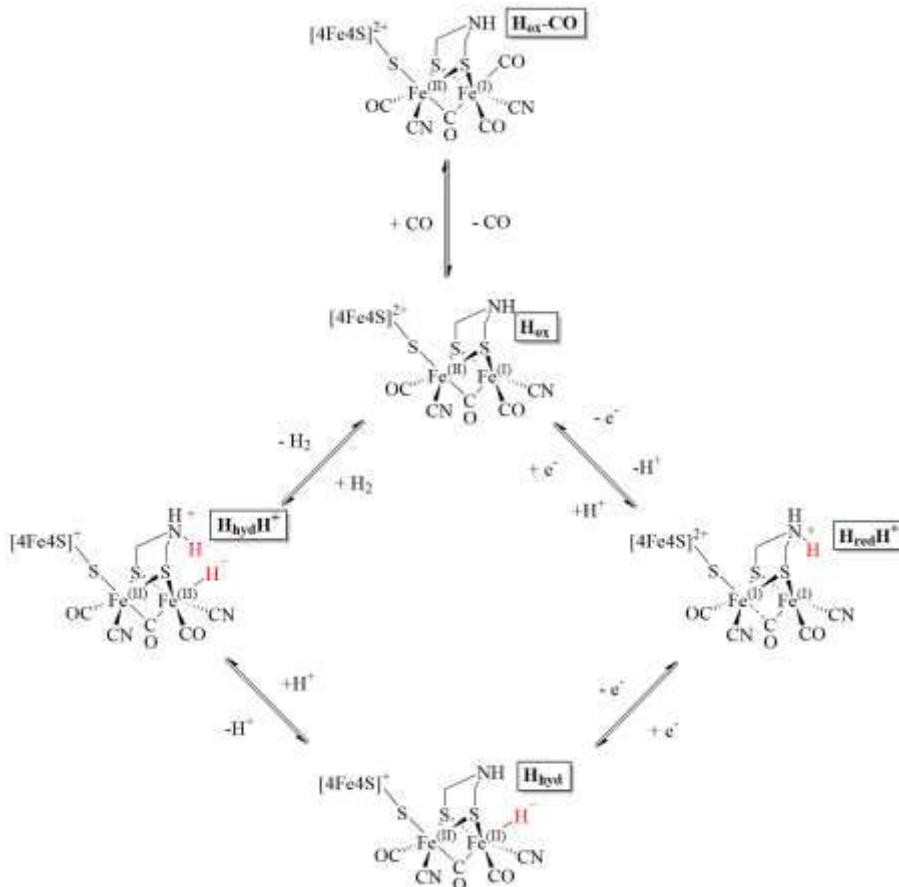


**Fig. 2.5** Schematic representation of the proposed catalytic cycle of [FeFe] hydrogenases. The scheme is based on the states observed under whole-cell conditions, therefore including  $H_{hyd}H^+$  and lacking  $H_{red}$  and  $H_{sred}H^+$ .

In conclusion, the results of this study show how the application of the artificial maturation to a whole-cell system represents a promising approach when it comes to characterizing catalytic intermediates and supporting their physiological relevance. Furthermore, in the context of mechanistic understanding,

we isolated the  $\text{H}_{\text{hyd}}\text{H}^+$  state under whole cell conditions, after its first identification in vitro,<sup>76</sup> corroborating the hypothesis of its relevance for the catalytic cycle. The determination of its FTIR fingerprint will possibly pave the way to future studies on its reactivity using transient spectroscopy, which might help shedding light on the complex hydride chemistry of these systems and providing critical insight into the mechanism of  $\text{H}_2$  evolution and cleavage.

## Chapter 3 - Paper II:

# Stability of the H-cluster under whole-cell conditions – Formation of an H<sub>trans</sub>-like state and its reactivity towards oxygen

### 3.1. Introduction and motivation

In the previous paper we have verified our ability to assemble and probe the H-cluster inside a bacterial cell. We have also verified that the intracellular environment has a non-negligible influence on [FeFe] hydrogenases, in particular concerning accessibility and relative stability of various intermediates in the catalytic cycle.

As we have seen in section 1.3, when it comes to transition metal catalysts or metalloenzymes, the incorporation into a bacterial cell can be seen a double-edged sword: on the one hand, it provides some degree of compartmentalization for the reaction, and protection from detrimental external agents (e.g. molecular oxygen); on the other hand it represents a not-well-defined chemical environment and it exposes the catalyst or enzyme to a series of possible inhibitors and competitors.

In the case of [FeFe] hydrogenases sulfide species have been shown to bind to the H-cluster and to generate the inhibited and oxygen-tolerant states H<sub>trans</sub> and H<sub>inact</sub>.<sup>79, 80</sup> This is a matter of interest, as *E. coli* is known to involve sulfide and other reactive sulfur species in several biosynthetic and oxidative stress response pathways.<sup>136, 137</sup>

In this study, we investigated the long term impact of whole-cell conditions on two model [FeFe] hydrogenases, evidencing the formation of an inhibited H<sub>trans</sub>-like state. Then, we estimated the extent of oxygen protection granted to the enzyme by the cell envelope and by this newly found state. Finally, we explored the role played by the proton transfer chain in the formation of this inhibited species.

## 3.2. Stability of [FeFe] hydrogenases under whole-cell conditions

Following the procedure developed in Paper I, we matured *CrHydA1*-expressing *E. coli* cells, in form of a suspension in M9 minimal medium, with an amount of  $[2\text{Fe}]^{\text{adt}}$  complex sufficient to yield quantitative H-cluster assembly. However, the incubation was prolonged beyond the first hour and, over its course, hydrogen production was measured. We noticed that hydrogen production would unavoidably halt after 3-4 hours from the  $[2\text{Fe}]^{\text{adt}}$  addition. Thus, EPR samples were prepared at different time points in order to monitor the state of the H-cluster over time (Fig 4.1A).

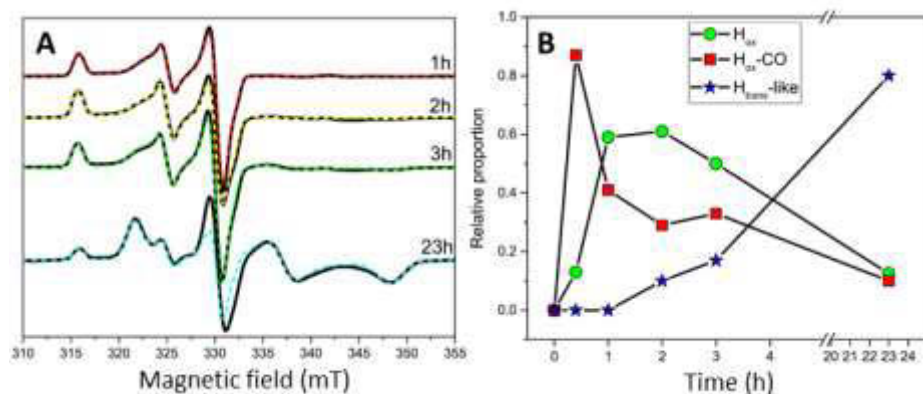


**Fig. 3.1** Effect of time on  $[2\text{Fe}]^{\text{adt}}$ -*CrHydA1* in *E. coli* cells. **(A)** EPR spectra of whole-cell  $[2\text{Fe}]^{\text{adt}}$ -*CrHydA1* at different time points following complex addition. Spectra (black lines) are overlaid with their respective simulations (colored dashed lines). **(B)** Relative abundance of the different states identified for samples from the dataset shown in panel A. Relative weights are extrapolated from simulations. EPR experimental conditions: temperature = 20K, power = 1mW, frequency = 9.28 GHz. Reprinted with permission from ref.<sup>138</sup>

The first time points showed the expected mixture of  $H_{ox}$  and  $H_{ox}-CO$  states, with the latter gradually converting into the former following CO release (Fig 3.1B). Simulations though revealed the presence of a third redox state in the mixture, characterized by a broad rhombic EPR signal with  $g_{zyx} = 2.064, 1.972, 1.910$ . This signal begins to accumulate already after 2h from  $[2\text{Fe}]^{\text{adt}}$  addition and becomes predominant in less than 24h. The signal appears H-cluster specific, as it cannot be observed in samples not expressing apo-*CrHydA1* or not matured using  $[2\text{Fe}]^{\text{adt}}$ , and is reminiscent of the sulfide-inhibited  $H_{trans}$  state identified in *Desulfovibrio desulfuricans* dimeric [FeFe] hydrogenase (*DdHydAB*).<sup>77, 139</sup>

The assignment of this  $H_{trans}$ -like state as a sulfide-inhibited species was reinforced by exposing the matured whole-cell samples to exogenous sources

of sulfide, namely L-cysteine or Na<sub>2</sub>S (Fig 3.2A). Both treatments resulted in samples displaying a more marked H<sub>trans</sub>-like signal compared to control, suggesting that this species could indeed be forming following sulfide-binding.

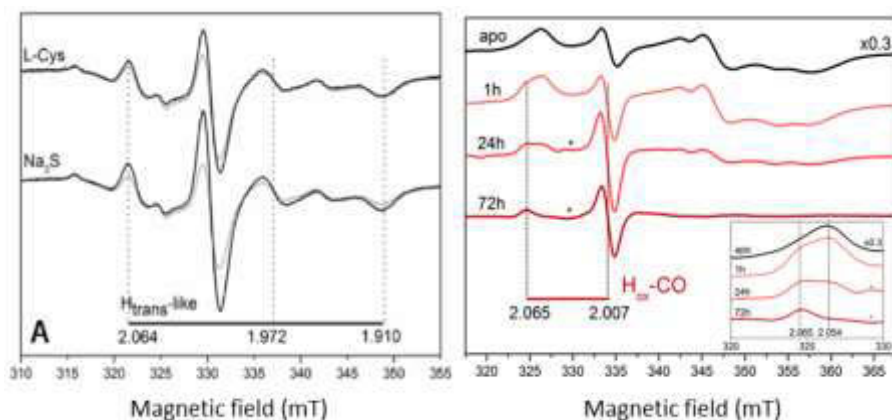


**Fig. 3.2 (A)** EPR spectra of whole-cell [2Fe]<sup>adt</sup>-CrHydA1 showing the effect of sulfide sources on the accumulation of a H<sub>trans</sub>-like state following a 23h incubation. A control spectrum (no sulfide source, grey lines) is overlaid to the spectra of samples incubated in the presence of L-cysteine (L-Cys) or Na<sub>2</sub>S (black lines). **(B)** Effect of time on [2Fe]<sup>adt</sup>-DdHydAB in *E. coli* cells. EPR spectra are presented for the 1h, 24h and 72h timepoints, following [2Fe]<sup>adt</sup> addition. The spectrum of the unmaturation samples (apo) is given as a reference for the [4Fe4S] clusters' interaction spectrum. Inset shows a detail of the 320-330mT region, evidencing the features of H<sub>ox</sub>-CO ( $g_{||} = 2.065$ ) and of the [4Fe4S] clusters' interaction spectrum ( $g_z = 2.054$ ). EPR experimental conditions: temperature = 20K, power = 1mW, frequency = 9.28 GHz. Reprinted with permission from ref.<sup>138</sup>

As both H<sub>trans</sub> and H<sub>inact</sub> have been almost exclusively characterized in DdHydAB, it was natural to try and observe how their formation would be influenced by the whole-cell conditions in this alternative model hydrogenase. We then proceeded to express DdHydAB in our *E. coli* strain and to artificially mature it with [2Fe]<sup>adt</sup>.

*In vitro* DdHydAB maturation is peculiar as it takes more than 2 days of incubation with the synthetic complex to obtain a quantitative incorporation into the active site, whereas for CrHydA1 the same result can be obtained in minutes. Surprisingly though, a distinct H<sub>ox</sub>-CO signal is observable in whole-cell EPR samples of [2Fe]<sup>adt</sup>-DdHydAB already after 1h from [2Fe]<sup>adt</sup> addition (Fig. 3.2B). The only spectral change over the course of the long term incubation was the gradual disappearance of the signal contributions coming from reduced [4Fe4S]<sub>H</sub> and accessory [4Fe4S] clusters (F-clusters), and no H<sub>trans</sub>-like signal was detected even after 72h. Tentatively, we attributed this phenomenon (or lack thereof) to the known strong affinity of [2Fe]<sup>adt</sup>-DdHydAB for CO, which could prevent other inhibitors from binding to the H-cluster.<sup>85</sup>

### 3.3. Oxygen tolerance

As mentioned in the introduction to this chapter (section 3.1), both  $H_{trans}$  and  $H_{inact}$  have been isolated and characterized as oxygen-tolerant states, with the sulfide ligand protecting the H-cluster from the attack of  $O_2$ . Thus, we decided to test how much the formation of the  $H_{trans}$ -like state could influence the oxygen tolerance of whole-cell  $[2Fe]^{adt}$ -CrHydA1 samples.

For this purpose, we exposed samples to air for 1h, which had been pre-incubated for 1h or 23h following  $[2Fe]^{adt}$  addition and therefore respectively consisted into a balanced mixture of  $H_{ox}$  and  $H_{ox-CO}$  states (1h pre-incubated) and into an 80%  $H_{trans}$  state (23h pre-incubated).

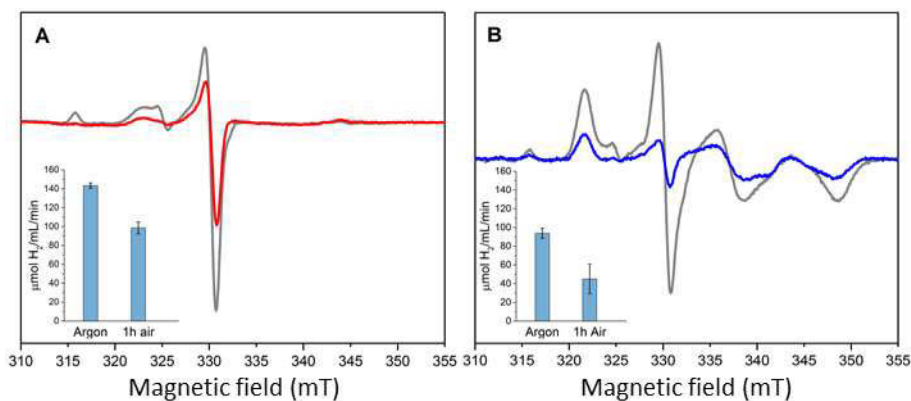


**Fig. 3.3** EPR spectra and  $H_2$ -evolution activity measurements showing the effect of air exposure on whole-cell  $[2Fe]^{adt}$ -CrHydA1 samples. **(A)** The EPR spectrum of a 1h-incubated sample, kept anaerobic, (grey spectrum) is overlaid to an identical sample exposed to air for 1h (red spectrum) Inset:  $H_2$ -evolution activities measured on the same samples. **(B)** The EPR spectrum of a 23h-incubated sample, kept anaerobic, (grey spectrum) is overlaid to an identical sample exposed to air for 1h (red spectrum) Inset:  $H_2$ -evolution activities measured on the same samples. Activity values are the mean values obtained from two biological replicates, with standard deviation reported as error bars. EPR experimental parameters: temperature = 20K, power = 1mW, frequency = 9.28 GHz. Reprinted with permission from ref.<sup>138</sup>

We followed the effect of air exposure by comparing the intensity of EPR signals and the specific activity of the samples (Fig. 3.3). On the 1h pre-incubated samples, air exposure resulted in ~ 55% of the EPR signal being lost, with all of the residual signal being attributable to  $H_{ox-CO}$ . This was not surprising, as CO-binding is known to grant some degree of oxygen resistance and as H-cluster degradation leads to its accumulation through a mechanism known in the field as “cannibalization”.<sup>78, 139</sup> In the case of the 23h pre-incubated samples, air exposure led to a ~ 65% loss of signal, with both  $H_{trans}$ -like and residual  $H_{ox}$  decreasing in terms of signal amplitude.

Yet, in both cases, the loss of EPR signal was larger than the loss of activity; 1h and 23h pre-incubated samples respectively lost only  $\sim 30\%$  and  $\sim 50\%$  of their  $H_2$ -evolution activity. This discrepancy is easily explained: the loss of EPR signal can be attributed to either H-cluster degradation or to the formation of EPR-silent species such as  $H_{inact}$ , with the latter species being able to re-enter the catalytic cycle under the strongly reductive conditions employed in activity assays.<sup>79, 139</sup>

Interestingly, these results show that the accumulation of the  $H_{trans}$ -like state prior to air exposure does not grant increased oxygen tolerance, as the 23h pre-incubated samples showed even greater activity losses compared to the 1h pre-incubated ones. On the other hand, considering that isolated *CrHydA1* is usually completely inactivated by oxygen on a timescale of minutes,<sup>43, 85</sup> our whole-cell samples displayed a remarkable tolerance. This is attributable to the low intracellular  $O_2$  concentrations ensured by cellular respiration, a process which is indeed expected to be more efficient in “young” and metabolically active cells.<sup>140</sup>

### 3.4. Role of the Proton Transfer Chain in the formation of the $H_{trans}$ -like state

The proposed mechanism for the formation of the  $H_{trans}$  and  $H_{inact}$  states includes the binding of an  $H_2S$  ligand onto the open coordination site of the H-cluster and its deprotonation to  $HS^-$ , involving the enzyme’s proton transfer chain.<sup>79</sup>

Given its similarities with the canonical  $H_{trans}$  and  $H_{inact}$  states, we decided to investigate the role of the proton transfer chain in the formation of the  $H_{trans}$ -like and  $H_{inact}$ -like states. Our strategy revolved around two modifications to the active site of *CrHydA1*, both aiming at disrupting the proton transfer chain functionality.

The first modification target was the pending amine on the adt bridgehead, which acts as final proton relay in the proton transfer chain. We then matured a whole-cell *CrHydA1* sample replacing the  $[2Fe]^{adt}$  mimic with  $[2Fe]^{pdt}$  ( $Fe_2(pdt)(CO)_4(CN)_2^{2-}$ , pdt = propanedithiolate,  $^-SCH_2CH_2CH_2S^-$ ), a variant where the bridgehead amine has been replaced with a non-protonatable aliphatic group.  $[2Fe]^{pdt}$  enzyme variants are reported to be inactive and locked into a state analogous to  $H_{ox}$ .<sup>28, 112, 130</sup> Consistently with previous reports, samples matured with  $[2Fe]^{pdt}$  displayed a pure  $H_{ox}$ -like EPR signal, with no trace of  $H_{trans}$ -like signals emerging even after a 23h incubation.

This result was in agreement with the proposed model for  $H_{trans}$  formation, which involves a proton transfer step from  $H_2S$  to the bridging amine.<sup>79</sup>



Moving toward the enzyme exterior, the second modification target was Cysteine169 (C169). This strictly conserved residue is the first protein-derived component of the proton transfer chain.<sup>39</sup> Mutating this amino acid into a serine (C169S) or an alanine (C169A) results into a completely blocked or severely impaired proton transfer chain and into inactive enzyme variants. In particular, the C169S variant has been used in the past to isolate hydride intermediates of the catalytic cycle.<sup>74, 141</sup>

We then chose to generate the C169S mutant (*CrHydA1*<sup>C169S</sup>), to mature it under whole-cell conditions using the  $[2\text{Fe}]^{\text{adt}}$  complex, and to monitor it using EPR (Fig. 3.4A).

Surprisingly, these samples accumulated a broad rhombic EPR signal ( $g_{\text{zyx}} = 2.064, 1.970, 1.910$ ) almost identical to the  $\text{H}_{\text{trans}}$ -like state detected in the wild-type ( $g_{\text{zyx}} = 2.064, 1.972, 1.910$ ). A similar signal had already been reported for the C169S variant *in vitro*, and had been assigned to an hydride-bound  $\text{H}_{\text{trans}}$ -like species.<sup>74, 76</sup>

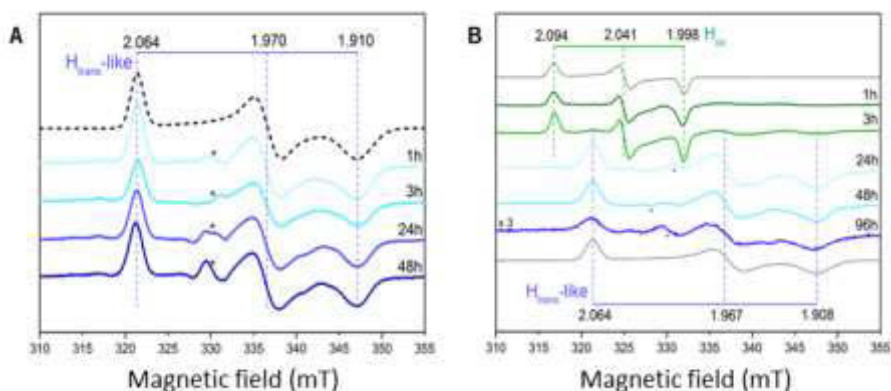


**Fig. 3.4** Effect of time on whole-cell *CrHydA1*<sup>C169S</sup> samples **(A)** EPR spectra are shown for the 1h, 3h, 24h and 48h timepoints, following  $[2\text{Fe}]^{\text{adt}}$  addition. For the  $\text{H}_{\text{trans}}$ -like state identified in this variant, g-values are given on a blue horizontal bar. **(B)** EPR spectra are shown for the 1h, 3h, 24h, 48 and 72h time points, following  $[2\text{Fe}]^{\text{pdt}}$  addition. For the  $\text{H}_{\text{ox}}$  and the  $\text{H}_{\text{trans}}$ -like state identified in this variant g-values are given on a green and on a blue horizontal bar, respectively. In both panels, asterisks (\*) mark non-specific features derived from an imperfect background subtraction. EPR experimental conditions: temperature = 20K, power = 1mW, frequency = 9.28 GHz. Reprinted with permission from ref.<sup>138</sup>

The accumulation of a metal-hydride species seemed very unlikely under our experimental conditions. Moreover, we were able to isolate the C169S variant in the  $\text{H}_{\text{trans}}$ -like state via affinity chromatography purification only using buffers supplemented with 100mM  $\text{Na}_2\text{S}$ , an indication that a sulfide ligand could be involved. In the absence of additional sulfide and under whole-cell conditions, incubation up to 48 h seem to have no effect on the shape or on the intensity of the signal, and no other species were detectable with EPR. The

same experiment performed at low temperature (12°C instead of 37°C), where we can expect that the chemistry involved is slowed down, revealed that also in the C169S variant the first species to form is  $H_{ox}$  which then begins to convert into a  $H_{trans}$ -like state after 2 h.

The diverging effects observed in the two variants suggest a more complex picture than the “simple” effect of an impaired proton transfer chain. We therefore decided to investigate the effect of the combination of the two modification by maturing the C169S mutant with the  $[2Fe]^{pdt}$  complex, generating  $[2Fe]^{pdt}$ -C169S (Fig 3.4B). EPR spectra taken at different timepoints show the initial formation of an almost pure  $[2Fe]^{pdt}$ - $H_{ox}$  state, indeed consistent with the behavior expected from an enzyme matured with  $[2Fe]^{pdt}$ . After 3h of incubation though, we began detecting an  $H_{trans}$ -like broad rhombic signal ( $g_{zyx} = 2.064, 1.967, 1.908$ ) that became predominant after 24 h and persisted from there on.

The conclusion that could be drawn from this experiment is that the amine bridgehead is likely to have an important but not critical role in the formation of the  $H_{trans}$ -like and  $H_{inact}$ -like states. As the C169S mutation has the effect of opening up more space into the active site pocket, its effect suggests that there might be factors involving the outer coordination sphere that influence the formation of the inhibited states. These effects include and are not limited to an active site more accessible to inhibitors, due to the reduced steric hindrance, and a change into the hydrogen-bonding network involving the H-cluster.

### 3.5. Conclusions

In this study we observed the formation of an inhibited  $H_{trans}$ -like state, which appears to be a thermodynamic sink for *CrHydA1* inside *E. coli* cells.

The identity of this state could not be proven definitively due to our inability to detect this state using other spectroscopic techniques, but the effect of sulfide on its formation and its stability strongly suggests that we are dealing with a species analogous to the reported  $H_{trans}$ .

As we discussed in section 1.3., the intracellular environment can be hostile to transition-metal catalysts as they can be exposed to several different inhibitors, with sulfide and other sulfur species possibly being included in the list.

This could represent an obstacle for the development of whole-cell biocatalytic systems, but the observation that *DdHydAB* does not accumulate this inhibited state indicates that one possible solution to the problem is a careful selection of the protein scaffold to use.

In our hands, both proton transfer and steric factors seem to be involved in the formation of the  $H_{trans}$ -like and  $H_{inact}$ -like states. A recent study has proposed a mechanism that could possibly explain our results.<sup>142</sup> In this model,  $H_2S$  initially interacts with  $[FeFe]$  hydrogenases in a non-competitive way, by replacing the water molecule in the proton transfer chain, while it binds to the

H-cluster only at a later time. Crystallographic data on the C299A mutant of *Clostridium pasteurianum* Cpl (a mutation to some extent analogous to C169S in CrHydA) show that one of the effect of the mutation is the presence of two water molecules in the active site channel instead of one.<sup>36</sup>

This model is consistent with our idea that the C169S mutation makes the active site pocket more accessible to small molecules and supports the proposition that steric factors could have a preponderant effect on the kinetics of the formation of the H<sub>trans</sub>-like and H<sub>inact</sub>-like states. Again, a careful selection of the protein scaffold to use, with particular attention to the accessibility of the active site to small molecules could be a possible solution to this problem.

As a final note, contrary to what has been reported for DdHydAB in vitro,<sup>79</sup> the H<sub>trans</sub>-like state does not seem to provide additional oxygen protection in whole-cell CrHydA1 samples. On the other hand, our experiments allowed us to appreciate the oxygen protection granted by the cellular envelope. Whole-cell samples exposed to oxygen for 1 h still have half or more of their H<sub>2</sub>-evolution activity preserved, whereas in vitro samples of CrHydA1 completely lose activity upon air exposure within minutes.<sup>43, 85</sup>

Combined with the previous results, this is a perfect example on how the whole-cell approach can be a double edged sword when it comes to biocatalysis.

# Chapter 4 - Paper III: H<sub>2</sub> production via an *E. coli* based semi-artificial photosynthetic system

## 4.1. Introduction and motivation

In the context of biological H<sub>2</sub> production, a promising approach is represented by the development of whole-cell semi-artificial photocatalytic systems, as described in section 1.3.2. In short, this strategy aims at creating bio-hybrid devices that, by benefitting both from the high efficiency and self-repairing properties of a biological whole-cell catalyst and from the light-harvesting properties of artificial photosensitizers (e.g. broadband light absorption), could prove superior to natural photosynthetic systems.

One of the main obstacles encountered in developing these whole-cell artificial photocatalytic systems is the difficulty in gaining mechanistic insight due to the intrinsic complexity of the whole-cell catalyst and of its interaction with the reaction environment. More specifically, in contrast to a molecular catalyst, a living cell exists in a state of constant mutual exchange with its environment; many parallel homeostatic processes are triggered every time there are changes in the surrounding conditions in order to try and counteract them.

In this study, by means of artificial maturation, we generate a whole-cell catalyst based on *E. coli* cells containing an [FeFe] hydrogenase, and we use it to build a semi-artificial photocatalytic model system. We take advantage of the high [FeFe] hydrogenase concentrations obtained to perform a basic spectroscopical characterization to verify the ability of the photosensitizer to transfer electrons to the enzyme upon illumination, and to check for the stability of the H-cluster under photocatalytic conditions.

Moreover, we approach the study and optimization of this model system using a mixed-level factorial design of experiments, with the goal of identifying relevant variables; and investigating the interactions and the relationships between them.<sup>143</sup> Finally, exploiting the oxygen-protection provided by the cellular envelope, we apply the same experimental design to identify parameters that might be relevant for increasing the resilience of the system towards this irreversible inhibitor.

## 4.2. System design

The model system employed in this study consists in a whole-cell hydrogen-evolving catalyst, based on  $[2\text{Fe}]^{\text{adt}}\text{-CrHydA1}$  inside *E. coli* cells, the organic photosensitizer eosin Y (EY) and triethanolamine (TEOA) as sacrificial electron donor in a PBS (Phosphate-Buffered Saline) buffer (Fig. 1).

As this work was being performed, Fujii and coworkers reported on a closely related system and showed that it was able to outperform similar systems based on inorganic photosensitizers.<sup>144</sup>

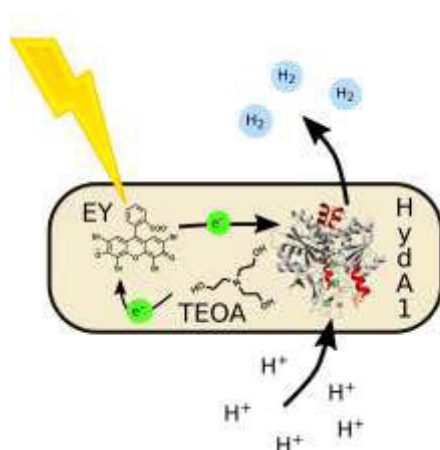


**Fig. 4.1** Graphical representation of the whole-cell semi-artificial photocatalytic system used in this study.

Contrary to what was reported in the aforementioned study, we chose not to co-express the maturation machinery for *CrHydA1* and to generate the mature enzyme via artificial maturation using the  $[2\text{Fe}]^{\text{adt}}$  complex. Other than allowing for a simpler growth and induction protocol, artificial maturation is known to be able to reliably generate spectroscopically-relevant amounts of mature enzyme inside the cells. Moreover, this choice allowed us to generate a system lacking catalyst repair and replacement capabilities; a feature we could take advantage of when investigating the stability and the oxygen-tolerance of the system itself.

## 4.3. Spectroscopic characterization

The light-induced reduction of  $[2\text{Fe}]^{\text{adt}}\text{-CrHydA1}$  was verified by a combination of ATR-FTIR and EPR spectroscopy (Fig. 4.2).

We performed ATR-FTIR by partially drying, via an inert gas flow, some of the reaction mix on an ATR crystal. The intrinsically diluted nature of the sample did not allow for the detection of the complete FTIR signature of the

H-cluster, but cofactor incorporation was verified by observing the two most intense bands (also called “reporter bands”) associated to the  $H_{ox}$  state (at 1964 and 1940  $cm^{-1}$ ). Upon illumination these two bands disappeared and gave way to the reporter bands for the  $H_{red}H^+$  and  $H_{sred}H^+$  states (at 1890 and 1881  $cm^{-1}$ , respectively) (Fig. 4.2A), thus providing evidence of a light-dependent H-cluster reduction.

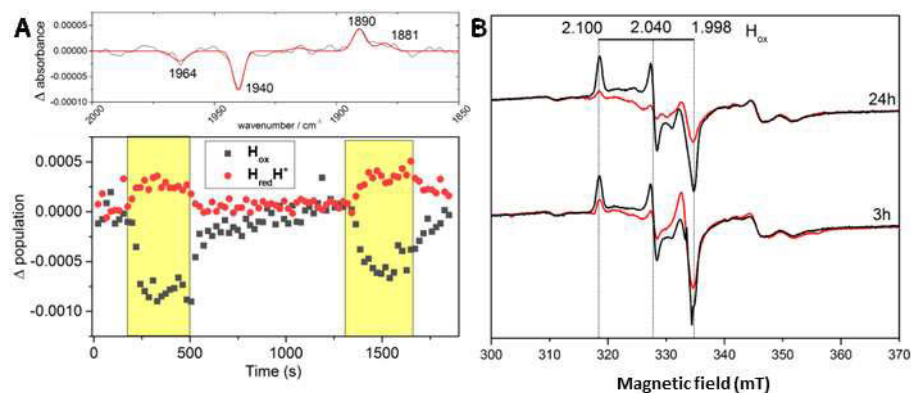


**Fig. 4.2** Assembly and photoreduction of the H-cluster verified via ATR-FTIR and EPR spectroscopy. **(A) Top:** difference spectrum measured on a semi-dry film obtained depositing the photocatalytic reaction mix on the ATR crystal, recorded before and after illumination (grey trace). The spectrum is overlaid with a peak-fitting (red trace), including the reporter bands of  $H_{ox}$  (1964 and 1940  $cm^{-1}$ ),  $H_{red}H^+$  (1890  $cm^{-1}$ ) and  $H_{sred}H^+$  (1881  $cm^{-1}$ ). **Bottom:** population changes for the  $H_{ox}$  and  $H_{red}H^+$  species, monitored over time. Periods of illumination are indicated by the yellow-coloured area. **(B)** EPR spectra recorded on a  $[2Fe]^{adt}$ -CrHydA1-containing cell suspension, in the presence of 100 $\mu$ M eosin Y and 100mM TEOA. Spectra were recorded after 3 h and 24 h of dark incubation (black traces) or continuous white-light illumination (red traces). g-values for the only discernible H-cluster signal, attributed to  $H_{ox}$ , are reported on an horizontal bar. EPR experimental parameters: temperature = 10K, power = 1mW, frequency = 9.28 GHz.

Both H-cluster assembly and photoreduction were supported by collecting EPR samples of whole-cell suspensions following dark incubation or continuous illumination for 3 h and 24 h (Fig. 4.2B).

Samples incubated in the dark showed a pure  $H_{ox}$  signature, with no signs of H-cluster inhibition or degradation even after 24 h.

Illumination induces a decrease of the signal intensity which, in light of the results obtained in ATR-FTIR, we can attribute to the accumulation of EPR-silent species such as  $H_{red}H^+$ .

The H-cluster appears stable also under illumination, with the 24 h sample displaying similar signal intensities as the 3 h one. Moreover, the lack of signals attributable to the  $H_{ox}$ -CO state indicate the absence of the expected H-cluster photodegradation, suggesting that the conditions employed in this study might be compatible with a long and sustained  $H_2$ -production.<sup>145</sup>

## 4.4. DoE and ANOVA

As mentioned before, we expect a photocatalytic system that includes a living cell to be a complex object to investigate. Compared to a molecular catalyst, the metabolic network of a bacterial cells presents more ways of adapting to and influencing the reaction environment. This has the potential to result in non-linear relations between the different reaction parameters.

To see what parameters are more critical in tuning the catalytic efficiency of our system, and to what extent they interact with each other, we applied a multivariate approach instead of a more common univariate one. We selected four variables: cell concentration (**OD<sub>600</sub>**), eosin Y concentration (**EY**), **pH** and light intensity (**LightT**). We chose a mixed-level design, with two levels assigned to each of the first three variables and three levels assigned to light intensity; the result was the scheme presented in Table 4.1.

**Table 4.1: Variables chosen for the design of the experiment and assigned levels.**

1) Cell concentration, measured as absorbance at 600 nm. 2) Eosin Y concentration. 3) Initial pH (PBS buffer, 100 mM). 4) Light intensity, in lux. The label assigned to each level for the ANOVA analysis is shown in parenthesis.

<b>OD<sub>600</sub><sup>1</sup></b>	<b>EY<sup>2</sup></b>	<b>pH<sup>3</sup></b>	<b>LightT<sup>4</sup></b>
1 (-1)	10 uM (-1)	6.5 (-1)	2500 lx (-1)
			4000 lx (0)
5 (+1)	100 uM (+1)	7.5 (+1)	5000 lx (+1)

The dataset deriving from the full-factorial combination of those variables and levels consists of 32 total runs (2<sup>5</sup>). The advantage of using a mixed-level design is that 8 of those runs serve as technical replicates, which can be used to estimate internal error and determine the statistical significance of the results.

Samples were prepared in sealed glass vials and placed under illumination, according to the variables scheme. The headspace was sampled and analyzed with a gas-chromatographer to measure H<sub>2</sub>-production after 2 h, 5 h, 9 h and 24 h of illumination (Fig. 4.3)

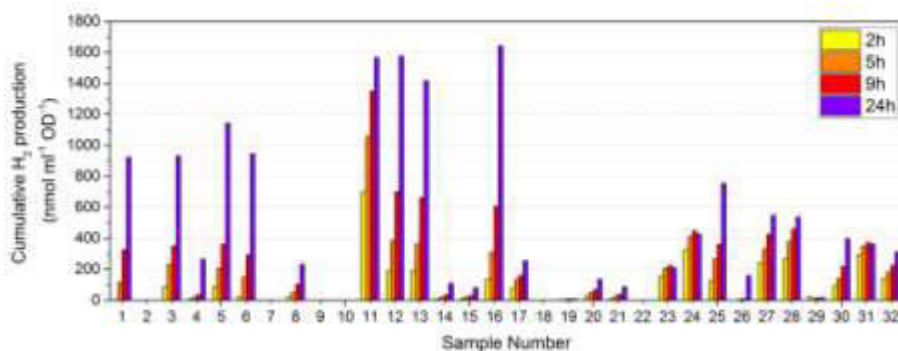


**Fig. 4.3** Cumulative H<sub>2</sub> production measured for each sample of the variables scheme after 2 h, 5 h, 9 h and 24 h of illumination. The sample number refers to a specific variables combination.

The wide range of activity and the different production profiles over time observed in the dataset indicates that the variables chosen have indeed an effect on the H<sub>2</sub>-production capability of our system. From this dataset it is already possible to identify the “best producers” based on total hydrogen produced, with samples 11, 12 and 16 being yielding approximately 1.6 μmol H<sub>2</sub> mL<sup>-1</sup> OD<sup>-1</sup> over the course of 24h, far surpassing the H<sub>2</sub>-production capabilities of the same whole-cell catalyst during glucose fermentation.<sup>130, 134, 138</sup>

Still, more information could be extracted from this dataset by using it to perform an **analysis of variance** (ANOVA), which allows to determine the influence on a response variable (in this case, cumulative H<sub>2</sub> production) of single independent variables (in this case, OD<sub>600</sub>, EY, pH and LightT) and of their higher-order interactions.

We decided to limit the size of the analysis and we applied a model including second- and third-order interaction only to the 5 h and 24 h subsets, as this would be sufficient to see how the influence of variables varies over time.

For each variable of variables combination the ANOVA analysis gives back a value indicating the amount of variance of the dataset that is explained by it (i.e. a sign of its influence) and an indication of the statistical significance of this value as a p-value. An example of an ANOVA table for my datasets is shown in Table 4.2 for the 5 h timepoint.



**Table 4.2: ANOVA table for the three-level model for the 5 h dataset.**

The table includes the label of the variables and combination of variables included in the model (Source). For each source the value of its contribution to the total variance (Sum. Sq.), the number of degrees of freedom (d.f.), the mean squares (Mean Sq., i.e. Sum Sq. per degree of freedom), the F-statistic (F) and the p-value (Prob>F) are given.

Analysis of Variance					
Source	Sum Sq.	d.f.	Mean Sq.	F	Prob>F
OD	270701.1	1	270701.1	21.83	0.0009
EY	287490.2	1	287490.2	23.18	0.0007
pH	68600.1	1	68600.1	5.53	0.0405
LightT	10581.4	2	5290.7	0.43	0.6641
OD*EY	109326.9	1	109326.9	8.82	0.0141
OD*pH	18022.5	1	18022.5	1.45	0.2558
OD*LightT	48488.9	2	24244.5	1.95	0.192
EY*pH	168059.5	1	168059.5	13.55	0.0042
EY*LightT	48298.2	2	24149.1	1.95	0.1931
pH*LightT	56751.1	2	28375.6	2.29	0.152
OD*EY*pH	17505.1	1	17505.1	1.41	0.2623
OD*EY*LightT	73967	2	36983.5	2.98	0.0964
OD*pH*LightT	119380.6	2	59690.3	4.81	0.0343
EY*pH*LightT	33147	2	16573.5	1.34	0.306
Error	124021.9	10	12402.2		
Total	1442533.7	31			

The analysis of the ANOVA matrix for the 5 h dataset shows that the contribution to the total variance of the internal error is limited to ~8% of the total variance, a value that can be considered quite low for a whole-cell system. This indicates that the applied protocol is reliable.

In terms of statistical significance, as there are no specific reasons to apply a more conservative approach, the conventional threshold value of  $< 0.05$  for the p-value is used also here. With this boundary set, we can see that, in terms of single variables, only the effect of OD<sub>600</sub> ( $p = 0.0009$ ), EY ( $p = 0.0007$ ) and pH ( $p = 0.0405$ ) can be considered statistically significant, whereas light intensity seems to be non-influential and differences in its value only explain ~1% of the total variance. This suggests that, on its own, the amount of photons hitting the sample is never the limiting factor for H<sub>2</sub>-production.

Moving to higher-order interaction, we can see that the ANOVA table indicates as relevant the interactions between OD<sub>600</sub> and EY (OD\*EY,  $p = 0.0141$ ), EY and pH (EY\*pH,  $p = 0.0042$ ) and of OD<sub>600</sub>, pH and light intensity (OD\*pH\*LightT,  $p = 0.0343$ ). In particular, this last piece of information suggests that light intensity is not a negligible factor, but that it should be studied strictly in relation to other variables.

The main effects and the interaction plots (Fig. 4.4) can be used to visualize the direction of the effect of these identified factors – whether they correlate positively or negatively with H<sub>2</sub> production – and the magnitude of this influence.

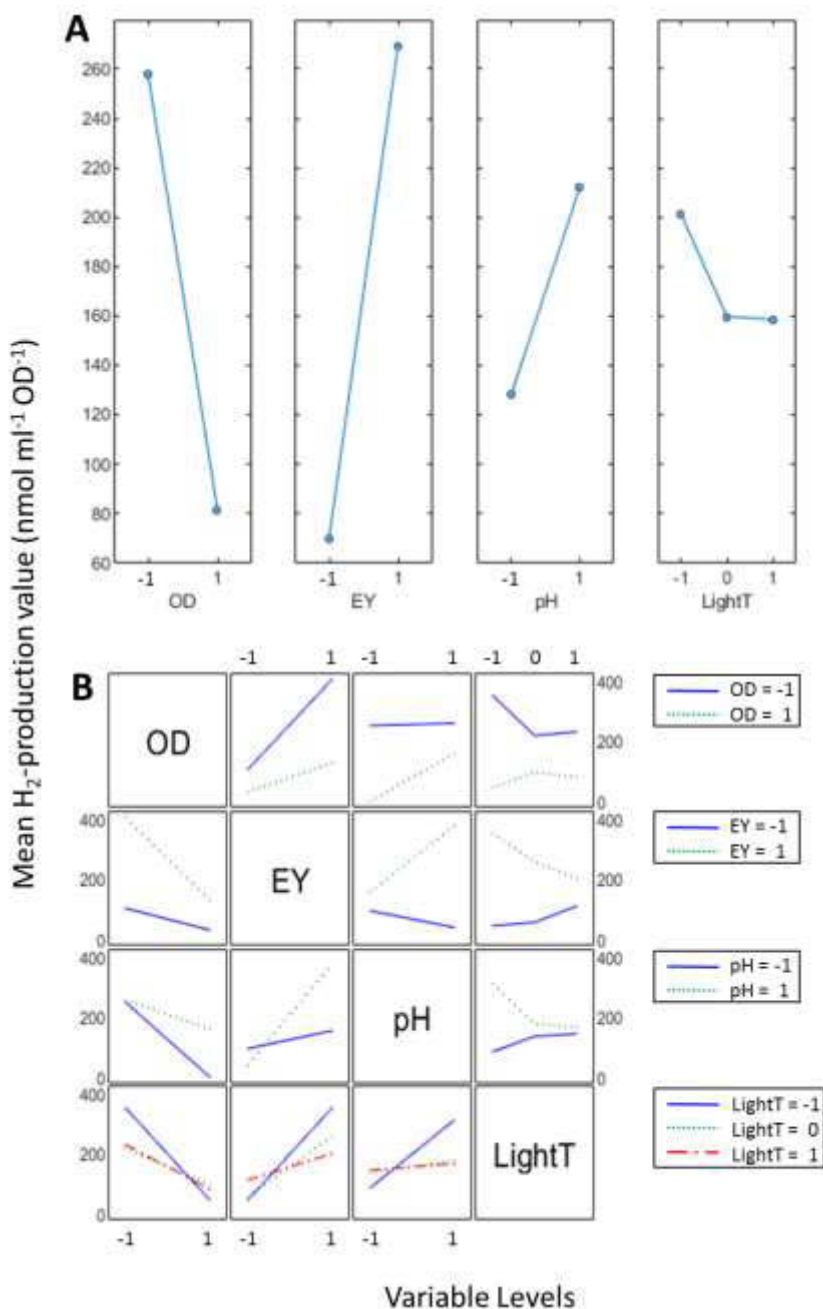


**Fig. 4.4 (A)** The main effect plots correlate the level of a single variable with the mean value of  $H_2$  production for samples with that variable at that level (-1, 0 or 1), and show their correlation as a two-points slope. **(B)** Each column of the interaction plot shows how the effect of a single variable influences  $H_2$ -production relative to the level of another variable in each row.

The analysis of the main effect plots it is evident that increasing OD<sub>600</sub> has a strong negative effect in terms of specific hydrogen production (Fig 4.4A, first plot from the left). This effect could be attributed to a denser suspension reducing light penetration in the sample. Alternatively, taking into consideration the observed interaction effect between OD and EY (Fig. 4.4B, second column from the left, first row from the top), it could be attributed to a reduced availability of photocatalyst per cell due to the denser suspension.

Another interesting piece of information regards the effect of pH, which appears counterintuitive. We indeed observe a high pH value correlating with higher H<sub>2</sub> production (Fig. 4.4A, third plot from the left), despite the fact that this effectively corresponds to a lower substrate (H<sup>+</sup>) concentration. Again, a better evaluation of this phenomenon can be done by looking at the interaction plot, which shows how the effect of pH is heavily influenced by the concentration of EY, suggesting an influence on the photochemical mechanism that would require a deeper investigation in order to be elucidated.

The ANOVA analysis on the 24 h dataset revealed that, for long term H<sub>2</sub>-production, OD and its interaction effect with pH contribute together for almost 50% of the total variance. The easiest explanation for this observation is also the most meaningful: a whole-cell system is not innocent. Cells and their metabolism influence and are influenced by the reaction environment, and this relationship can have dramatic effects on the yields of a photocatalytic system. On the contrary, a higher amount of eosin Y does not correlate with increase H<sub>2</sub>-production, which can be interpreted as an indication that the photosensitizer does not become a limiting factor on the long run.

#### 4.4.1. Oxygen tolerance

Following the observation that a cellular envelope is able to grant a good degree of protection to matured [FeFe] hydrogenases against oxygen damage, discussed in Chapter 3, we decided to see how much activity an optimized whole-cell photocatalytic system can retain upon air exposure.

We prepared a set of samples following the same design used above, except that we replaced 25% of the inert gas atmosphere of the glass vial with air, obtaining an atmosphere composed by ~5% O<sub>2</sub>.

When placed under continuous illumination, these samples were not producing any H<sub>2</sub>. This could be due either to O<sub>2</sub> rapidly quenching the excited photosensitizer or to H-cluster being irreversibly inhibited by O<sub>2</sub> or by other ROS

Light-induced H<sub>2</sub>-production was not completely lost when cells were given time to consume O<sub>2</sub> via respiration before illuminating the samples, by means of a 2 h incubation at 30°C in darkness. For most of these samples the amount of H<sub>2</sub> produced was low or negligible, but a few still displayed moderate levels of activity (Fig. 4.5).

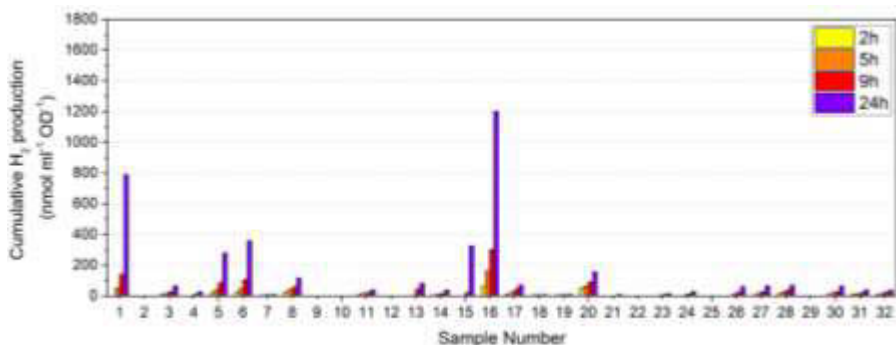


**Fig. 4.5** Cumulative H<sub>2</sub> production measured for each sample of a set exposed to a 5% O<sub>2</sub> atmosphere, incubated in the dark to allow for O<sub>2</sub> removal and illuminated for 2 h, 5 h, 9 h and 24 h. The sample number refers to a specific variables combination.

In particular, sample 16 clearly outclasses all other samples in the dataset in terms of amount of H<sub>2</sub> produced over the course of the experiment. This sample is assigned low levels for the OD, EY and pH and, interestingly, all other samples that were assigned the same levels for those variables (i.e. 1, 5 and 6, only differing in the level of the LightT variable) display higher-than-average levels of H<sub>2</sub> production.

As noted when discussing the design of our system (section 4.2), our *E. coli* strain is not co-expressing the maturation machinery of [FeFe] hydrogenases, and thus it is not capable of replacing damaged H-clusters. This means that the residual activity can only be attributed to enzymes surviving the oxygen exposure, a testament to the stability and to the resilience of [FeFe] hydrogenases under these whole-cell conditions. The ANOVA analysis highlighted a negative influence of EY concentration on H<sub>2</sub>-production, which could be related to the formation of reactive oxygen species (ROS) induced by the photosensitizer, and a strong interaction effect of OD and pH, again placing the spotlight on the cell metabolic state and, in this case, on its role in dealing with O<sub>2</sub> and ROS.

## 4.5. Conclusions

In this study, we have demonstrated light-dependent H<sub>2</sub>-production using a whole-cell semi-artificial photocatalytic system.

We have also applied whole-cell spectroscopy to prove the occurrence of electron transfer from the photosensitizer to [2Fe]<sup>ad</sup>-CrHydA1 by observing the light-induced accumulation of the reduced states H<sub>red</sub>H<sup>+</sup> and H<sub>sred</sub>H<sup>+</sup>.

The appearance of a signal attributable to H<sub>sred</sub>H<sup>+</sup> is of particular interest to us, as this state had escaped all of our investigative attempts in Paper I and this represents the first detection of this state under whole-cell conditions.

Furthermore, we have proven that it is possible to effectively study a complex whole-cell photocatalytic system using a design-of-experiment approach, as it seems that it is possible to identify controllable variables and vary them to gain insight into the inner workings of this type of systems. On our dataset, the results showed a limited influence of light intensity (reflected in a peak apparent quantum yield of 1.1%) implying that efforts should focus towards improving light use efficiency. There are many strategies that could lead to a good result, for instance using an artificial redox mediator (e.g. methyl viologen) or using strains overexpressing the [FeFe] hydrogenases' natural redox partners: ferredoxins.

Improving the bacterial host and optimizing the reaction conditions around it looks indeed a promising direction to follow. As we have observed, variables closely or directly related with the whole-cell catalyst often appear to be the most influential, especially in the case of long-term production and of O<sub>2</sub>-tolerance.

On a more general note, we have herein presented an oxygen-resistant platform and a simple experimental scheme that could be of interest for researchers trying to gain insight and to optimize also other (photo)catalytic systems involving notoriously O<sub>2</sub>-sensitive enzymes.

# Chapter 5 - Paper IV:

## Investigating the role of the strong field ligands in semi-synthetic hydrogenases: Spectroscopic and functional characterization of the asymmetric mono-cyanide active site.

### 5.1. Introduction and motivation

One of the most exciting new possibilities offered by artificial maturation is that of being able to generate modified version of the H-cluster by introducing different organometallic complexes into the active site.

This possibility has been already exploited to facilitate mechanistic studies of [FeFe] hydrogenases, utilizing pdt (propanedithiolate,  $^-\text{SCH}_2\text{CH}_2\text{CH}_2\text{S}^-$ ) and odt (oxodithiolate,  $^-\text{SCH}_2\text{OCH}_2\text{S}^-$ ) variants of the  $[\text{2Fe}]^{\text{adt}}$  synthetic mimic to help trap catalytic intermediates,<sup>67, 75, 84</sup> and even using mimics based on ruthenium to gain insight into hydride-bound species of the H-cluster.<sup>146</sup>

A recent screening of several mono- and di-iron mimics, has shown how flexible the active site pocket can be in accommodating cofactors with different sterick hindrances and CO/CN<sup>-</sup> ligands ratios.<sup>55</sup>

So far only two variants of the  $[\text{2Fe}]^{\text{adt}}$  complex, other than  $[\text{2Fe}]^{\text{adt}}$  itself, have shown relevant catalytic activities. The first one was a variant where the adt ligand was replaced by an azadiselenate ( $-\text{SeCH}_2\text{NHCH}_2\text{Se}-$ ) that was inserted into both CpI and *CrHydA1* scaffolds, yielding enzyme variants with 80% and 120% of the H<sub>2</sub>-evolution activities of their native counterparts, respectively.<sup>147</sup> The second one is the mono-cyanide variant of  $[\text{2Fe}]^{\text{adt}}$  ( $[\text{2Fe}]^{\text{monoCN}}$ , Fig. 5.1B), which was inserted into *CrHydA1* as part of the aforementioned screening. This variant showed roughly half the H<sub>2</sub>-evolution activity as the native enzyme, which sparked our interest because the seemingly minor replacement of a CN<sup>-</sup> ligand by a CO ligand is expected to have a huge effect on the electronic structure of the resulting H-cluster, as the CO ligand is a better electron-withdrawing group compared to CN<sup>-</sup>. Another interesting characteristic of  $[\text{2Fe}]^{\text{monoCN}}$  is its asymmetry (i.e. a di-iron complex where the two iron ions do not have the same ligands coordinating them). Working with an asymmetric mimic is fascinating for mainly two reasons:

- a [FeFe] hydrogenase matured with an asymmetric complex can theoretically have two different H-cluster configurations (or isomers), based on which iron ion is going to be coordinated by the bridging cysteine. In the case of  $[2\text{Fe}]^{\text{monoCN}}$  these two isomers would be lacking the  $\text{CN}^-$  on either the proximal or the distal iron and all of the second-coordination sphere interactions related to it (Fig. 5.1A and 5.1C).
- inserting an asymmetric cofactor into an [FeFe] hydrogenases represent the exploration of a chemical space that is precluded to the native maturation machinery which, by design, is limited to building and inserting symmetrical cofactors (see section 1.2)

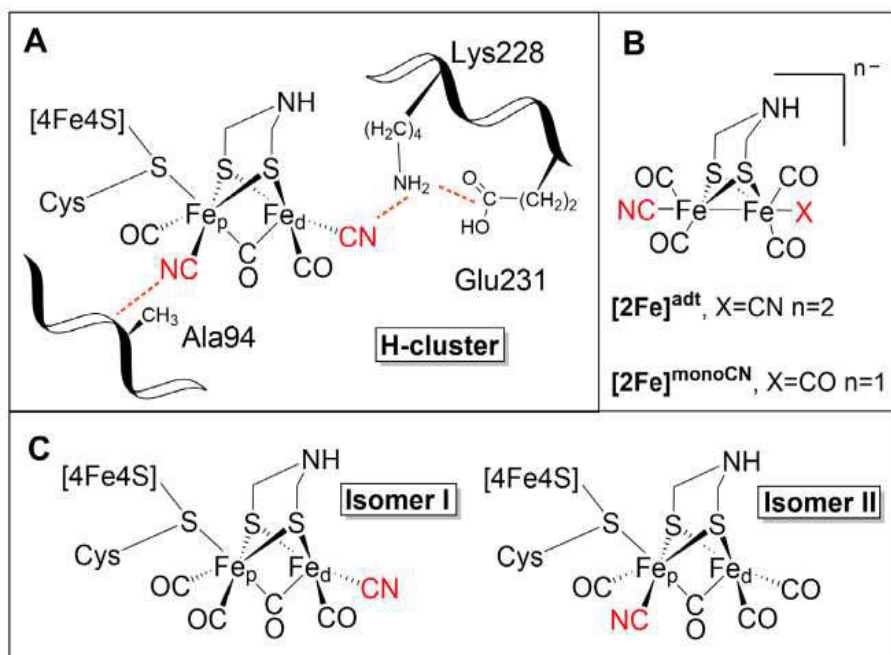


**Fig. 5.1** (A) Schematic representation of the active site of a [FeFe] hydrogenase, including the H-cluster and selected amino acids interacting with the diatomic ligands (numbering based on *CrHydA1*). H-bond and salt-bridge interactions are marked as red dashed lines. (B) Structures of the  $[2\text{Fe}]^{\text{adt}}$  and of the  $[2\text{Fe}]^{\text{monoCN}}$  synthetic complexes. (C) Schematic representation of the two possible isomer forms of the H-cluster obtained following maturation using the  $[2\text{Fe}]^{\text{monoCN}}$  complex. In all panels, the  $\text{CN}^-$  ligands are highlighted in red.

In this study, we use  $[2\text{Fe}]^{\text{monoCN}}$  to mature two different [FeFe] hydrogenase scaffolds: the monomeric enzyme *CrHydA1* from *Chlamydomonas reinhardtii* and the heterodimeric enzyme *DdHydAB* from *Desulfovibrio desulfuricans*. We show that the complex is able to bind to the  $[4\text{Fe4S}]_{\text{H}}$  cluster and

forms a single isomer of the H-cluster with both *apo*-hydrogenases. Interestingly though, the protein scaffold has a strong influence on the catalytic and spectroscopic properties of the resulting enzymes.

## 5.2. Cofactor insertion and spectroscopic characterization

### 5.2.1. FTIR

[2Fe]<sup>monoCN</sup> insertion was successful for both protein scaffolds, and proceeded similarly to what is observed during maturation with [2Fe]<sup>adt</sup> in both cases. For *DdHydAB*, a 48h incubation was required and the resulting holo-enzyme displayed an FTIR spectrum suggestive of a single isomer and a pure state. The five narrow H-cluster-like bands consist of a single CN<sup>-</sup> band (2057 cm<sup>-1</sup>), three intense band in the typical terminal-CO ligands region (1969, 1923 and 1903 cm<sup>-1</sup>) and one low energy band (1835 cm<sup>-1</sup>) attributable to a  $\mu$ CO ligand (Fig. 5.2A).

The maturation process in *CrHydA1* proceeded more rapidly, only requiring only 90 minutes. In addition to a set of five sharp H-cluster-like features (2080, 1953, 1922, 1843, 1778 cm<sup>-1</sup>), the FTIR spectrum of [2Fe]<sup>monoCN</sup>-*CrHydA1* also displays some broader band approximately around 2044, 2013 and 1980 cm<sup>-1</sup> (Fig. 5.2D, spectrum a). These bands are attributable to non-specifically bound complex and are indeed also observed when using [2Fe]<sup>monoCN</sup> to mature a demetallized *CrHydA1* enzyme (i.e. lacking the anchoring [4Fe4S]<sub>H</sub> cluster), which is unable to integrate the complex to form an H-cluster (Fig. 5.2D, spectrum b). Moreover, these non-specific bands showed light-sensitivity and exposing the enzyme to white light selectively degraded them, leaving the H-cluster bands unchanged (Fig. 5.2D, spectra c). On [2Fe]<sup>monoCN</sup>-*DdHydAB*, light treatment had no visible effect, which by itself is a striking feature, as the H-cluster [2Fe]<sup>adt</sup>-*DdHydAB* is known to degrade upon light-exposure.<sup>145</sup>

The FTIR spectra of both enzymes only show a single, clearly discernible, CN<sup>-</sup> band, which indicates the occurrence of one single isomer.

The difference in band positions between [2Fe]<sup>monoCN</sup>-*CrHydA1* and [2Fe]<sup>monoCN</sup>-*DdHydAB* is bigger than what would be expected for the two enzymes residing in the same redox state, based on what is observed for the [2Fe]<sup>adt</sup> variants, and strongly suggests variations in both oxidation state and possibly cofactor geometry.



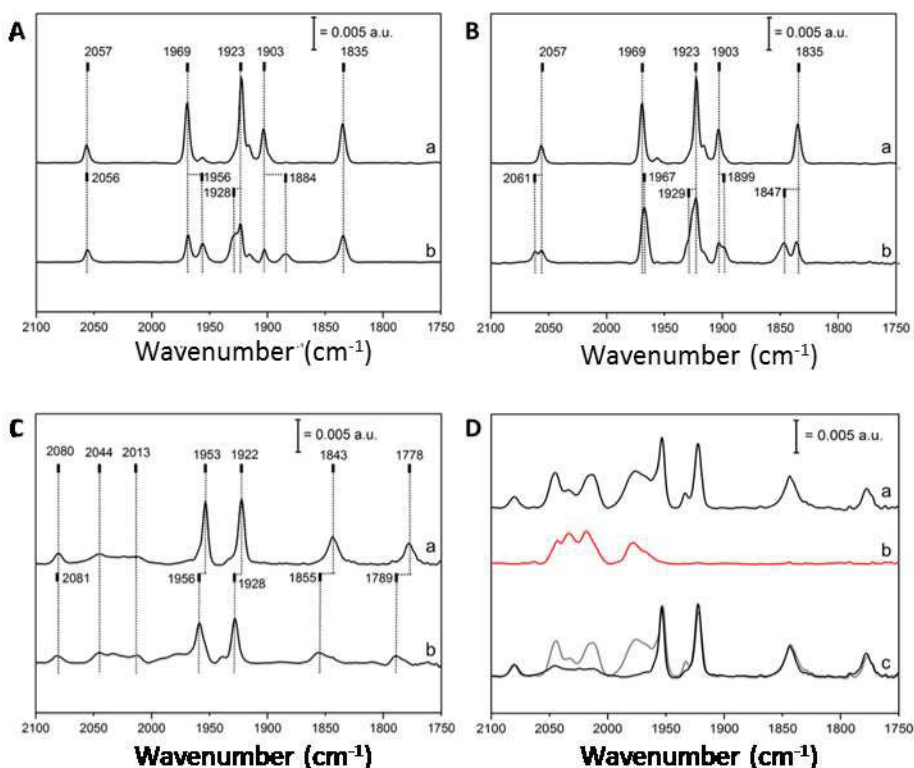


**Fig. 5.2** (A) FTIR spectra of  $[2\text{Fe}]^{\text{monoCN}}\text{-DdHydAB}$  recorded before (**spectrum a**) and following addition of 10 mM NaDT (**spectrum b**). (B) FTIR spectra of  $[2\text{Fe}]^{\text{monoCN}}\text{-DdHydAB}$  recorded before (**spectrum a**) and following addition of 10 mM  $\text{Eu}^{\text{II}}$ -DTPA (**spectrum b**). (C) ATR-FTIR spectra of  $[2\text{Fe}]^{\text{monoCN}}\text{-CrHydA1}$  recorded before (**spectrum a**) and following addition of 10 mM NaDT (**spectrum b**). (D) **Spectrum a**: ATR-FTIR spectrum of an as prepared  $[2\text{Fe}]^{\text{monoCN}}\text{-CrHydA1}$  sample, with the broad non-specific bands being visible in the 2050-1950  $\text{cm}^{-1}$  spectral region. **Spectrum b**: ATR-FTIR spectrum of demetalized  $\text{CrHydA1}$  incubated with the  $[2\text{Fe}]^{\text{monoCN}}$  complex and showing similar broad features as in spectrum a in the 2050-1950  $\text{cm}^{-1}$  spectral region. **Spectra c**: the spectrum from an as prepared  $[2\text{Fe}]^{\text{monoCN}}\text{-CrHydA1}$  sample (*grey trace*) is overlaid to the much cleaner spectrum resulting from its white light treatment (*black trace*).

Reduction of  $[2\text{Fe}]^{\text{monoCN}}\text{-DdHydAB}$  with NaDT ( $E^{0'} = -0.66$  V vs NHE) resulted in a limited reactivity and in the partial generation of a new state, clearly identifiable from the bands appearing in the FTIR spectrum at 1956, 1928 and 1884  $\text{cm}^{-1}$  (Fig. 5.2A). Using a stronger reductant, specifically  $\text{Eu}^{\text{II}}$ -DTPA ( $E^{0'} = -1.09$  V vs NHE), also resulted in a partial reaction and triggered a distinct hypsochromic shift of most of the spectral features, instead of the expected bathochromic shift (Fig. 5.2B). A similar effect was observed upon addition of NaDT on  $[2\text{Fe}]^{\text{monoCN}}\text{-CrHydA1}$  samples. (Fig. 5.2C).

The position of the FTIR bands, with relatively low-frequencies for the  $\text{CN}^-$  band of  $[\text{2Fe}]^{\text{monoCN}}\text{-DdHydAB}$  ( $2057\text{ cm}^{-1}$ ) and even more so for the  $\mu\text{CO}$  band of  $[\text{2Fe}]^{\text{monoCN}}\text{-CrHydA1}$  ( $1778\text{ cm}^{-1}$ ), combined with the limited and unusual reactivity towards reductant indicates that the H-clusters of both enzymes could be residing in singly or doubly-reduced states.

### 5.2.2. EPR

We consolidated the spectroscopic characterization of these two enzyme variants using EPR. Samples of  $[\text{2Fe}]^{\text{monoCN}}\text{-DdHydAB}$  show no discernible H-cluster signal, which together with the results of the FTIR characterization leads to the conclusion that the H-cluster of  $[\text{2Fe}]^{\text{monoCN}}\text{-DdHydAB}$  is residing in a state analogous to the EPR-silent singly reduced  $\text{H}_{\text{red}}\text{H}^+$  state.

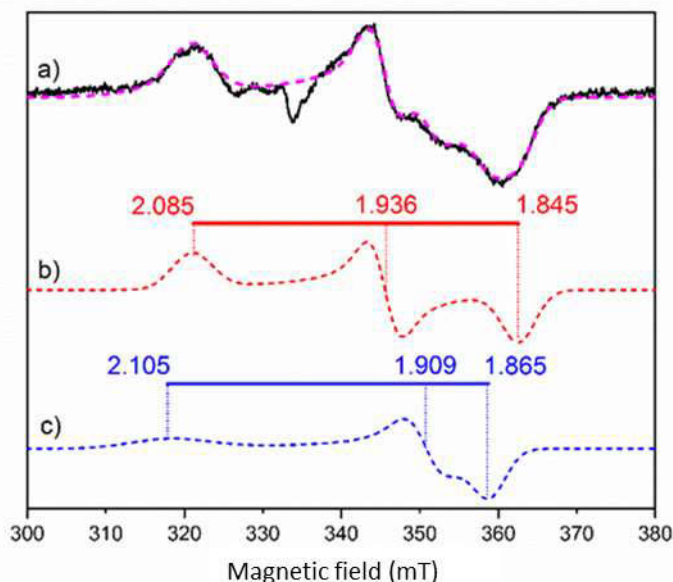


**Fig. 5.3** EPR spectrum recorded on a  $[\text{2Fe}]^{\text{monoCN}}\text{-CrHydA1}$  sample at pH 8 a) Experimental data (black) is overlaid with a two-components simulated spectrum (pink dashed line). b) Simulated rhombic signal ( $g_{\text{zyx}} = 2.085\ 1.936\ 1.845$ ) representing the first component of the two-components simulated spectrum c) S Simulated rhombic signal I ( $g_{\text{zyx}} = 2.105\ 1.909\ 1.865$ ) representing the second component of the two-components simulated spectrum. Experimental parameters: Frequency: 9.365 GHz Temperature = 10 K; microwave power =  $64\mu\text{W}$

In contrast, samples of  $[\text{2Fe}]^{\text{monoCN}}\text{-CrHydA1}$  displayed a spectrum consisting of a mixture of two rhombic signals, with  $g_{\text{zyx}} = 2.085, 1.936, 1.845$  and  $g_{\text{zyx}} = 2.105, 1.909, 1.865$  (Fig. 5.3). The two signals appear to be relatively anisotropic and fast-relaxing, both properties typical of H-cluster redox states with

a  $[\text{Fe}_4\text{S}]_{\text{H}}$ -centered paramagnetic species. This indicates that under similar conditions the two enzymes stabilize different states of the H-cluster, with  $[\text{Fe}]^{\text{monoCN}}$ -CrHydA1 likely residing in an  $\text{H}_{\text{red}}\text{H}^+$ -like state.

The observation of two separate signals for  $[\text{Fe}]^{\text{monoCN}}$ -CrHydA1 appears to be non-consistent with the single set of peaks observed with FTIR. This discrepancy can be attributed to the cryogenic temperatures employed in EPR measurements, which could freeze different ligand conformations (or rotamers) that instead are averaged out in room temperature spectroscopy, as reported in model complexes.<sup>148</sup>

Ligand rotation on the distal iron is a phenomenon that has been proposed to occur in  $[\text{FeFe}]$  hydrogenases upon CO inhibition;<sup>149</sup> in our case, an increased ligand flexibility could be the direct consequence of the lack of the distal  $\text{CN}^-$  ligand and consequently of the hydrogen bonding network involving it.

### 5.3. Determining the isomer form

As pointed out in section 5.2.1, FTIR suggests the occurrence of a single configuration, and the increase ligand flexibility discussed hereabove is compatible with the prevalent formation of isomer II (Fig. 5.1).

In order to verify this hypothesis, we decided to generate mutants of CrHydA1 targeting amino acidic residues in the active pocket being part of the second-coordination sphere for both  $\text{Fe}_{\text{d}}$  and  $\text{Fe}_{\text{p}}$ .

On the  $\text{Fe}_{\text{d}}$  side, finding a target is not an easy task. In CrHydA1, the only amino acid known to directly interact with the distal  $\text{CN}^-$  ligand is Lysine228, which is an extremely conserved residue and whose mutation unavoidably results in enzyme unable to incorporate an H-cluster<sup>150, 151</sup>. The choice fell on Glutamate231, a residue involved in a salt-bridge with Lysine228, whose conservative mutation to an aspartate (E231D) can be seen reflected in the FTIR spectrum of the resulting mutant.<sup>63</sup> Even in this mutant, though, incorporation of  $[\text{Fe}]^{\text{monoCN}}$  proved impossible. This is compatible with the role of Lysine228 as the final amino-acid belonging to the maturation channel, with any mutation changing its position having a dramatic influence on H-cluster incorporation.<sup>27, 63, 150</sup>

On the  $\text{Fe}_{\text{p}}$  side, Alanine94 was chosen as target for mutation, as it is known to interact with the proximal  $\text{CN}^-$  ligand forming an hydrogen bond *via* its backbone amide. Moreover, its mutation to serine (A94S) is reported to result in a large shift of the proximal  $\text{CN}^-$  FTIR band, with no effect observable on the distal  $\text{CN}^-$  band, making this mutation a perfect probe to distinguish between the two possible isomers.

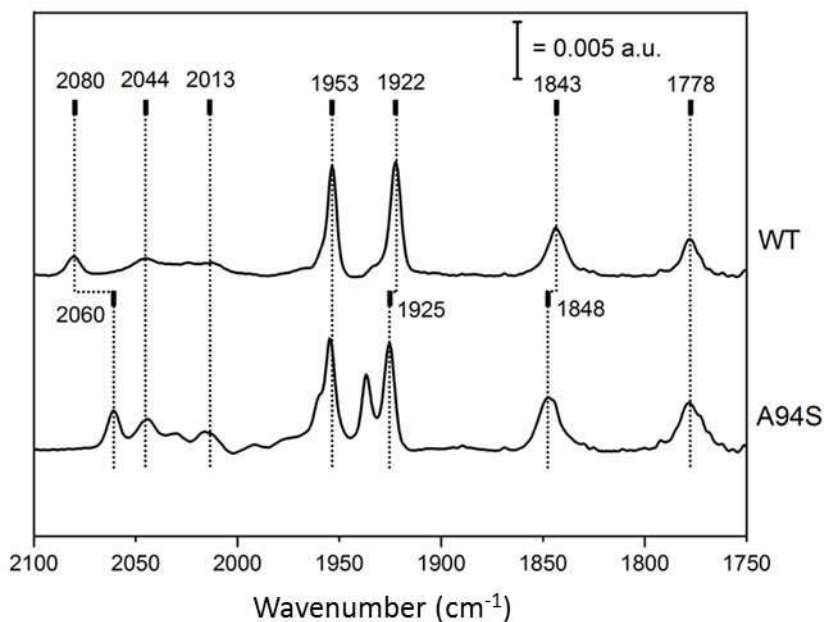


**Fig. 5.4** Room temperature ATR-FTIR spectra of  $[2\text{Fe}]^{\text{monoCN}}\text{-CrHydA1}$  (WT) and  $[2\text{Fe}]^{\text{monoCN}}\text{-CrHydA1}^{\text{A94S}}$ . The wavenumbers of the the most prominent bands are given as labels, and the wavenumber shifts induced by the point-mutation can be followed through the dotted lines.

The FTIR spectrum of a  $[2\text{Fe}]^{\text{monoCN}}$ -matured A94S mutant ( $[2\text{Fe}]^{\text{monoCN}}\text{-CrHydA1}^{\text{A94S}}$ ) showed in addition to smaller shifts ( $3\text{-}5\text{ cm}^{-1}$ ) involving two of the terminal CO bands, a  $20\text{ cm}^{-1}$  red-shift involving the sole  $\text{CN}^-$  band, confirming the prevalence of isomer II upon maturation of *CrHydA1* with  $[2\text{Fe}]^{\text{monoCN}}$  (Fig. 5.4).

The spectrum of  $[2\text{Fe}]^{\text{monoCN}}\text{-CrHydA1}^{\text{A94S}}$  also shows the appearance of two additional CO bands at  $1959$  and  $1936\text{ cm}^{-1}$  which can only be attributed to the effect of the mutation, as all sample preparation followed the same protocol as for the WT enzyme. As the A94S mutation effectively introduces next to  $\text{Fe}_p$  a polar residue capable of H-bonding, the result could be that of triggering the formation of two different ligand conformations, or to slow down ligand rotation allowing for the distinction of these two conformations also at room temperature, partially replicating the effect observed in cryo-EPR.

## 5.4. Reactivity towards inhibitors

Compared to their native counterpart, enzymes mature with  $[2\text{Fe}]^{\text{monoCN}}$  show very different reactivity towards the inhibitors CO and  $\text{O}_2$ .

Both  $[2\text{Fe}]^{\text{monoCN}}\text{-CrHydA1}$  and  $[2\text{Fe}]^{\text{monoCN}}\text{-DdHydAB}$  show no reactivity towards CO, up to 1 atm. This is striking especially for *DdHydAB*, which in its native form has high affinity for this competitive inhibitor, and it is often isolated predominantly in the  $\text{H}_{\text{ox}}\text{-CO}$  state.<sup>85, 152</sup>

The possibility that  $[2\text{Fe}]^{\text{monoCN}}\text{-DdHydAB}$  would be already residing in a CO-inhibited state was excluded both by observing CO-release during maturation and by observing no change to the as prepared spectrum upon promoting CO-release with an extensive (48 h)  $\text{N}_2$  flush.

$[2\text{Fe}]^{\text{monoCN}}\text{-DdHydAB}$  also displays enhanced tolerance towards  $\text{O}_2$ , retaining 36% of its FTIR signal intensity after 30 minutes of air exposure, whereas  $[2\text{Fe}]^{\text{adt}}\text{-DdHydAB}$  loses ~85% of it just after 5 minutes.

Conversely, exposing  $[2\text{Fe}]^{\text{monoCN}}\text{-CrHydA1}$  to atmospheric concentrations of  $\text{O}_2$  results in a complete disappearance of the original five H-cluster bands within a few minutes. At the same time we could see the appearance of three small bands (2097, 2024, 1985  $\text{cm}^{-1}$ ) that are reminiscent of the air-induced  $\text{H}_{\text{air-ox}}$  state reported in *TamHydS*.<sup>30</sup> This spectral signature, consisting of two CO and  $\text{CN}^-$  bands, is compatible with an H-cluster in the isomer II conformation losing the all-carbonyl  $\text{Fe}_d$  and forming a partially degraded H-cluster where a single Fe ion (formerly  $\text{Fe}_p$ ) is coordinated by the bridging cysteine, two CO and one  $\text{CN}^-$ .

## 5.5. Catalytic properties

The results shown so far clearly indicate that the monoCN variants of *CrHydA1* and *DdHydAB* possess different redox and structural properties compared to their native counterparts. We then decided to investigate whether these differences would translate into differences in the catalytic properties of these enzymes.

As previously reported,  $[2\text{Fe}]^{\text{monoCN}}\text{-CrHydA1}$  retains a significant portion of  $\text{H}_2$ -evolution activity, with of  $223 \pm 25 \mu\text{mol H}_2 (\text{mg protein})^{-1} \text{ min}^{-1}$  vs. the  $370 \pm 64 \mu\text{mol H}_2 (\text{mg protein})^{-1} \text{ min}^{-1}$  of the native  $[2\text{Fe}]^{\text{adt}}\text{-CrHydA1}$  observed in our hands. This is strikingly different to what happens with  $[2\text{Fe}]^{\text{monoCN}}\text{-DdHydAB}$ , which only displays very minor residual  $\text{H}_2$ -evolution and  $\text{H}_2$ -oxidation activities (1% and 0.02% of the activities of  $[2\text{Fe}]^{\text{adt}}\text{-DdHydAB}$ , respectively).

Similarly, Protein Film Electrochemistry (PFE) experiments performed on  $[2\text{Fe}]^{\text{monoCN}}\text{-DdHydAB}$  films showed no catalytic current neither in the oxidative nor in the reductive direction. On the contrary, the cyclic voltammograms (CVs) recorded on films of  $[2\text{Fe}]^{\text{monoCN}}\text{-CrHydA1}$  showed the typical behaviour of a bidirectional and reversible catalyst, with the current crossing the zero-current level at exactly the thermodynamical potential (Fig. 5.5). Interestingly, the CVs showed no sign of low-potential inactivation, a well-known phenomenon in  $[2\text{Fe}]^{\text{adt}}\text{-CrHydA1}$ .<sup>153</sup>

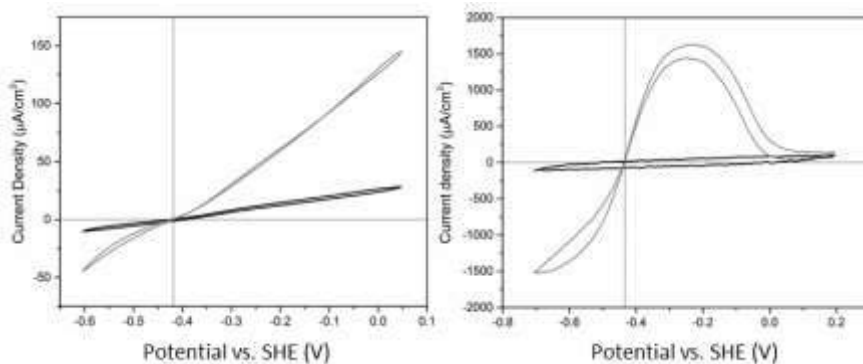


Fig. 5.5 **(A)** Cyclic voltammograms for [2Fe]<sup>adt</sup>-CrHydA1 (grey) and [2Fe]<sup>monoCN</sup>-CrHydA1 (black) recorded in a pH 7 halide-free buffer and under 1 atm H<sub>2</sub>. Experimental conditions: rotation rate = 3000 rpm, temperature = 30°C, scan rate = 10 mV/s. **(B)** Cyclic voltammograms for [2Fe]<sup>adt</sup>-DdHydAB (grey) and [2Fe]<sup>monoCN</sup>-DdHydAB (black) recorded in a pH 7 NaCl-containing buffer and under 1 atm H<sub>2</sub>. Experimental conditions: rotation rate = 3200 rpm, temperature = 25°C, scan rate = 20 mV/s. In both panels, a vertical dotted line indicates the thermodynamic potential for the H<sub>2</sub>/H<sup>+</sup> couple at pH 7, while a horizontal dotted line marks the zero-current level.

We were able to estimate the catalytic bias as the ratio between oxidative and reductive currents at 100 mV overpotential ( $i_{\text{ox}}/i_{\text{red}}$ ) and we determined it to be  $\approx 1.6$ , not too different from the value measured for [2Fe]<sup>adt</sup>-CrHydA1 ( $i_{\text{ox}}/i_{\text{red}} \approx 1.5$ ) and indicating an enzyme biased towards H<sub>2</sub>-oxidation. We were also able to estimate the  $K_m$  for H<sub>2</sub>, measuring current intensity as a function of H<sub>2</sub> partial pressure. As we observed a linear correlation between current intensity and H<sub>2</sub> concentration, we could only estimate  $K_m$  to be higher than the maximum partial pressure we applied (1 atm), still a much higher value than the  $0.64 \pm 0.05$  atm reported for [2Fe]<sup>adt</sup>-CrHydA1.<sup>154</sup>

## 5.6. Conclusions

The characterization of monoCN variants of [FeFe] hydrogenases has provided a lot of information on the role that first and second coordination spheres have in tuning the properties of these enzymes.

As I mentioned before, mutations targeting the Lysine228 residue in CrHydA1 (or its homologs in other hydrogenases) unavoidably result in enzyme variants lacking the H-cluster, and this has limited the possibilities to investigate the role of the interaction between this residue and the distal CN<sup>-</sup> ligand (dCN). Having determined that the maturation with [2Fe]<sup>monoCN</sup> yields an H-cluster lacking this ligand (isomer II), we finally had the opportunity to study variants where the aforementioned interaction is disrupted.

The relatively high residual activity exhibited by  $[2\text{Fe}]^{\text{monoCN}}\text{-CrHydA1}$  seems to indicate that the Lysine228-dCN interaction is not critical for catalysis, despite being undoubtedly important for cofactor insertion and possibly for tuning the electron density on dCN.

Following this hypothesis, the lack of activity of  $[2\text{Fe}]^{\text{monoCN}}\text{-DdHydAB}$  could be the consequence of another important function of Lysine228 and its homologs: contributing to the stabilization of the rotated structure of  $\text{Fe}_d$  and to the positioning of the open coordination site in an apical position. The formation of alternative rotated structures could explain both the lack of activity, due to the open coordination site no longer being able to form a frustrated Lewis pair with the bridgehead amine, and the complete loss of affinity towards CO, due to the apical coordination site being already occupied by another CO ligand.

The hypothesis of an increased rotational freedom on  $\text{Fe}_d$  is also supported by the observation of two different forms for the H-cluster in the low-temperature EPR spectrum of  $[2\text{Fe}]^{\text{monoCN}}\text{-CrHydA}$ .

From a catalyst design perspective, the study of  $[2\text{Fe}]^{\text{monoCN}}\text{-CrHydA1}$  showed an interesting phenomenon connected to the influence of the H-cluster on the overall catalytic performance of  $[\text{FeFe}]$  hydrogenases: the  $\text{CN}^-$ -to-CO ligand replacement caused a decrease of  $\text{H}_2$ -production rate, and reduced the affinity for both substrate ( $\text{H}_2$ ) and inhibitors (CO), but had no effect on its reversibility (defined as its ability to work in either direction in response to a small overpotential)<sup>155</sup>. This provides a good example of how directionality, TOF and reaction overpotential are decoupled parameters for redox catalysts.<sup>155, 156</sup>

Based on the diverging results obtained during the spectroscopic and catalytic characterization of these two monoCN variants, it is apparent that the choice of the scaffold can have a huge impact on the results obtained when studying H-cluster variants. The community has become aware of this issue as more and more  $[\text{FeFe}]$  hydrogenases have been isolated and characterized (see sections 1.2.1. and 1.2.3.) and will have to take scaffold diversity into consideration when developing semi-artificial enzymes. Yet, this study shows that it is possible to rely on hydrogenase scaffolds to exert directional control during the introduction of asymmetric synthetic mimics into the active site, opening the door for the development of a whole new class of semi-artificial  $[\text{FeFe}]$  hydrogenases.

## Chapter 6 – Summary and Outlook

It has been more than 90 years since hydrogenases were discovered,<sup>157</sup> yet there are still many more things about them that we need to understand and the [FeFe] hydrogenase community is more alive and vibrant than ever.

One of the most recent breakthroughs in [FeFe] hydrogenases research has been for sure the discovery of artificial maturation, which helped solving the debate around the identity of the bridgehead atom of the H-cluster and has led to streamlining of enzyme preparation procedures.<sup>28, 54</sup> Even more recently, artificial maturation has been successfully applied in a whole-cell context and this has branched out into a whole new subfield.<sup>112, 130</sup>

In Paper I, we have moved our first steps into this latter subfield, and we have seen how whole-cell artificial maturation can be utilized to probe the catalytic cycle of [FeFe] hydrogenases under intracellular conditions.

Specifically, we have been able to accumulate and identify four known proposed catalytic intermediates, thereby supporting their physiological relevance for the catalytic cycle *in vivo*. Of particular interest is the detection of the elusive hydride state  $H_{hyd}H^+$ , which accumulated in the absence of any non-physiological reductant. This finding further solidified the notion of presence of terminal hydride states in the physiological catalytic cycle and it represents another step toward the clarification of the complex hydride chemistry of the H-cluster.

In Paper II, we have been reminded that not all that glitters is gold. The whole-cell environment can be hostile to transition-metal catalysts, and [FeFe] hydrogenases are no exception to the rule. We have seen how, inside *E. coli* cells, [FeFe] hydrogenases tend to lose activity over time and enter a thermodynamically stable inhibited state, probably analogous to the  $H_{trans}$  and  $H_{inact}$  states reported for *DdHydAB*. We have then investigated the factors influencing the formation of this state and proposed strategies to try and minimize this process. Some gold was found in the end though, as we were able to show the outstanding degree of oxygen protection that *E. coli* cells can provide for oxygen-sensitive catalysts.

In Paper III, we have demonstrated the possibility to drive  $H_2$ -production with light using an [FeFe] hydrogenase-based whole-cell catalyst coupled with a synthetic photosensitizer. We have demonstrated that the [FeFe] hydrogenase is able to receive electrons from the photosensitizer and that this process drives part of the catalysis. Furthermore, we have proposed a relatively



simple method to investigate the complex interplay of the different parameters in this, and similar, semi-artificial photocatalytic systems. By applying it to our system, we have put the spotlight on the central role that the whole-cell catalyst's metabolism has on influencing the product yield, and we have identified promising targets for a future system optimization.

Finally, in Paper IV, we have moved away from whole-cell studies to take one step along another freshly paved road: we have inserted the non-native  $[2\text{Fe}]^{\text{monoCN}}$  synthetic cofactor into the *CrHydA1* and *DdHydAB* scaffolds, and we have characterized the resulting enzyme variants both spectroscopically and catalytically. The diverging results obtained with the two variants are indicative of how the choice of the scaffold can influence the structural and catalytical properties of an  $[\text{FeFe}]$  hydrogenase. The most interesting finding though was the observation that, despite  $[2\text{Fe}]^{\text{monoCN}}$  being an asymmetrical complex, its insertion in the active site pocket results in the formation of one single H-cluster conformation with the sole  $\text{CN}^-$  ligand being bound to the proximal iron. The resulting lack of a distal  $\text{CN}^-$  has effectively allowed us to study enzyme variants with a disrupted H-bonding network close to the distal iron, a feat that was not achievable with mutations in the active site pocket. Thereby, we could gain more insight into the role of H-bonding in stabilizing the rotational conformation of the distal iron ligands.

Moreover, the finding that we can rely on  $[\text{FeFe}]$  hydrogenases protein scaffold to insert asymmetrical cofactors into the active site with directional control opens the door to the development of a new class of semi-artificial enzymes. The biosynthesis of an asymmetric cofactor, despite being the normality for  $[\text{NiFe}]$  hydrogenases, to the best of my knowledge appears to be out of reach for the  $[\text{FeFe}]$  hydrogenases' maturation machinery. Studying  $[\text{FeFe}]$  hydrogenases variants matured with asymmetric cofactors arguably represents a way to sample a chemical space precluded to natural evolution and could therefore lead to the embetterment of these already extraordinary enzymes.

# Popular Science Summary

In the next decades, humanity will be facing the huge challenge of freeing itself from the dependence on fossil fuels in order to limit the impact that climate change will have on our planet and on our society.

Hydrogen gas ( $H_2$ ) can be a precious ally in this fight, as its physical and chemical properties make it particularly adapt for storing the energy produced with intermittent renewable sources (such as solar and wind power) and to be used as clean on-demand fuel. Indeed,  $H_2$  combustion with oxygen only results in the release of water in the environment and, contrary to the combustion of fossil fuels, does not contribute to the rise of carbon dioxide levels in the atmosphere. Moreover,  $H_2$  is a very useful chemical for many important industrial applications, ranging from the production of agricultural fertilizer to steel manufacturing

Sadly, the currently available  $H_2$  production methods do not let this gas uphold its promise of a greener future. More than 99% of  $H_2$  produced globally every year is either directly derived from fossil fuels, using processes that do release carbon dioxide in the atmosphere, or it is obtained as a side product of oil industry.

The only “clean” way we that is employed on industrial scale to produce  $H_2$  is water electrolysis, a process that uses electricity to break water molecules into  $H_2$  and oxygen. This process is very energy-demanding though, therefore we need special materials or molecules called “catalysts” to help the reaction happen more quickly and with a lower energy expenditure. At the moment, the only reliable catalysts available are based on rare and expensive metals like platinum, so if we want to use water electrolysis on a large scale and in an economically viable way we need to develop catalysts based on cheaper and more abundant elements.

As it is often the case Nature lent us a helping hand, at least for solving the problem for hydrogen evolution, by creating extremely efficient catalysts based on iron: [FeFe] hydrogenases.

[FeFe] hydrogenases are ancient enzymes that help many different organisms in satisfying their needs in terms of  $H_2$  metabolism. They are fascinating small machines that perform their task at incredible speeds, with a single molecule of [FeFe] hydrogenase being able to produce up to 20 000 molecules of  $H_2$  per second. Moreover, their ability to functions under conditions that are mild and compatible with biological life makes them really interesting for the

developing of systems that are robust and easy to maintain. There is major drawback for these enzymes though: they are completely and irreversibly deactivated by molecular oxygen. And oxygen is, well... everywhere.

A lot of research is focused on understanding the exact mechanism by which [FeFe] hydrogenases function, and on trying to overcome their oxygen-sensitivity by shielding them from oxygen damage or by designing intrinsically oxygen-resistant variants.

My thesis is trying to contribute to this endeavour in three different ways.

The first way is by investigating [FeFe] hydrogenases' mechanism and stability inside a living cell, in contrast to canonical approaches that study these enzymes in a test tube. This strategy appears very promising for reaching a model of the catalytic cycle that is physiologically relevant. Furthermore, keeping these enzymes inside a cellular envelope is one of the possible strategies to protect them from oxygen damage.

The second way is to come up with strategies to study and develop systems that drive the H<sub>2</sub>-production process using energy from light – an approach known as semi-artificial photosynthesis – while taking advantage of the oxygen protection granted by the cellular environment.

The third and final way is to study enzyme variants obtained with the help of synthetic chemistry, aiming at understanding how their structural and chemical characteristics influence the enzymes' various properties (like their catalytic proficiency or their susceptibility to inhibitors). This has the potential to lead to the future development of semi-artificial hydrogenases that are optimized not for Nature's needs, but for ours.

# Populärvetenskaplig Sammanfatning

Under de kommande årtiondena kommer mänskligheten att stå inför den enorma utmaningen att frigöra sig från beroendet av fossila bränslen för att begränsa klimatförändringarnas inverkan på vår planet och vårt samhälle.

Vätgas ( $H_2$ ) kan vara en värdefull allierad i denna kamp, eftersom dess fysikaliska och kemiska egenskaper gör den särskilt lämplig för att lagra energi från intermittenta förnybara källor (t.ex. sol- och vindkraft) och för att användas som ett rent bränsle vid behov. Förbränning av  $H_2$  med syre leder bara till att vatten släpps ut i miljön och bidrar, till skillnad från förbränning av fossila bränslen, inte till att öka koldioxidhalterna i atmosfären.  $H_2$  är dessutom en mycket användbar kemikalie för många viktiga industriella tillämpningar, från produktion av jordbruksgrödor till ståltillverkning.

Tyvärr är det så att de nuvarande  $H_2$ -tillverkningsmetoderna inte gör det möjligt för denna gas att uppfylla sitt löfte om en grönare framtid. Mer än 99 % av den  $H_2$  som produceras globalt varje år kommer antingen direkt från fossila bränslen med hjälp av processer som släpper ut koldioxid i atmosfären, eller så erhålls den som en biprodukt från oljeindustrin.

Det enda "rena" sätt som används idag för att producera  $H_2$  är vattenelektrolys, en process där elektricitet används för att bryta vattenmolekyler till  $H_2$  och syrgas. Denna process är dock mycket energislukande, och därför behöver vi särskilda material eller molekyler som kallas "katalysatorer" för att reaktionen ska kunna ske snabbare och med lägre energiåtgång. För närvarande är de enda tillförlitliga katalysatorer som finns tillgängliga baserade på sällsynta och dyra metaller som platina, så om vi vill använda vattenelektrolys i stor skala och på ett ekonomiskt hållbart sätt måste vi utveckla katalysatorer baserade på billigare och vanligare grundämnen.

Som ofta är fallet har evolutionen redan hittat en lösning på problemet genom att skapa extremt effektiva katalysatorer baserade på järn: [FeFe]-hydrogenaser.

[FeFe]-hydrogenaser är urgamla enzymer som hjälper många olika organismer att tillgodose sina behov av  $H_2$ -metabolism. De är fascinerande små maskiner som utför sin uppgift i otroliga hastigheter, där en enda molekyl av [FeFe]-hydrogenas kan producera upp till 20 000  $H_2$ -molekyler per sekund. Deras förmåga att fungera under förhållanden som är milda och förenliga med biologiskt liv gör dem dessutom mycket intressanta för att utveckla system som är robusta och lätta att underhålla. Det finns dock en stor nackdel med

enzymerna: de inaktiveras fullständigt och irreversibelt av molekylärt syre. Och syre finns, ja... överallt.

Mycket forskning är inriktad på att förstå den exakta mekanism genom vilken [FeFe]-hydrogenaser fungerar, och på att försöka övervinna deras syrekänslighet genom att skydda dem från syre-skador eller genom att konstruera syre-resistenta varianter.

Min avhandling försöker bidra till denna strävan på tre olika sätt.

Det första sättet är att undersöka [FeFe]-hydrogenasers mekanism och stabilitet i en levande cell, i motsats till klassiska metoder som studerar dessa enzymer efter ett reningssteg. Denna strategi verkar mycket lovande för att nå en modell av den katalytiska cykeln som är fysiologiskt relevant. Att hålla dessa enzymer inuti ett cellhölje är dessutom en av de möjliga strategierna för att skydda dem från syre-skador.

Det andra sättet är att hitta strategier för att studera och utveckla system som driver H<sub>2</sub>-produktionsprocessen med hjälp av ljusenergi - ett tillvägagångssätt som kallas semi-artificiell fotosyntes - samtidigt som man drar nytta av det syreskydd som cellmiljön ger.

Det tredje och sista sättet är att studera enzymvarianter som framställts med hjälp av syntetisk kemi, i syfte att förstå hur deras strukturella och kemiska egenskaper påverkar enzymernas olika egenskaper (t.ex. deras katalytiska förmåga eller deras känslighet för hämmare). Detta har potential att leda till framtida utveckling av halvkonstgjorda hydrogenaser som är optimerade inte för naturens behov, utan för våra.

## Riassunto divulgativo

Nei prossimi decenni, l'umanità dovrà affrontare l'enorme sfida di liberarsi dalla dipendenza dai combustibili fossili per limitare l'impatto che il cambiamento climatico avrà sul nostro pianeta e sulla nostra società.

L'idrogeno ( $H_2$ ) può essere un prezioso alleato in questa lotta, poiché le sue proprietà fisiche e chimiche lo rendono particolarmente adatto ad immagazzinare l'energia prodotta con fonti rinnovabili intermittenti (come l'energia solare ed eolica) e ad essere utilizzato come carburante pulito. Infatti la combustione dell' $H_2$  con l'ossigeno provoca solo il rilascio di acqua nell'ambiente e, contrariamente a quanto avviene con l'utilizzo dei combustibili fossili, non contribuisce all'aumento dei livelli di anidride carbonica nell'atmosfera; inoltre l'idrogeno è una sostanza chimica che trova uso in molte importanti applicazioni industriali, che vanno dalla produzione di fertilizzanti agricoli a quella dell'acciaio.

Purtroppo, i metodi per produrre  $H_2$  attualmente disponibili non permettono a questo gas di mantenere la sua promessa di un futuro più verde. Più del 99% dell' $H_2$  prodotto globalmente ogni anno è prodotto a partire da combustibili fossili, usando processi che rilasciano anidride carbonica nell'atmosfera, o è ottenuto come prodotto secondario dell'industria petrolifera.

L'unico modo "pulito" che conosciamo per produrre  $H_2$  è l'elettrolisi dell'acqua, un processo che usa l'elettricità per rompere le molecole d'acqua in  $H_2$  e ossigeno. Questo processo richiede però molta energia, e abbiamo quindi bisogno di materiali o molecole speciali chiamate "catalizzatori" per permettere a questa reazione di avvenire più rapidamente e con un minor dispendio energetico. Al momento, gli unici catalizzatori affidabili che abbiamo a disposizione sono basati su metalli rari e costosi come il platino. Quindi, se vogliamo usare l'elettrolisi dell'acqua su larga scala e in modo economicamente sostenibile abbiamo bisogno di sviluppare catalizzatori basati su elementi più economici ed abbondanti.

Come spesso accade, la Natura ci ha dato una mano per trovare una soluzione al problema, quantomeno riguardo la produzione di idrogeno, creando catalizzatori estremamente efficienti basati sul ferro: le [FeFe] idrogenasi.

Le [FeFe] idrogenasi sono enzimi primordiali che aiutano molti organismi diversi a soddisfare i loro bisogni in termini di metabolismo dell' $H_2$ . Sono piccole macchine biologiche molto affascinanti che svolgono il loro compito a

velocità incredibili, con una singola molecola di [FeFe] idrogenasi in grado di produrre fino a 20 000 molecole di  $H_2$  al secondo. Inoltre la loro capacità di funzionare in condizioni neutre e compatibili con la vita biologica li rende estremamente interessanti per lo sviluppo di sistemi robusti e di facile mantenimento. C'è però un grosso svantaggio legato a questi enzimi: l'esposizione all'ossigeno li danneggia e disattiva in modo irreparabile. E l'ossigeno è, beh... ovunque.

La ricerca si sta concentrando sulla comprensione dell'esatto meccanismo con cui le [FeFe] idrogenasi funzionano, con anche l'obiettivo di superare la loro sensibilità all'ossigeno; o in qualche modo schermandole dall'esposizione o progettando varianti intrinsecamente resistenti all'ossigeno.

La mia tesi cerca di contribuire a questo sforzo in tre modi diversi.

Il primo modo è investigando il meccanismo enzimatico e la stabilità delle [FeFe] idrogenasi all'interno di una cellula vivente, contrariamente agli approcci canonici che studiano questi enzimi solo in seguito ad una fase di purificazione. Questa strategia sembra molto promettente per sviluppare un modello del ciclo catalitico che sia fisiologicamente rilevante. Inoltre, mantenere questi enzimi all'interno di un involucro cellulare è una delle possibili strategie che possono essere applicate per proteggerli dall'inattivazione causata dall'ossigeno.

Il secondo modo è proponendo strategie utili a studiare e sviluppare sistemi che portino avanti il processo di produzione di  $H_2$  usando l'energia luminosa - un approccio conosciuto come fotosintesi semi-artificiale - approfittando al contempo della protezione dall'ossigeno garantita dall'ambiente cellulare.

Il terzo e ultimo modo è studiando varianti enzimatiche ottenute con l'aiuto della chimica sintetica, con l'obiettivo di capire come le caratteristiche strutturali e chimiche influenzino le proprietà degli enzimi stessi (come la loro efficienza catalitica o la loro sensibilità nei confronti degli inibitori). Questo campo di ricerca può potenzialmente portare al futuro sviluppo di idrogenasi semi-artificiali, che siano ottimizzate non per i bisogni della Natura, ma per i nostri.

# Acknowledgments

As the story of René Descartes teaches us, you cannot expect to last more than a few months in Sweden without some love and support from people around you.

Having survived for more than four years, I think I might have receive some of both and there are people I need to thank for that.

I think my supervisor, **Prof. Gustav Berggren**, deserves the first spot in this list. You took me under your wing four and a half years ago and got me to this point. There are no words to express my gratitude. You have been (very) patient and helpful all throught this journey. Thank you.

Special thanks go also to **Dr. Livia Mészáros**. You have been a reliable guide as I moved my first step into this field and you taught me most of what I know. I owe you a lot.

Thanks to **Prof. Johannes Messinger**, for being as patient (maybe even more patient) with me as Gustav, and for having pushed me to always do more and do better.

Thanks to **Prof. Stenbjörn Styring**, I still remember the first chat we had and the great impression you had on me. We miss you in the department.

Thanks to **Fikret Mamedov** and **Ping Huang**, for having made me into a decent (I hope) EPR spectroscopist.

Thanks to **Moritz Senger**, for having taught me that there is more to spectroscopy than just EPR.

Thanks to all the members of the BBC group, past and present: **Mira Gamache**, **Henrik Land**, **Pierre Ceccaldi**, **Casper De Lichtenberg** (I will never forget your laugh and you energy) **Sergii Shylin**, **Brigitta Németh**, **Marcus Lundberg**, **Nessima Salhi**, **Felix Ho**, **Ann Magnuson**, **Michael Cheah** (there should be one in every lab), **Fatemeh Khosravitabar**, **Petko Chernev**, **Alina Sekretareva**, **Sagar Ganguli**, **Shipra Prakash** and **Long Vo Pham**. You people make up a great team! Keep it up!



Thanks to the “PhDini”: **Holly, Princess** and **Afridi**. The hydrogenases brats. It was nice to share this adventure with you.

Thank to the (more or less) new generation: **Claudia Spallacci, Orkun Aydin, Nicholas Croy, Ziwen Zhao, Maximilian Böhm** and **Sofie Ye**. If I managed to get to this point, I am sure you guys will breeze through your PhDs.

Thanks to **Manuel**, for uphold the honour of Italian Latin Lovers. I just want to make clear that I never fell for your charme. Despite what you insinuated in your acknowledgments, to me you are just a friend.

Thanks to Don **Michele “Biden” Bedin**, and Don **Luca D’Amario**. Baciamo le mani. Your friendship and your characters made me feel a bit more at home.

Thank to **João “J-Wow” Rodrigues**, for having been my gym mate, my MtG mate, my beers mate, my One Piece mate... basically for having been my mate.-

Thanks to **Prof. Peter Lindblad, Pia, Karin, Kate, Matina, Amit, Hao, Claudia, Henna** and all of the other cyanos, old and new. Your big office has always felt like home, even though you never gave me the desk that was rightfully mine.

Thanks to **Prof. Leif Hammarström** (or Hammerstorm, which sounds even better), **Prof. Sascha Ott, Starla, Sigrid, Astrid, Belinda, Martin, Ashleigh, Nicholas, Salauat, Andrea** and all of the **SMC** and **Fyskem** people. You are all great people and have been great lab-neighbors.

Thanks to **Mariia**, for putting up with me as a collaborator and for always being so sweet. It was a pleasure and an honor to help you.

Thanks to the “night club”: **Nidhi, Aijie, Yocifu** and **Andela**. It was nice to know you could always find someone in the department to have a chat with, regardless of the time of the night.

Thanks to those who were unlucky enough to be my students: **Karina** and **Chloé**. I hope I managed to teach something to you! I sure learnt a lot during my time as your tutor.

Thanks to TestaCenter, in particular to **Jasper, Adam, Erik** and **Charlotte**. Thank you for the opportunity, for the help and for the great time.

Thanks to **Iê Capoeira Uppsala**, for welcoming this weird Italian guy that refuses to speak Swedish and for making him find out that he's not the walrus he thought. And that he can play a tamburine.

Grazie alla mia famiglia, **Monica**, **Roberto** e mio fratello, quello bello dei due, **Mauro**. Nonostante la distanza vi ho sempre sentiti vicini, e sono contento di tornare finalmente a casa.

Infine, grazie a **Stephanie**. Grazie della pazienza. Grazie per esserci stata sempre. Sei oggi piú che mai il faro la cui luce illumina il mio cammino, e senza di te io non sono nulla.

# References

1. R. Moradi and K. M. Groth, *Int. J. Hydrogen Energy*, 2019, **44**, 12254-12269.
2. IEA, 2021.
3. A. Abdulla, R. Hanna, K. R. Schell, O. Babacan and D. G. Victor, *Environmental Research Letters*, 2020, **16**, 014036.
4. IPCC, 2013.
5. A. J. Turner, C. Frankenberg and E. A. Kort, *Proc. Natl. Acad. Sci. U.S.A.*, 2019, **116**, 2805-2813.
6. G. Ertl, *Catalysis Reviews*, 1980, **21**, 201-223.
7. C. Smith, A. K. Hill and L. Torrente-Murciano, *Energy Environ. Sci.*, 2020, **13**, 331-344.
8. P. H. Pfromm, *Journal of Renewable and Sustainable Energy*, 2017, **9**, 034702.
9. R. Ramachandran and R. K. Menon, *Int. J. Hydrogen Energy*, 1998, **23**, 593-598.
10. P. Mäki-Arvela, T. A. Kaka khel, M. Azkaar, S. Engblom and D. Y. Murzin, *Catalysts*, 2018, **8**, 534.
11. F. Patisson and O. Mirgaux, *Metals*, 2020, **10**, 922.
12. L. García, in *Compendium of Hydrogen Energy*, eds. V. Subramani, A. Basile and T. N. Veziroğlu, Woodhead Publishing, Oxford, 2015, DOI: <https://doi.org/10.1016/B978-1-78242-361-4.00004-2>, pp. 83-107.
13. G. Franchi, M. Capocelli, M. De Falco, V. Piemonte and D. Barba, *Membranes (Basel)*, 2020, **10**, 10.
14. M. Steinberg, *Int. J. Hydrogen Energy*, 1999, **24**, 771-777.
15. J. G. Speight, in *Natural Gas (Second Edition)*, ed. J. G. Speight, Gulf Professional Publishing, Boston, 2019, DOI: <https://doi.org/10.1016/B978-0-12-809570-6.00006-0>, pp. 189-218.
16. N. J. Wagner, M. Coertzen, R. H. Matjie and J. C. van Dyk, in *Applied Coal Petrology*, eds. I. Suárez-Ruiz and J. C. Crelling, Elsevier, Burlington, 2008, DOI: <https://doi.org/10.1016/B978-0-08-045051-3.00005-1>, pp. 119-144.
17. A. Abánades, in *Production of Hydrogen from Renewable Resources*, eds. Z. Fang, J. R. L. Smith and X. Qi, Springer Netherlands, Dordrecht, 2015, DOI: 10.1007/978-94-017-7330-0\_6, pp. 149-177.

18. N. Sánchez-Bastardo, R. Schlögl and H. Ruland, *Industrial & Engineering Chemistry Research*, 2021, **60**, 11855-11881.
19. U. P. M. Ashik, W. M. A. Wan Daud and H. F. Abbas, *Renewable and Sustainable Energy Reviews*, 2015, **44**, 221-256.
20. A. Ursua, L. M. Gandia and P. Sanchis, *Proceedings of the IEEE*, 2012, **100**, 410-426.
21. V. F. Valdés-López, T. Mason, P. R. Shearing and D. J. L. Brett, *Progress in Energy and Combustion Science*, 2020, **79**, 100842.
22. B. M. Besancon, V. Hasanov, R. Imbault-Lastapis, R. Benesch, M. Barrio and M. J. Mølnvik, *Int. J. Hydrogen Energy*, 2009, **34**, 2350-2360.
23. S. Shiva Kumar and V. Himabindu, *Materials Science for Energy Technologies*, 2019, **2**, 442-454.
24. B. Zhang, L. Fan, R. B. Ambre, T. Liu, Q. Meng, B. J. J. Timmer and L. Sun, *Joule*, 2020, **4**, 1408-1444.
25. C. Madden, M. D. Vaughn, I. Díez-Pérez, K. A. Brown, P. W. King, D. Gust, A. L. Moore and T. A. Moore, *J. Am. Chem. Soc.*, 2012, **134**, 1577-1582.
26. W. Lubitz, E. Reijerse and M. van Gastel, *Chem. Rev.*, 2007, **107**, 4331-4365.
27. D. W. Mulder, D. O. Ortillo, D. J. Gardenghi, A. V. Naumov, S. S. Ruebush, R. K. Szilagyi, B. Huynh, J. B. Broderick and J. W. Peters, *Biochem.*, 2009, **48**, 6240-6248.
28. G. Berggren, A. Adamska, C. Lambertz, T. R. Simmons, J. Esselborn, M. Atta, S. Gambarelli, J. M. Mouesca, E. Reijerse, W. Lubitz, T. Happe, V. Artero and M. Fontecave, *Nature*, 2013, **499**, 66-69.
29. A. Silakov, C. Kamp, E. Reijerse, T. Happe and W. Lubitz, *Biochem.*, 2009, **48**, 7780-7786.
30. H. Land, A. Sekretareva, P. Huang, H. J. Redman, B. Németh, N. Polidori, L. S. Mészáros, M. Senger, S. T. Stripp and G. Berggren, *Chem. Sci.*, 2020, **11**, 12789-12801.
31. M. Winkler, J. Esselborn and T. Happe, *Biochim. Biophys. Acta, Bioenerg.*, 2013, **1827**, 974-985.
32. David W. Mulder, Eric M. Shepard, Jonathan E. Meuser, N. Joshi, Paul W. King, Matthew C. Posewitz, Joan B. Broderick and John W. Peters, *Structure*, 2011, **19**, 1038-1052.
33. A. J. Cornish, K. Gärtner, H. Yang, J. W. Peters and E. L. Hegg, *J. Biol. Chem.*, 2011, **286**, 38341-38347.
34. A. J. Cornish, B. Ginovska, A. Thelen, J. C. S. da Silva, T. A. Soares, S. Raugei, M. Dupuis, W. J. Shaw and E. L. Hegg, *Biochem.*, 2016, **55**, 3165-3173.
35. S. Morra, A. Giraudo, G. Di Nardo, P. W. King, G. Gilardi and F. Valetti, *PLOS ONE*, 2012, **7**, e48400.

36. J. Duan, M. Senger, J. Esselborn, V. Engelbrecht, F. Wittkamp, U.-P. Apfel, E. Hofmann, S. T. Stripp, T. Happe and M. Winkler, *Nat. Commun.*, 2018, **9**, 4726.
37. M. Senger, V. Eichmann, K. Laun, J. Duan, F. Wittkamp, G. Knör, U.-P. Apfel, T. Happe, M. Winkler, J. Heberle and S. T. Stripp, *J. Am. Chem. Soc.*, 2019, **141**, 17394-17403.
38. J. Meyer, *Cell. Mol. Life Sci.*, 2007, **64**, 1063-1084.
39. H. Land, M. Senger, G. Berggren and S. T. Stripp, *ACS Catal.*, 2020, **10**, 7069-7086.
40. C. Gauquelin, C. Baffert, P. Richaud, E. Kamionka, E. Etienne, D. Guieysse, L. Girbal, V. Fourmond, I. André, B. Guigliarelli, C. Léger, P. Soucaille and I. Meynial-Salles, *Biochim. Biophys. Acta, Bioenerg.*, 2018, **1859**, 69-77.
41. G. Caserta, C. Papini, A. Adamska-Venkatesh, L. Pecqueur, C. Sommer, E. Reijerse, W. Lubitz, C. Gauquelin, I. Meynial-Salles, D. Pramanik, V. Artero, M. Atta, M. del Barrio, B. Faivre, V. Fourmond, C. Léger and M. Fontecave, *J. Am. Chem. Soc.*, 2018, **140**, 5516-5526.
42. P. Rodríguez-Maciá, K. Pawlak, O. Rüdiger, E. J. Reijerse, W. Lubitz and J. A. Birrell, *J. Am. Chem. Soc.*, 2017, **139**, 15122-15134.
43. A. Kubas, C. Orain, D. De Sancho, L. Saujet, M. Sensi, C. Gauquelin, I. Meynial-Salles, P. Soucaille, H. Bottin, C. Baffert, V. Fourmond, R. B. Best, J. Blumberger and C. Léger, *Nat. Chem.*, 2016, **9**, 88-95.
44. J. Cohen, K. Kim, P. King, M. Seibert and K. Schulten, *Structure*, 2005, **13**, 1321-1329.
45. T. Lautier, P. Ezanno, C. Baffert, V. Fourmond, L. Cournac, J. C. Fontecilla-Camps, P. Soucaille, P. Bertrand, I. Meynial-Salles and C. Léger, *Faraday Discuss*, 2011, **148**, 385-407.
46. J. Esselborn, N. Muraki, K. Klein, V. Engelbrecht, N. Metzler-Nolte, U. P. Apfel, E. Hofmann, G. Kurisu and T. Happe, *Chem. Sci.*, 2016, **7**, 959-968.
47. M. Lorenzi and G. Berggren, in *Comprehensive Coordination Chemistry III*, eds. E. C. Constable, G. Parkin and L. Que Jr, Elsevier, Oxford, 2021, DOI: <https://doi.org/10.1016/B978-0-08-102688-5.00081-7>, pp. 731-756.
48. D. L. M. Suess, J. M. Kuchenreuther, L. De La Paz, J. R. Swartz and R. D. Britt, *Inorg. Chem.*, 2016, **55**, 478-487.
49. G. Rao, L. Tao and R. D. Britt, *Chem. Sci.*, 2020, **11**, 1241-1247.
50. J. N. Betz, N. W. Boswell, C. J. Fugate, G. L. Holliday, E. Akiva, A. G. Scott, P. C. Babbitt, J. W. Peters, E. M. Shepard and J. B. Broderick, *Biochem.*, 2015, **54**, 1807-1818.

51. R. Rohac, P. Amara, A. Benjdia, L. Martin, P. Ruffié, A. Favier, O. Berteau, J. M. Mouesca, J. C. Fontecilla-Camps and Y. Nicolet, *Nat Chem*, 2016, **8**, 491-500.
52. B. Németh, M. Senger, H. J. Redman, P. Ceccaldi, J. Broderick, A. Magnuson, S. T. Stripp, M. Haumann and G. Berggren, *J. Biol. Inorg. Chem.*, 2020, **25**, 777-788.
53. B. Németh, H. Land, A. Magnuson, A. Hofer and G. Berggren, *J. Biol. Chem.*, 2020, **295**, 11891-11901.
54. J. Esselborn, C. Lambertz, A. Adamska-Venkatesh, T. Simmons, G. Berggren, J. Noth, J. Siebel, A. Hemschemeier, V. Artero, E. Reijerse, M. Fontecave, W. Lubitz and T. Happe, *Nat. Chem. Biol.*, 2013, **9**, 607-609.
55. J. F. Siebel, A. Adamska-Venkatesh, K. Weber, S. Rumpel, E. Reijerse and W. Lubitz, *Biochem.*, 2015, **54**, 1474-1483.
56. W. Lubitz, H. Ogata, O. Rudiger and E. Reijerse, *Chem. Rev.*, 2014, **114**, 4081-4148.
57. J. W. Peters, G. J. Schut, E. S. Boyd, D. W. Mulder, E. M. Shepard, J. B. Broderick, P. W. King and M. W. Adams, *Biochim Biophys Acta*, 2015, **1853**, 1350-1369.
58. H. S. Shafaat, O. Rüdiger, H. Ogata and W. Lubitz, *Biochim. Biophys. Acta, Bioenerg.*, 2013, **1827**, 986-1002.
59. J. W. Peters, G. J. Schut, E. S. Boyd, D. W. Mulder, E. M. Shepard, J. B. Broderick, P. W. King and M. W. W. Adams, *Biochimica et Biophysica Acta (BBA) - Molecular Cell Research*, 2015, **1853**, 1350-1369.
60. C. Baffert, A. Kpebe, L. Avilan and M. Brugna, in *Advances in Microbial Physiology*, ed. R. K. Poole, Academic Press, 2019, vol. 74, pp. 143-189.
61. J. T. Henry and S. Crosson, *Annu Rev Microbiol*, 2011, **65**, 261-286.
62. N. Chongdar, J. A. Birrell, K. Pawlak, C. Sommer, E. J. Reijerse, O. Rudiger, W. Lubitz and H. Ogata, *J Am Chem Soc*, 2018, **140**, 1057-1068.
63. O. Lampret, A. Adamska-Venkatesh, H. Konegger, F. Wittkamp, U.-P. Apfel, E. J. Reijerse, W. Lubitz, O. Rüdiger, T. Happe and M. Winkler, *J. Am. Chem. Soc.*, 2017, **139**, 18222-18230.
64. L. Kertess, A. Adamska-Venkatesh, P. Rodriguez-Macia, O. Rudiger, W. Lubitz and T. Happe, *Chem Sci*, 2017, **8**, 8127-8137.
65. J. H. Artz, O. A. Zadornyy, D. W. Mulder, S. M. Keable, A. E. Cohen, M. W. Ratzloff, S. G. Williams, B. Ginovska, N. Kumar, J. Song, S. E. McPhillips, C. M. Davidson, A. Y. Lyubimov, N. Pence, G. J. Schut, A. K. Jones, S. M. Soltis, M. W. W. Adams, S. Raugei, P. W. King and J. W. Peters, *J. Am. Chem. Soc.*, 2020, **142**, 1227-1235.
66. W. K. Myers, T. A. Stich, D. L. M. Suess, J. M. Kuchenreuther, J. R. Swartz and R. D. Britt, *J. Am. Chem. Soc.*, 2014, **136**, 12237-12240.

67. C. Sommer, A. Adamska-Venkatesh, K. Pawlak, J. A. Birrell, O. Rüdiger, E. J. Reijerse and W. Lubitz, *J. Am. Chem. Soc.*, 2017, **139**, 1440-1443.
68. Y. Nicolet, A. L. de Lacey, X. Vernède, V. M. Fernandez, E. C. Hatchikian and J. C. Fontecilla-Camps, *J. Am. Chem. Soc.*, 2001, **123**, 1596-1601.
69. C. Lorent, S. Katz, J. Duan, C. J. Kulka, G. Caserta, C. Teutloff, S. Yadav, U.-P. Apfel, M. Winkler, T. Happe, M. Horch and I. Zebger, *J. Am. Chem. Soc.*, 2020, **142**, 5493-5497.
70. M. W. Ratzloff, J. H. Artz, D. W. Mulder, R. T. Collins, T. E. Furtak and P. W. King, *J. Am. Chem. Soc.*, 2018, DOI: 10.1021/jacs.8b03072.
71. J. A. Birrell, V. Pelmeshnikov, N. Mishra, H. Wang, Y. Yoda, K. Tamasaku, T. B. Rauchfuss, S. P. Cramer, W. Lubitz and S. DeBeer, *J. Am. Chem. Soc.*, 2020, **142**, 222-232.
72. M. Winkler, M. Senger, J. Duan, J. Esselborn, F. Wittkamp, E. Hofmann, U.-P. Apfel, S. T. Stripp and T. Happe, *Nat. Commun.*, 2017, **8**, 16115.
73. S. Rumpel, C. Sommer, E. Reijerse, C. Farès and W. Lubitz, *J. Am. Chem. Soc.*, 2018, DOI: 10.1021/jacs.8b00459.
74. D. W. Mulder, Y. Guo, M. W. Ratzloff and P. W. King, *J. Am. Chem. Soc.*, 2017, **139**, 83-86.
75. E. J. Reijerse, C. C. Pham, V. Pelmeshnikov, R. Gilbert-Wilson, A. Adamska-Venkatesh, J. F. Siebel, L. B. Gee, Y. Yoda, K. Tamasaku, W. Lubitz, T. B. Rauchfuss and S. P. Cramer, *J. Am. Chem. Soc.*, 2017, **139**, 4306-4309.
76. D. W. Mulder, M. W. Ratzloff, M. Bruschi, C. Greco, E. Koonce, J. W. Peters and P. W. King, *J. Am. Chem. Soc.*, 2014, **136**, 15394-15402.
77. D. S. Patil, J. J. Moura, S. H. He, M. Teixeira, B. C. Prickril, D. V. DerVartanian, H. D. Peck, J. LeGall and B. H. Huynh, *J. Biol. Chem.*, 1988, **263**, 18732-18738.
78. S. P. J. Albracht, W. Roseboom and E. C. Hatchikian, *J. Biol. Inorg. Chem.*, 2006, **11**, 88-101.
79. P. Rodríguez-Maciá, E. J. Reijerse, M. van Gastel, S. DeBeer, W. Lubitz, O. Rüdiger and J. A. Birrell, *J. Am. Chem. Soc.*, 2018, **140**, 9346-9350.
80. P. Rodríguez-Maciá, L. M. Galle, R. Bjornsson, C. Lorent, I. Zebger, Y. Yoda, S. P. Cramer, S. DeBeer, I. Span and J. A. Birrell, *Angew. Chem. Int. Ed.*, 2020, **59**, 16786-16794.
81. S. Morra, M. Arizzi, F. Valetti and G. Gilardi, *Biochem.*, 2016, **55**, 5897-5900.
82. P. S. Corrigan, J. L. Tirsch and A. Silakov, *J. Am. Chem. Soc.*, 2020, **142**, 12409-12419.

83. M. Winkler, J. Duan, A. Rutz, C. Felbek, L. Scholtysek, O. Lampret, J. Jaenecke, U.-P. Apfel, G. Gilardi, F. Valetti, V. Fourmond, E. Hofmann, C. Léger and T. Happe, *Nat. Commun.*, 2021, **12**, 756.
84. A. Adamska-Venkatesh, D. Krawietz, J. Siebel, K. Weber, T. Happe, E. Reijerse and W. Lubitz, *J. Am. Chem. Soc.*, 2014, **136**, 11339-11346.
85. G. Goldet, C. Brandmayr, S. T. Stripp, T. Happe, C. Cavazza, J. C. Fontecilla-Camps and F. A. Armstrong, *J. Am. Chem. Soc.*, 2009, **131**, 14979-14989.
86. M. L. K. Sanchez, C. Sommer, E. Reijerse, J. A. Birrell, W. Lubitz and R. B. Dyer, *J. Am. Chem. Soc.*, 2019, **141**, 16064-16070.
87. P. Chernev, C. Lambertz, A. Brünje, N. Leidel, K. G. V. Sigfridsson, R. Kositzki, C.-H. Hsieh, S. Yao, R. Schiwon, M. Driess, C. Limberg, T. Happe and M. Haumann, *Inorg. Chem.*, 2014, **53**, 12164-12177.
88. S. Mebs, M. Senger, J. Duan, F. Wittkamp, U.-P. Apfel, T. Happe, M. Winkler, S. T. Stripp and M. Haumann, *J. Am. Chem. Soc.*, 2017, **139**, 12157-12160.
89. S. Mebs, J. Duan, F. Wittkamp, S. T. Stripp, T. Happe, U.-P. Apfel, M. Winkler and M. Haumann, *Inorg. Chem.*, 2019, **58**, 4000-4013.
90. A. R. Finkelmann, M. T. Stiebritz and M. Reiher, *Chem. Sci.*, 2014, **5**, 215-221.
91. M. Haumann and S. T. Stripp, *Accounts of Chemical Research*, 2018, **51**, 1755-1763.
92. O. Lampret, J. Duan, E. Hofmann, M. Winkler, F. A. Armstrong and T. Happe, *Proc. Natl. Acad. Sci. U.S.A.*, 2020, **117**, 20520-20529.
93. S. B. Zimmerman and S. O. Trach, *Journal of Molecular Biology*, 1991, **222**, 599-620.
94. R. J. Ellis, *Trends in Biochemical Sciences*, 2001, **26**, 597-604.
95. R. J. Ellis, *Current Opinion in Structural Biology*, 2001, **11**, 114-119.
96. G. B. Ralston, *Journal of Chemical Education*, 1990, **67**, 857.
97. M. Mourão, D. Kreitman and S. Schnell, *Phys. Chem. Chem. Phys.*, 2014, **16**, 4492-4503.
98. M. Senger, S. Mebs, J. Duan, O. Shulenina, K. Laun, L. Kertess, F. Wittkamp, U.-P. Apfel, T. Happe, M. Winkler, M. Haumann and S. T. Stripp, *Phys. Chem. Chem. Phys.*, 2018, **20**, 3128-3140.
99. M. Chalfie, Y. Tu, G. Euskirchen, W. W. Ward and D. C. Prasher, *Science*, 1994, **263**, 802-805.
100. D. Shrestha, A. Jenei, P. Nagy, G. Vereb and J. Szöllösi, *International Journal of Molecular Sciences*, 2015, **16**, 6718-6756.
101. E. Luchinat and L. Banci, *J. Biol. Chem.*, 2016, **291**, 3776-3784.
102. Z. Serber, R. Ledwidge, S. M. Miller and V. Dötsch, *J. Am. Chem. Soc.*, 2001, **123**, 8895-8901.



103. Z. Serber, W. Straub, L. Corsini, A. M. Nomura, N. Shimba, C. S. Craik, P. Ortiz de Montellano and V. Dötsch, *J Am Chem Soc*, 2004, **126**, 7119-7125.
104. C. Li, G.-F. Wang, Y. Wang, R. Creager-Allen, E. A. Lutz, H. Scronce, K. M. Slade, R. A. S. Ruf, R. A. Mehl and G. J. Pielak, *J. Am. Chem. Soc.*, 2010, **132**, 321-327.
105. R. Hänsel, S. Foldynová-Trantírková, F. Löhr, J. Buck, E. Bongartz, E. Bamberg, H. Schwalbe, V. Dötsch and L. Trantírek, *J. Am. Chem. Soc.*, 2009, **131**, 15761-15768.
106. S. Ogino, S. Kubo, R. Umemoto, S. Huang, N. Nishida and I. Shimada, *J. Am. Chem. Soc.*, 2009, **131**, 10834-10835.
107. A. Bonucci, O. Ouari, B. Guigliarelli, V. Belle and E. Mileo, *ChemBioChem*, 2020, **21**, 451-460.
108. R. Igarashi, T. Sakai, H. Hara, T. Tenno, T. Tanaka, H. Tochio and M. Shirakawa, *J. Am. Chem. Soc.*, 2010, **132**, 8228-8229.
109. M. J. Schmidt, J. Borbas, M. Drescher and D. Summerer, *J. Am. Chem. Soc.*, 2014, **136**, 1238-1241.
110. M. M. Haugland, J. E. Lovett and E. A. Anderson, *Chemical Society Reviews*, 2018, **47**, 668-680.
111. A. Martorana, G. Bellapadrona, A. Feintuch, E. Di Gregorio, S. Aime and D. Goldfarb, *J. Am. Chem. Soc.*, 2014, **136**, 13458-13465.
112. L. S. Meszaros, B. Nemeth, C. Esmieu, P. Ceccaldi and G. Berggren, *Angew. Chem. Int. Ed.*, 2018, **57**, 2596-2599.
113. Z. Dai and J. Nielsen, *Current Opinion in Biotechnology*, 2015, **36**, 8-15.
114. C. C. C. R. de Carvalho, *Microbial Biotechnology*, 2017, **10**, 250-263.
115. B. Lin and Y. Tao, *Microbial Cell Factories*, 2017, **16**, 106.
116. N. Ladkau, A. Schmid and B. Bühler, *Current Opinion in Biotechnology*, 2014, **30**, 178-189.
117. M. Jeschek, S. Panke and T. R. Ward, *Trends in Biotechnology*, 2018, **36**, 60-72.
118. A. G. Jarvis, *Curr. Opin. Chem. Biol.*, 2020, **58**, 63-71.
119. S. Chordia, S. Narasimhan, A. Lucini Paioni, M. Baldus and G. Roelfes, *Angew. Chem. Int. Ed.*, 2021, **60**, 5913-5920.
120. M. Jeschek, R. Reuter, T. Heinisch, C. Trindler, J. Klehr, S. Panke and T. R. Ward, *Nature*, 2016, **537**, 661-665.
121. I. Drienovská, L. Alonso-Cotchico, P. Vidossich, A. Lledós, J.-D. Maréchal and G. Roelfes, *Chem. Sci.*, 2017, **8**, 7228-7235.
122. K. J. Naughton, R. E. Treviño, P. J. Moore, A. E. Wertz, J. A. Dickson and H. S. Shafaat, *ACS Synthetic Biology*, 2021, **10**, 2116-2120.
123. S. Cestellos-Blanco, H. Zhang, J. M. Kim, Y.-x. Shen and P. Yang, *Nature Catalysis*, 2020, **3**, 245-255.

124. L. Schmermund, V. Jurkaš, F. F. Özgen, G. D. Barone, H. C. Büchsenschtz, C. K. Winkler, S. Schmidt, R. Kourist and W. Kroutil, *ACS Catal.*, 2019, **9**, 4115-4144.
125. H. Zhang, H. Liu, Z. Tian, D. Lu, Y. Yu, S. Cestellos-Blanco, K. K. Sakimoto and P. Yang, *Nature Nanotechnology*, 2018, **13**, 900-905.
126. J. Ye, J. Yu, Y. Zhang, M. Chen, X. Liu, S. Zhou and Z. He, *Applied Catalysis B: Environmental*, 2019, **257**, 117916.
127. J. H. Park, S. H. Lee, G. S. Cha, D. S. Choi, D. H. Nam, J. H. Lee, J. K. Lee, C. H. Yun, K. J. Jeong and C. B. Park, *Angew Chem Int Ed Engl*, 2015, **54**, 969-973.
128. S. F. Rowe, G. Le Gall, E. V. Ainsworth, J. A. Davies, C. W. J. Lockwood, L. Shi, A. Elliston, I. N. Roberts, K. W. Waldron, D. J. Richardson, T. A. Clarke, L. J. C. Jeuken, E. Reisner and J. N. Butt, *ACS Catal.*, 2017, **7**, 7558-7566.
129. Y. M. Wilson, M. Dürrenberger, E. S. Nogueira and T. R. Ward, *J. Am. Chem. Soc.*, 2014, **136**, 8928-8932.
130. N. Khanna, C. Esmieu, L. S. Mészáros, P. Lindblad and G. Berggren, *Energy Environ. Sci.*, 2017, **10**, 1563-1567.
131. A. Wegelius, N. Khanna, C. Esmieu, G. D. Barone, F. Pinto, P. Tamagnini, G. Berggren and P. Lindblad, *Energy Environ. Sci.*, 2018, **11**, 3163-3167.
132. U. Tokumoto and Y. Takahashi, *J Biochem*, 2001, **130**, 63-71.
133. C. Kamp, A. Silakov, M. Winkler, E. J. Reijerse, W. Lubitz and T. Happe, *Biochim. Biophys. Acta, Bioenerg.*, 2008, **1777**, 410-416.
134. L. Mészáros, P. Ceccaldi, M. Lorenzi, H. J. Redman, E. Pfitzner, J. Heberle, M. Senger, S. T. Stripp and G. Berggren, *Chem. Sci.*, 2020, DOI: 10.1039/D0SC00512F.
135. M. A. Martini, O. Rüdiger, N. Breuer, B. Nöring, S. DeBeer, P. Rodríguez-Maciá and J. A. Birrell, *J. Am. Chem. Soc.*, 2021, **143**, 18159-18171.
136. A. Sekowska, H. F. Kung and A. Danchin, *J Mol Microbiol Biotechnol*, 2000, **2**, 145-177.
137. K. Li, Y. Xin, G. Xuan, R. Zhao, H. Liu, Y. Xia and L. Xun, *Frontiers in Microbiology*, 2019, **10**.
138. M. Lorenzi, P. Ceccaldi, P. Rodríguez-Maciá, H. J. Redman, A. Zamader, J. A. Birrell, L. S. Mészáros and G. Berggren, *J. Biol. Inorg. Chem.*, 2022, DOI: 10.1007/s00775-022-01928-5.
139. W. Roseboom, A. L. De Lacey, V. M. Fernandez, E. C. Hatchikian and S. P. J. Albracht, *J. Biol. Inorg. Chem.*, 2006, **11**, 102-118.
140. M. Lempp, P. Lubrano, G. Bange and H. Link, *Biol. Chem.*, 2020, **401**, 1479-1485.
141. P. Knörzer, A. Silakov, C. E. Foster, F. A. Armstrong, W. Lubitz and T. Happe, *J. Biol. Chem.*, 2012, **287**, 1489-1499.

142. C. Felbek, F. Arrigoni, D. de Sancho, A. Jacq-Bailly, R. B. Best, V. Fourmond, L. Bertini and C. Léger, *ACS Catal.*, 2021, **11**, 15162-15176.
143. R. Leardi, *Analytica Chimica Acta*, 2009, **652**, 161-172.
144. Y. Honda, Y. Shinohara and H. Fujii, *Catalysis Science & Technology*, 2020, **10**, 6006-6012.
145. M. Sensi, C. Baffert, V. Fourmond, L. de Gioia, L. Bertini and C. Léger, *Sustain. Energy Fuels*, 2021, **5**, 4248-4260.
146. C. Sommer, C. P. Richers, W. Lubitz, T. B. Rauchfuss and E. J. Reijerse, *Angew. Chem. Int. Ed.*, 2018, **57**, 5429-5432.
147. L. Kertess, F. Wittkamp, C. Sommer, J. Esselborn, O. Rüdiger, E. J. Reijerse, E. Hofmann, W. Lubitz, M. Winkler, T. Happe and U. P. Apfel, *Dalton Trans.*, 2017, **46**, 16947-16958.
148. W. Wang, M. J. Nilges, T. B. Rauchfuss and M. Stein, *J. Am. Chem. Soc.*, 2013, **135**, 3633-3639.
149. M. Senger, S. Mebs, J. Duan, F. Wittkamp, U.-P. Apfel, J. Heberle, M. Haumann and S. T. Stripp, *Proc. Natl. Acad. Sci. U.S.A.*, 2016, **113**, 8454-8459.
150. O. Lampret, J. Esselborn, R. Haas, A. Rutz, R. L. Booth, L. Kertess, F. Wittkamp, C. F. Megarity, F. A. Armstrong, M. Winkler and T. Happe, *Proc. Natl. Acad. Sci. U.S.A.*, 2019, **116**, 15802-15810.
151. D. W. Mulder, E. S. Boyd, R. Sarma, R. K. Lange, J. A. Endrizzi, J. B. Broderick and J. W. Peters, *Nature*, 2010, **465**, 248-251.
152. J. A. Birrell, K. Wrede, K. Pawlak, P. Rodriguez-Maciá, O. Rüdiger, E. J. Reijerse and W. Lubitz, *Isr. J. Chem.*, 2016, **56**, 852-863.
153. V. Hajj, C. Baffert, K. Sybirna, I. Meynial-Salles, P. Soucaille, H. Bottin, V. Fourmond and C. Léger, *Energy Environ. Sci.*, 2014, **7**, 715-719.
154. V. Fourmond, C. Baffert, K. Sybirna, S. Dementin, A. Abou-Hamdan, I. Meynial-Salles, P. Soucaille, H. Bottin and C. Léger, *ChemComm*, 2013, **49**, 6840-6842.
155. V. Fourmond, N. Plumeré and C. Léger, *Nat. Rev. Chem.*, 2021, **5**, 348-360.
156. V. Fourmond, E. S. Wiedner, W. J. Shaw and C. Léger, *J. Am. Chem. Soc.*, 2019, **141**, 11269-11285.
157. M. Stephenson and L. H. Stickland, *Biochemical Journal*, 1931, **25**, 205-214.

# Acta Universitatis Upsaliensis

*Digital Comprehensive Summaries of Uppsala Dissertations  
from the Faculty of Science and Technology 2133*

Editor: The Dean of the Faculty of Science and Technology

A doctoral dissertation from the Faculty of Science and Technology, Uppsala University, is usually a summary of a number of papers. A few copies of the complete dissertation are kept at major Swedish research libraries, while the summary alone is distributed internationally through the series Digital Comprehensive Summaries of Uppsala Dissertations from the Faculty of Science and Technology. (Prior to January, 2005, the series was published under the title "Comprehensive Summaries of Uppsala Dissertations from the Faculty of Science and Technology".)



ACTA  
UNIVERSITATIS  
UPSALIENSIS  
UPPSALA  
2022

Distribution: [publications.uu.se](http://publications.uu.se)  
urn:nbn:se:uu:diva-470799